Shear Stress and the Vessel Wall

In vivo studies applying 3-D finite element modelling

Afschuifspanning en de vaatwand

In vivo studies waarbij 3-D eindige elementen modellering is toegepast

Proefschrift

ter verkrijging van de graad van doctor aan de
Erasmus Universiteit Rotterdam
op gezag van de rector magnificus
Prof.dr. P.W.C. Akkermans M.A.
en volgens besluit van College voor Promoties

De openbare verdediging zal plaatsvinden op
woensdag 19 januari 2000 om 13.45 uur

door

Jolanda Johanna Wentzel
geboren te Delft

Promotie Commissie:

Promotor:	Prof. dr. ir. N. Bom
Overige leden:	Prof. dr. P.W. Serruys Prof. dr. R.S. Reneman Prof. dr. C. Borst Dr. R. Krams (tevens co-promotor) Dr. ir. C.J. Slager (tevens co-promotor)

Shear Stress and the Vessel Wall,
In vivo studies applying 3-D finite element modelling

ISBN 90-73235-77-4

Cover: 3-D reconstruction of coronary artery with shear stress color coded at the surface. The left end of the 3-D reconstruction represents the grid applied for the 3-D finite element modelling.
Cover design: F. Kuijper

The financial support of the Interuniversity Cardiology Institute of the Netherlands and the Netherlands Heart Foundation is gratefully acknowledged.

The financial contribution of Boston Scientific is gratefully acknowledged.

Groot en wonderbaar zijn uw werken, Here God
Openbaring 15:3

aan mijn ouders

Contents

Contents

Contents

General introduction

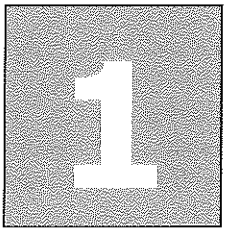

Atherosclerosis, a degenerative arterial disease, is a leading cause of death in the western society. It can cause dysfunction of the heart, stroke or peripheral vascular disease by limiting the blood supply to the heart, the brain, the abdominal organs and the legs. The narrowing of those arteries originates from the build up of 'atherosclerotic' plaques in the arterial wall. Such plaques are the result of accumulating lipids and accompanying reactive processes into the vessel wall. Several risk factors are known to induce and influence the progression of this disease like hypercholesteremia (Anderson *et al.*, 1987; Davis *et al.*, 1990), diabetes mellitus (Fontbonne *et al.*, 1989), high blood pressure (Jackson *et al.*, 1993; Kannel and Higgins, 1990) and smoking (Kannel and Higgins, 1990). Although these risk factors are systemic in nature, several studies showed that atherosclerotic plaques are not randomly distributed, but occur with preference to specific locations in the arterial tree. Similarly, after treatment of these narrowings, it seems that highly localized factors are involved in the healing process. The local nature of atherosclerosis and healing after treatment and their relation with biophysical factors, particularly shear stress, is the main subject of this thesis. Before going further into the detail of the locations of these lesions, first a brief overview is given of the process of atherosclerosis and restenosis.

1.1.1 Atherosclerosis

The earliest recognizable lesion of atherosclerosis is an aggregation of lipid-rich cells within the innermost layer of the arterial wall, called the fatty streak (Ross, 1976). The progression of this early form of atherosclerosis is accompanied by dysfunctional endothelium, which triggers a whole cascade of processes, so that the fatty streak progresses towards more complex composition (Ross, 1976).

Initially, while the arterial wall thickens, the growing plaque does not encroach into the arterial lumen because of adaptive growth of the total arterial circumference ('vessel remodeling') (Glagov *et al.*, 1987). However, this adaptive growth process apparently ceases at a certain stage of plaque development and lumen narrowing or even arterial occlusion may occur. (Glagov *et al.*, 1987).

1.1.2 Restenosis

Nowadays, the treatment of (partially) occluded arteries in order to restore the blood flow is highly focussed on minimally invasive techniques. Since Charles Dotter, in 1964, introduced the use of percutaneously applicable instruments to create a pathway through previously occluded vessels (Dotter and Judkins, 1964), several techniques became available. Examples of these techniques are the balloon catheter (Gruntzig *et al.*, 1979), the atherectomy catheter (Hansen *et al.*, 1988; Hofling *et al.*, 1988), the excimer laser (Bittl *et al.*, 1992; Litvack *et al.*,

1989). Although percutaneous transluminal angioplasty (PTA) results in restoration of the lumen, frequently within a few months renarrowing of the arteries is observed, which is defined as restenosis when the renarrowing exceeds 50% of the reference segment. In 30%-50% of the patients, restenosis is observed at the treated site within a period of 6 months (Fischman *et al.*, 1994; Serruys *et al.*, 1994). Recently, it became clear that the main determinant of restenosis after PTA is not the neointimal formation, but the so-called negative remodeling or 'vessel shrinkage' (Kakuta *et al.*, 1994; Lafont *et al.*, 1993; Mintz *et al.*, 1993; Post *et al.*, 1994). Vessel shrinkage is a structural change in the total arterial wall, which renarrows the treated arterial segment. In order to overcome the vessel shrinkage after PTA, endovascular prosthesis (stents) were applied and firstly used in human coronary arteries by Jacques Puel (Toulouse, France) in 1986, shortly followed by Ulrich Sigwart (Sigwart *et al.*, 1987). By early 1988, already 117 stents were implanted in native coronary arteries or aortocoronary bypass grafts (Serruys *et al.*, 1991). In 1994 Serruys (Serruys *et al.*, 1994) and Fischman (Fischman *et al.*, 1994) showed that this approach was superior to balloon angioplasty, however still a restenosis rate of 22-32% was observed at 6 months follow up, which now was largely caused by neointimal formation.

Another way to prevent the artery from negative remodeling after balloon angioplasty is by pharmacological treatment. Negative remodeling of the vessel wall is accompanied by a process of degradation and restructuring of the extra cellular matrix. Therefore treatment was directed against the most active matrix degrading enzymes (Matrix Metalloproteinases). Inactivating those enzymes has shown promising results in pigs in attenuating vessel shrinkage and studies are in preparation to investigate this treatment in patients (de Smet, 1998).

1.1.3 Localization of atherosclerotic and restenotic lesions

Atherosclerotic plaques are not uniformly distributed in the arterial system, (Friedman *et al.*, 1993; Sabbah *et al.*, 1984; Smedby *et al.*, 1995). Well-known predilection sites are located at the inner curve of coronary arterial segments, near side branches of the coronary arteries, the aorta, the bulb of the carotid artery (Friedman *et al.*, 1993; Ku *et al.*, 1985; Masawa *et al.*, 1994; Moore *et al.*, 1994; Sabbah *et al.*, 1984; Smedby *et al.*, 1995, Kornet *et al*, 1998). These observations imply that besides the systemic risk factors, additional localizing factors must be involved in the atherosclerotic process. Proposed localizing factors include regional vessel wall stress (Thubrikar and Robicsek, 1995); local high lipid concentrations in the blood (Caro *et al.*, 1971); regional permeability variations (Fry, 1968); regional vascular geometry (Friedman *et al.*, 1986) and regional shear stress of the blood at the vessel wall (Ku *et al.*, 1985; Sabbah *et al.*, 1984; Sabbah *et al.*, 1986). Although all these factors seem not related to each other, they are to a certain extent connected to either the local shear stress or wall stress.

In the next paragraph, the relationship between shear stress, wall stress and the biological process involved in atherosclerosis is described into more detail.

In resemblance to the development of atherosclerotic lesions, it does not seem unlikely that the vessel growth processes, which repair an artery after mechanical treatment, are also related to the mentioned biophysical factors. This hypothesis implies that the restenotic lesions should be located at specific locations in the artery. Indeed such specific locations are reported for the restenotic lesions observed after stent implantation, like for instance at the stent (Palmaz Schatz) margins (Hoffmann *et al.*, 1997), the central articulation (Hoffmann *et al.*, 1996). Furthermore, Fontaine observed that the restenotic lesions show an eccentric distribution six months after stent implantation (Fontaine *et al.*, 1994). Whether these specific locations are related to either the shear stress or wall stress distribution is unknown. For the restenotic lesions after balloon angioplasty no particular pattern has been described.

1.2 Biophysical factors

The biophysical factors scrutinized in this thesis are shear stress and wall stress related to the development of atherosclerosis and restenosis by either neointimal formation or vascular remodeling. Therefore a general overview is given of the role of shear stress and wall stress in biological processes involved in atherosclerosis and restenosis.

1.2.1 Shear stress and wall stress

Shear stress is the friction force between fluid layers flowing at different speed with respect to each other. Especially near the vessel wall, generally large velocity gradients between fluid layers exist and the shear stress is at its highest value.

The wall stress is the tensile force in the vessel wall itself, in order to withstand the blood pressure. The wall stress is dependent on the local pressure, local vessel radius and the wall thickness ('Laplace Law').

1.2.2 Shear stress and wall stress in vascular biology

The shear stress imposed on the endothelium by the movement of blood deforms the endothelial cells to a very small amount, but stimulates shear stress sensing elements probably integrins in the endothelial wall.These integrins may act as sensors, which induce the activation of second messenger systems (Bhullar *et al.*, 1998).

It is has been well established, that the vessel dilates under the influence of an acute increment in flow, thereby controlling the shear stress in an artery ('flow dependent vasodilatation'; (Lie *et al.*, 1970)). Furchgott showed that products released by the endothelium play a crucial role in maintaining shear stress at a certain level (Furchgott and Zawadzki, 1980). A variety of vasoactive substances are produced by the endothelium under the influence of shear stress (Davies and Tripathi, 1993; McIntire, 1994). The most described factor is EDRF or nitric oxide (NO), which is produced in a shear stress dependent way. The endothelium also produces, as a response to alterations of shear stress, Prostacycline and Endothelin-1 (Davies and Tripathi, 1993; Redmond *et al.*, 1997). There is a delicate interplay between NO, Endothelin-1 and Prostacycline production (Davies and Tripathi, 1993; Redmond *et al.*, 1997). After sustained periods of shear stress alterations the endothelial cells accommodate to the new environment through the activation of several genes, including the early response genes (c-myc, c-fos and c-jun), NOS III gene, TGF β-1, ICAM-1, VCAM-1 and PDGF-B genes. It has been shown that the regulation of some of these genes is dependent on shear responsive elements (Resnick *et al*, 1997). More sustained stimulation with shear stress, remodels the organization of F-actine microfilaments and aligns

the endothelial cells to the streamlines of the flow (Resnick, *et al*, 1997) Furthermore, integrins in the cell membrane tend to cluster after chronic shear stress increments, which amplifies the shear stress signal making the endothelial cells more susceptible to shear stress (Takahashi *et al.*, 1997).

Acute changes in vessel wall stress, for instance induced by changes in the transmural pressure, result within seconds in a rise in intracellular Ca^{2+} and IP_3. (Davies and Tripathi, 1993). In a period of hours the cells start to realign perpendicular to the strain. Additionally, the F-actin filament starts to redistribute and finally after 5 days collagen production is inhibited and cell growth is stimulated. By sustained changes in circumferential stress the endothelial cells start to activate certain genes. Studies from in vitro experiments reveal that similar to the shear stress, the circumferential stretch induces the expression of eNOS, ET-1, ICAM-1.

1.2.3 Shear stress and lipid uptake in atherosclerosis

Shear stress and its localizing role in atherosclerosis has been postulated by Caro *et. al.* in 1971. They proposed a shear stress dependent transfer of lipids into the vessel wall (Caro *et al.*, 1971). According to that theory, *low shear stress* promotes the interaction between blood borne elements and the vessel wall. Fry, on the other hand, provided experimental evidence for a *high shear stress* related desquamation of the endothelium (Fry, 1968). Due to the lost barrier function of the endothelium, diffusion of blood borne elements into the vessel wall might be facilitated (Fry, 1968). Later measurements showed clearly that low shear stress and not high shear stress promotes atherosclerotic development (Friedman *et al.*, 1986; Giddens *et al.*, 1993; Sabbah *et al.*, 1986). According to modeling studies, low shear stress regions are accompanied by local high LDL concentrations in the blood near the arterial wall (Deng *et al.*, 1995). In contrast, the permeability of an artery is positively related to the shear stress (Jo *et al.*, 1991; Waters, 1996). Interestingly, the accumulation of LDL in the vessel wall is high in low shear stress regions (Gibson *et al.*, 1993), which suggests that the balance between permeability and LDL concentration is responsible for the final result.

Despite the consensus that low shear stress regions favor atherosclerosis, evidence for the validity of this theory originates mainly from animal experiments and from post mortem studies in humans (Friedman *et al.*, 1987; Friedman *et al.*, 1992; Moore *et al.*, 1994). In the later studies, the post mortem specimens were used to construct a 3-D-model of the artery. With the help of laser Doppler techniques or computational fluid dynamics (Friedman *et al.*, 1992), the shear stress at the wall was derived by measuring or calculating the velocity profile and a relation was found between shear stress and the location of atherosclerotic plaques.

1.2.4 Shear stress, wall stress and vascular remodeling

Sustained increments in flow, structurally increase the vessel diameter mediated by the activation of several genes (section 1.2.2) (Kamiya and Togawa, 1980; Zarins *et al.*, 1987). Such a structural adaptation of the vessel wall is called vascular remodeling and has a much larger effect than the acute response. For instance, 2 to 3 weeks of steady flow increment by a factor of 7 increases the diameter of the carotid artery in atherosclerotic rabbits by 83%. This contrasts with the range of adaptation to acute increments in flow, which increased the vessel diameter only in the order of 10% (Tronc *et al.*, 1996). The mentioned 83% increase of the vessel diameter implies a reduction of shear stress to its baseline values. Hence, it has been postulated that a negative feedback loop exists between shear stress and the vessel lumen with shear stress as the controlling variable (Kamiya and Togawa, 1980). Glagov's group showed that this negative feedback loop indeed exists and also remains intact in experimental atherosclerosis (Zarins *et al.*, 1987). Therefore, due to the high compensatory potential of the feedback loop, this mechanism is able to adjust for most of the atherosclerotic plaques found in patients. As shown by the same group of researchers, human coronary vessels show expansion of their outer vessel circumference until the plaque area occupies approximately 40% of total wall area. Thereafter compensation is lost and lumen narrowing occurs (Glagov *et al.*, 1987). Later studies confirmed this post mortem study and extended the findings in vivo by intra vascular ultrasound (IVUS) measurements in humans (Mintz *et al.*, 1997).

Besides the influence of shear stress on the vascular remodeling, changes in wall stress have shown to be of some importance too, but now in order to restore the wall stress to its baseline values. For instance, during hypertension, the circumferential stress increases, which is followed by a proportional increase in the vessel wall thickness, such that the artery remodels (Bevan *et al.*, 1975; Girerd *et al.*, 1994; Wolinsky, 1970).

1.2.5 Shear stress, wall stress and neointimal formation

The first experiment investigating the influence of shear stress on neointimal formation after intervention was performed by Kohler in 1991. He showed in endothelialized grafts placed in baboons, that increasing the shear stress in the graft reduced the neointimal formation at follow up (Kohler *et al.*, 1991). At the locations of reduced flow, the neointimal thickness was increased. Similar observations were reported by Salam in PTFE bypass grafts implanted in dogs. At the low shear stress regions the neointima was significantly thicker than at the high shear stress regions (Salam *et al.*, 1996). Furthermore, increasing the shear stress 2 months after graft implantation induced a regression of the neointimal thickness (Mattsson *et al.*, 1997). Shear stress related neointimal formation is reported at the edges of anastomosis as well (Ethier *et al.*, 1998; Liu, 1998). At these edges, disturbances in the flow as well as low shear stress regions were

observed, which were significantly related to the neointimal growth (Liu, 1998). These findings suggest that shear stress is involved in the generation of neointimal formation.

Until now the only experiments suggesting shear stress to be related to in-stent neointimal formation refer to in vitro experiments. As an example the reendothelialization of stent material was studied in vitro in relation to the local shear stress and appeared to be shear stress dependent, such that the low shear stress regions are delayed in endothelialization compared to high shear stress regions (Sprague *et al.*, 1997). Since reendothelialization is assumed to play a key role in controlling neointimal formation after stent implantation (Asahara *et al.*, 1995; Chen *et al.*, 1999), this observation suggest that also in stent neointimal formation may be related to shear stress. Furthermore, in resemblance to the neointimal formation observed in vascular bypass grafts or anastomosis, it is not unlikely that shear stress has similar influence on the vascular repair process after stent implantation, thereby influencing the neointimal formation.

Other investigators suggest that the tensile stress is an important factor that influences the neointimal formation in stents or vascular bypass grafts (Predel *et al.*, 1992). In vascular bypass grafts, it was shown that under influence of pulsatile stretch (60 cylces/min) the cell number in the by pass graft was significantly increased after a period of 6 days.

Furthermore, wall stress is also proposed as a candidate to influence the neointimal growth after stent implantation. Vorwerk did some experiments thereby changing the radial force of Wallstents. He showed that decreasing the local radial force did not influence the local neointimal formation (Vorwerk *et al.*, 1994). So these data suggest that the observed neointimal growth is not due to the radial force of the stent.

1.2.6 Shear stress, wall stress and Matrix Metalloproteinases

Matrix metalloproteinases (MMP) are a group of enzymes, which are responsible for the degeneration of the extracellular matrices in both normal physiological and patho-physiological processes. Nine types of MMPs are identified and are divided into three groups based on the substrate preferences. The *collagenases* degrade type I and III collagens, *gelatinases* act mainly on the basement membrane components and *stromelysins* cover a broad range of substrates including proteoglycans, laminin, fibronectin, basement membrane collagens (Dollery *et al.*, 1995). Several studies showed that the MMPs are involved in the flow mediated remodeling of arteries by applying specific MMP-inhibitors (Abbruzzese *et al.*, 1998; Bassiouny *et al.*, 1998). Others showed that even in a period of 7 days of changed flow conditions the MMP-2 mRNA expression was upregulated for both low and high flow conditions (Bassiouny *et al.*, 1998),which suggests that changes in shear stress mediate the production of MMPs.

Not only during remodeling, but also after vessel injury, for instance after balloon angioplasty, the MMP expression was increased (Zempo *et al.*, 1994). It was proposed that vessel stretch itself caused the expression of MMP-2 and MMP-9, as studied by Meng (Meng *et al.*, 1999). The pharmaceutical inhibition of MMPs after vessel injury by, for instance, balloon angioplasty, showed to prevent the smooth muscle cells from migration (Zempo *et al.*, 1996), but did not reduce neointimal formation (Bendeck *et al.*, 1996). Since MMPs are involved in the processes of extra cellular matrix remodeling and smooth muscle migration (Bendeck *et al.*, 1996), recent experiments showed that MMP-inhibition could prevent the artery from vascular remodeling after balloon angioplasty in the atherosclerotic pig (de Smet, 1998).

1.3.1 Problem definition and hypothesis

As described before, restenosis after an intervention is still a drawback in its application either caused by neointimal formation or by excessive vascular remodeling. Until now the proposed mechanisms explaining these phenomenon are heavily focussed on the wall healing response as a self controlled entity. However, as a result of the restoration of the flow through a previous narrowed artery by balloon angioplasty and stent placement, it may be expected that both the local shear stress and the local wall stress are affected. In normal arteries changes in both shear stress and wall stress are restored to their baseline values by either vascular remodeling (Langille, 1993) or vessel wall growth (Girerd *et al.*, 1994). So it may be hypothesized that after balloon angioplasty the artery remodels in order to restore the shear stress and wall stress to less or more normal values. In contrast, after stent placement the artery is not able to remodel anymore, so in that case neointimal formation only could be the result of the regulation of the local shear stress and or the wall stress.

Thus our hypothesis is that the process of vascular remodeling and neointimal formation in repairing the artery occurs in a shear stress and wall stress controlled way.

In this thesis the experiments performed to test this hypothesis are described.

1.3.2 Research objectives

Until now, only a couple of studies were carried out investigating the possible role of shear stress and wall stress in the development of restenosis after stent implantation or balloon angioplasty. The experiments pointing towards the relationship between in stent restenosis and shear stress concerned in vitro studies studying the shear stress dependent permeability of the endothelium and the migration of the endothelial or smooth muscle cells (Jo *et al.*, 1991; Ono *et al.*, 1991; Sprague *et al.*, 1997). Other studies concerned the shear stress related neointimal growth in vascular bypass grafts or anastomosis (Ishibashi *et al.*, 1995; Salam *et al.*, 1996).

Considering atherosclerosis, no in vivo studies in patients are known directly relating shear stress to the development of atherosclerosis.

Therefor the aims of our studies were:

1. to select or develop a non-destructive method applicable *in vivo*, enabling the local determination and comparison of shear stress, wall stress and the geometry of the arterial wall, thereby focussing on the application in the field of cardiology
2. to study *in vivo* the relationship between shear stress and/or wall stress and the neointimal growth, vessel remodeling after intervention and the grade of atherosclerotic plaque, also focussing on the field of cardiology.

1.3.3 Selection of techniques

Several techniques can be thought of to accomplish the aim of our study. In order to measure shear stress in vivo several techniques have been proposed, but mostly they do not allow measuring the vessel wall at the same location. These techniques will be discussed briefly to elucidate the rationale of our final approach.

External Ultrasound

The externally applied ultrasound systems, which are placed in contact with the skin of the patient, enable to measure shear rate for example at the posterior wall of the carotid arteries derived from the Doppler based velocity profile (Reneman *et al.*, 1986; Brands *et al.*, 1995; Tortoli *et al.*, 1996; Tortoli *et al.*, 1997; Kornet *et al.*, 1998). Furthermore application of this technique is known in an open surgical procedure of the aorta of a swine (Sawchuk *et al.*, 1994). Recently, ultrasound measurements became also possible in proximal coronary arteries by transesophageal echocardiography. Unfortunately, until now only coronary flow reserve measurements were successful (Coletta *et al.*, 1999; Gadallah *et al.*, 1998), but no velocity profile measurements in coronary arteries have been reported. In principle, this technique might provide details on the wall geometry simultaneously with the shear rate.

Intravascular Ultrasound (IVUS)

Another recent development is the Intravascular ultrasound (IVUS) technique to measure velocity profiles based on the decorrelation of the radio frequency signal (RF-signal) (Li, 1997). Although the flow estimation from the obtained velocity profiles gives promising results and cross sectional information of the arterial wall is achieved, the presence of the catheter in the lumen disturbs the blood velocity patterns and therefore precludes the possibility to obtain physiological velocity profiles in vivo (Chapter 2).

Intravascular Ultrasound Doppler

Similar problems as described for the IVUS are observed for the intravascular ultrasound Doppler techniques using a Doppler guide wire. They only can be used to measure the peak velocity of the velocity profile (Doucette *et al.*, 1992). However this technique does not provide the shape of the velocity profile itself nor the wall geometry, which limits its application to derive local shear stress values at the vessel wall in an eccentric way and the wall thickness.

Magnetic Resonance Imaging (MRI)

Techniques based on Magnetic Resonance Imaging (MRI) to quantify flow in arteries stem from 1959 (Singer, 1959). However, from the eighties on, quantitative flow measurements were performed in phantoms and in the renal artery, carotid artery the basilar artery, coronary artery and in the abdominal aorta in vivo (Buonocore, 1998; Firmin *et al.*, 1987; Maier *et al.*, 1989; Meier *et al.*, 1988) and they seem to give promising results in measuring velocity profiles as well (Rittgers *et al.*, 1988). Until now this technique is applied in the cardiology to measure flow and coronary flow reserve (Davis *et al.*, 1997; Grist *et al.*, 1997), however measuring velocity profiles in coronary arteries seems not achievable until now. Furthermore accurate reconstruction of local coronary wall geometry is currently out of reach of the technical possibilities of this technique.

Computational fluid dynamics

Another way to obtain shear stress is by computational fluid dynamics. Computational fluid dynamics is the general term of all the numerical techniques to calculate the velocity of fluid elements at each location in a certain geometry. In order to calculate these velocities of fluid elements at each location, the incompressible Navier Stokes equations need to be solved. The Navier Stokes equations are 3-D nonlinear differential equations and describe the movement of fluid elements based on conservation of energy and mass (Fox and McDonald, 1992). Since these equations are non-linear and applied to complex geometries, numerical techniques need to be used to solve them. Nowadays, several numerical techniques are applied and in development.

Table 1: Determination of shear rate and wall thickness

	Flow	Velocity profiles	Wall thickness	Applicable in coronary arteries
Ultrasound (external)	+	+	+	-
Ultrasound (TEE)	+	-	±	±
IVUS	+	±	+	+
Doppler	+	-	-	+
MRI	+	-	±	±
CFD + true 3-D recontruction technique	-	+	+	+

IVUS: intra vascular ultrasound, MRI: magnetic resonance imaging, CFD: computational fluid dynamics, TEE: transesophageal echocardiography, +:the ability to measure either flow, velocity profiles, wall thickness in among others coronary arteries; ±: in principle possible.

From these calculations the velocity profiles, the pressure differences and the shear stresses are obtained. As great advantage of these numerical techniques, compared to all the ultrasound based techniques, is that the velocity determined in an uncompromised directional way in contrast to the ultrasound Doppler techniques, which only provide information in the direction of the ultrasound beam. Therefore secondary velocity fields, perpendicular to the flow transition field, cannot be studied with ultrasound based techniques.

Application of computational fluid dynamics to an artery requires a 3-D description of the studied artery. Although a lot of effort is put to obtain 3-D reconstructions of coronary arteries in vivo based on either angiography (Muhlestein *et al.*, 1997; Parker *et al.*, 1987; Wahle *et al.*, 1995), intravascular ultrasound (Evans *et al.*, 1996; Kitney *et al.*, 1989; Koch *et al.*, 1993) or MRI (van Geuns *et al.*, 1999), still the resolution or the accuracy of the 3-D curvature of the artery of those methods was limited. For reaching a better resolution and accuracy a new 3-D reconstruction method was developed based on a combination of angiography and intravascular ultrasound ('ANGUS'). The intravascular ultrasound technique provided high cross sectional resolution, while the angiography was used to 3-D reconstruct the 3-D curvature of the artery. This combination of ANGUS with computational fluid dynamics offers the unique possibility to acquire a detailed measurement of the local wall geometry and to combine this with local shear stress values.

Table 1 summarizes the described techniques in its application to measure velocity profiles and the local wall geometry. Although all the techniques are to a certain extent able to measure accurately flow or velocity profiles, the only technique to measure both shear stress and the local wall geometry is by a combination of 3-D reconstruction techniques and computational fluid dynamics. The new combination of methods lacks the possibility to measure the flow, but is still valuable as it resolves the local differences in shear stress values in an artery,

which for our purpose is sufficient. In case absolute shear stress values are required, these should be obtained in combination with another flow measurement.

In this thesis, studies are described, which focus on the relationship between shear stress, wall stress and atherosclerotic plaque location, neointimal formation and vascular remodeling *in vivo*.

To study the influence of shear stress on the location of atherosclerosic plaques and the development of neointima and vascular remodeling after intervention, the local shear stress, local wall (neointimal) thickness and lumen are required. A direct measuring technique is preferred for this goal and an ultrasound based catheter technique coming close is described in Chapter 2. However, the influence of the inserted catheter in the arterial system on the measured velocity profiles precludes the possibility of achieving accurate local shear stress values. This influence a blood velocity catheter on the measured velocity profiles and therefore on the shear stress of blood at the vessel wall is further elucidated in this chapter.

An optimal solution, to obtain shear stress and wall geometry, was found in the combination of a new technique (ANGUS) based on biplane angiography and Intravascular Ultrasound (IVUS) and computational fluid dynamics. ANGUS provides high resolution of both the lumen geometry and the local wall thickness and enables the application of computational fluid dynamics. In Chapter 3, details of the (ANGUS) 3-D reconstruction technique and its validation in clinical practice is described.

Chapter 4 describes the first application of a combination of both techniques applied on an atherosclerotic human coronary artery in vivo. The relation between local vessel wall thickness and local shear stress is further elucidated.

A first study on restenosis, described in Chapter 5, focuses on the changes in local shear stress induced by implantation of Wallstents in pigs.

Chapter 6 reports on a study in patients after Wallstent implantation and describes the relationship between the variations in the observed neointimal thickness and the variations in shear stress after stent implantation.

Chapter 1, introduction

To better understand the fundamental role of shear stress and wall stress on vascular remodeling and neointimal formation and their interaction after balloon angioplasty, two studies were carried out in atherosclerotic Yucatan pigs in cooperation with the Experimental Cardiology Department of the University Hospital of Utrecht. In Chapter 7, the influence of changes in shear stress and wall stress induced by balloon angioplasty on the vascular remodeling is discussed, whereas in Chapter 8 the influence of the Matrix Metalloproteinase inhibitor (Batimastat) on these processes is described.

Abbruzzese, T. A., Guzman, R. J., Martin, R. L., Yee, C., Zarins, C. K. and Dalman, R. L. (1998) Matrix metalloproteinase inhibition limits arterial enlargements in a rodent arteriovenous fistula model. *Surgery* **124**, 328-34; discussion 334-5.

Anderson, K. M., Castelli, W. P. and Levy, D. (1987) Cholesterol and mortality. 30 years of follow-up from the Framingham study. *Jama* **257**, 2176-80.

Asahara, T., Bauters, C., Pastore, C., Kearney, M., Rossow, S., Bunting, S., Ferrara, N., Symes, J. F. and Isner, J. M. (1995) Local delivery of vascular endothelial growth factor accelerates reendothelialization and attenuates intimal hyperplasia in balloon-injured rat carotid artery [see comments]. *Circulation* **91**, 2793-801.

Bassiouny, H., Song, R., Hong, X., Singh, A., Kocharyan, H. and Glagov, S. (1998) Flow regulation of 72-kD collagenase IV (MMP-2) after experimental arterial injury. *Circulation* **98**, 157-163.

Bendeck, M. P., Irvin, C. and Reidy, M. A. (1996) Inhibition of matrix metalloproteinase activity inhibits smooth muscle cell migration but not neointimal thickening after arterial injury. *Circ Res* **78**, 38-43.

Bevan, J. A., Bevan, R. D., Chang, P. C., Pegram, B. L., Purdy, R. E. and Su, C. (1975) Analysis of changes in reactivity of rabbit arteries and veins two weeks after induction of hypertension by coarctation of the abdominal aorta. *Circ Res* **37**, 183-90.

Bhullar, I. S., Li, Y. S., Miao, H., Zandi, E., Kim, M., Shyy, J. Y. and Chien, S. (1998) Fluid shear stress activation of IkappaB kinase is integrin-dependent. *J Biol Chem* **273**, 30544-9.

Bittl, J. A., Sanborn, T. A., Tcheng, J. E., Siegel, R. M. and Ellis, S. G. (1992) Clinical success, complications and restenosis rates with excimer laser coronary angioplasty. The Percutaneous Excimer Laser Coronary Angioplasty Registry [see comments]. *Am J Cardiol* **70**, 1533-9.

Brands, P., Hoeks, A., Hofstra, L. and Reneman, R. (1995) A noninvasive method to estimate wall shear rate using ultrasound. *Ultrasound in medicine and biology* **21**, 171-185.

Buonocore, M. H. (1998) Visualizing blood flow patterns using streamlines, arrows, and particle paths. *MRM* **40**, 210-226.

Caro, C. G., Fitz-Gerald, J. M. and Schroter, R. C. (1971) Atheroma and arterial wall shear. Observation, correlation and proposal of a shear dependent mass transfer mechanism for atherogenesis. *Proc R Soc Lond B Biol Sci* **177**, 109-59.

Chen, D., Asahara, T., Krasinski, K., Witzenbichler, B., Yang, J., Magner, M., Kearney, M., Frazier, W., Isner, J. and Andres, V. (1999) *Circulation* **100**, 849-54.

Coletta, C., Galati, A., Ricci, R., Sestili, A., Aspromonte, N., Richichi, G. and Ceci, V. (1999) Coronary flow reserve of normal left anterior descending artery in patients with ischemic heart disease: A transesophageal doppler study. *J Am Soc Echocardiogr* **12**, 720-8.

Davies, P. F. and Tripathi, S. C. (1993) Mechanical stress mechanisms and the cell. An endothelial paradigm. [Review]. *Circ Res* **72**, 239-45.

Davis, C., Rifkind, B., Brenner, H. and Gordon, D. (1990) A single cholesterol measurement underestimates the risk of CHD. An empirical example from the Lipid Research Clinics mortality follow up study. *Jama* **264**, 3044-3046.

Davis, C. P., Liu, P., Hauser, M., Goehde, S. C., von Schulthess, G. K. and Debatin, J. F. (1997) Coronary flow and coronary flow reserve measurements in humans with breath-held magnetic resonance phase contrast velocity mapping. *MRM*, 537-544.

de Smet, B. J. G. L. (1998) A new Paradigm in Restenosis: Morphometric and Molecular Characteristics. *dissertation*.

Deng, X., Marois, Y., How, T., Merhi, Y., King, M., Guidoin, R. and Karino, T. (1995) Luminal surface concentration of lipoprotein (LDL) and its effect on the wall uptake of cholesterol by canine carotid arteries [published erratum appears in J Vasc Surg 1995 Dec;22(6):648]. *J Vasc Surg* **21**, 135-45.

Dollery, C. M., McEwan, J. R. and Henney, A. M. (1995) Matrix metalloproteinases and cardiovascular disease. *Circ Res* **77**, 863-8.

Dotter, C. and Judkins, M. P. (1964) Transluminal treatment of arteriosclerotic obstruction. *Circulation* **30**, 654-670.

Doucette, J. W., Corl, P. D., Payne, H. M., Flynn, A. E., Goto, M., Nassi, M. and Segal, J. (1992) Validation of a Doppler guide wire for intravascular measurement of coronary artery flow velocity. *Circulation* **85**, 1899-911.

Ethier, C. R., Steinman, D. A., Zhang, X., Karpik, S. R. and Ojha, M. (1998) Flow waveform effects on end-to-side anastomotic flow patterns. *J Biomech* **31**, 609-17.

Evans, J., Kok-Hwee, N., Wiet, S., Vonesh, M., Burns, W., Radvany, M., Kane, B., Davidson, C., Roth, S., Kramer, B., Meyers, S. and McPherson, D. (1996) Accurate Three-dimensional reconstruction of intravascular ultrasound data. Spatially correct three-dimensional reconstructions. *Circulation* **93**, 567-576.

Firmin, D. N., Nayler, G. L., Klipstein, R. H., Underwood, S. R. and Rees, R. S. O. (1987) In vivo validation of MR velocity imaging. *Journal of computer assisted tomography* **11**, 751-756.

Fischman, D., Leon, M., Baim, D., Schatz, R., Savage, M., Penn, I., Detre, K., Veltri, K., Ricci, D., Nobuyoshi, M. and Investigators, e. a. f. t. S. R. S. (1994) A randomized comparison of coronary stent placement and balloon angioplasty in the treatment of coronary artery disease. *N Engl J Med* **331**, 539-541.

Fontaine, A. B., Spigos, D. G., Eaton, G., Das Passos, S., Christoforidis, G., Khabiri, H. and Jung, S. (1994) Stent-induced intimal hyperplasia: are there fundamental differences between flexible and rigid stent designs? *J Vasc Interv Radiol* **5**, 739-44.

Fontbonne, A., Eschwege, E., Cambien, F., Richard, J., Ducimetiere, P., Thibult, N., Warnet, J., Claude, J. and Rosselin, G. (1989) Hypertriglyceridemia as a risk factor of coronary heart-disease mortality in subjects with impaired glucose-tolerance or diabetes- results from the 11-year follow up of the paris prospective-study. *Diabetologia* **32**, 300-304.

Fox, R. W. and McDonald, A. T. (1992) Introduction to fluid mechanics. John wiley & sons, inc.

Friedman, M., Deters, O., Bargeron, C., Hutchins, G. and Mark, F. (1986) Shear-dependent thickening of the human arterial intima. *Atherosclerosis* **60**, 161-71.

Friedman, M. H., Bargeron, C. B., Deters, O. J., Hutchins, G. M. and Mark, F. F. (1987) Correlation between wall shear and intimal thickness at a coronary artery branch. *Atherosclerosis* **68**, 27-33.

Friedman, M. H., Bargeron, C. B., Duncan, D. D., Hutchins, G. M. and Mark, F. F. (1992) Effects of arterial compliance and non-Newtonian rheology on correlations between intimal thickness and wall shear. *J Biomech Eng* **114**, 317-20.

Friedman, M. H., Brinkman, A. M., Qin, J. J. and Seed, W. A. (1993) Relation between coronary artery geometry and the distribution of early sudanophilic lesions. *Atherosclerosis* **98**, 193-9.

Fry, D. L. (1968) Acute vascular endothelial changes associated with increased blood velocity gradients. *Circ Res* **22**, 165-97.

Furchgott, R. F. and Zawadzki, J. V. (1980) The obligatory role of endothelial cells in the relaxation of arterial smooth muscle by acetylcholine. *Nature* **288**, 373-6.

Gadallah, S., Thaker, K., Kawanishi, D., A, M., Lau, S., Rashtian, M. and Chandraratna, A. (1998) Comparison of intracoronary Doppler guide wire and transesophageal echocardiography in measurement of low velocity and coronary flow reserve in the left anterior descending coronary artery. *Am Heart J* **135**, 38-42.

Gibson, C. M., Diaz, L., Kandarpa, K., Sacks, F. M., Pasternak, R. C., Sandor, T., Feldman, C. and Stone, P. H. (1993) Relation of vessel wall shear stress to

atherosclerosis progression in human coronary arteries. *Arterioscler Thromb* **13**, 310-5.

Giddens, D. P., Zarins, C. K. and Glagov, S. (1993) The role of fluid mechanics in the localization and detection of atherosclerosis. *J Biomech Eng* **115**, 588-94.

Girerd, X., Mourad, J. J., Copie, X., Moulin, C., Acar, C., Safar, M. and Laurent, S. (1994) Noninvasive detection of an increased vascular mass in untreated hypertensive patients. *Am J Hypertens* **7**, 1076-84.

Glagov, S., Weisenberg, E., Zarins, C. K., Stankunavicius, R. and Kolettis, G. J. (1987) Compensatory enlargement of human atherosclerotic coronary arteries. *N Engl J Med* **316**, 1371-5.

Grist, T. M., Polzin, J. A., Bianco, J. A., Foo, T. K. F., Bernstein, M. A. and Mistretta, C. M. (1997) Measurement of coronary blood flow and flow reserve using magnetic resonance imaging. *Cardiology* **88**, 80-89.

Gruntzig, A. R., Senning, A. and Siegenthaler, W. E. (1979) Nonoperative dilatation of coronary-artery stenosis: percutaneous transluminal coronary angioplasty. *N Engl J Med* **301**, 61-8.

Hansen, D., Auth, D., Vracko, R. and Ritchie, J. (1988) Rotational atherectomy in atherosclerotic rabbit iliac arteries. *Am Heart J* **115(1 Pt 1)**, 160-5.

Hoffmann, R., Mintz, G. S., Dussaillant, G. R., Popma, J. J., Pichard, A. D., Satler, L. F., Kent, K. M., Griffin, J. and Leon, M. B. (1996) Patterns and mechanisms of in-stent restenosis. A serial intravascular ultrasound study. *Circulation* **94**, 1247-54.

Hoffmann, R., Mintz, G. S., Kent, K. M., Satler, L. F., Pichard, A. D., Popma, J. J. and Leon, M. B. (1997) Serial intravascular ultrasound predictors of restenosis at the margins of Palmaz-Schatz stents. *Am J Cardiol* **79**, 951-3.

Hofling, B., Polnitz, A., Backa, D., von Arnim, T., Lauterjung, L., Jauch, K. and Simpson, J. (1988) Percutaneous removal of atheromatous plaques in peripheral arteries. *Lancet I* **1**, 384-6.

Ishibashi, H., Sunamura, M. and Karino, T. (1995) Flow patterns and preferred sites of intimal thickening in end-to-end anastomosed vessels. *Surgery* **117**, 409-20.

Jackson, R., Barham, P., Bills, J., Birch, T., McLennan, L., MacMahon, S. and Maling, T. (1993) Management of raised blood pressure in New Zealand: a discussion document. *Bmj* **307**, 107-10.

Jo, H., Dull, R. O., Hollis, T. M. and Tarbell, J. M. (1991) Endothelial albumin permeability is shear dependent, time dependent, and reversible. *Am J Physiol* **260**, H1992-6.

Kakuta, T., Currier, J. W., Haudenschild, C. C., Ryan, T. J. and Faxon, D. P. (1994) Differences in compensatory vessel enlargement, not intimal formation, account for restenosis after angioplasty in the hypercholesterolemic rabbit model. *Circulation* **89**, 2809-15.

Kamiya, A. and Togawa, T. (1980) Adaptive regulation of wall shear stress to flow change in the canine carotid artery. *Am J Physiol* **239**, H14-21.

Kannel, W. B. and Higgins, M. (1990) Smoking and hypertension as predictors of cardiovascular risk in population studies. *J Hypertens Suppl* **8**, S3-8.

Kitney, R., Moura, L. and Straughan, K. (1989) 3-D visualization of arterial structures using ultrasound and voxel modeling. *Int J Card Imaging* **4**, 135-43.

Koch, L., Kearney, P., Erbel, R., Roth, T., Ge, J., Brenneke, R. and Meyer, J. (1993) Three dimensional reconstruction of intracoronary ultrasound images: roadmapping with simultaneously digitised coronary angiograms. *IEEE Computers in Cardiology*, 89-91.

Kohler, T. R., Kirkman, T. R., Kraiss, L. W., Zierler, B. K. and Clowes, A. W. (1991) Increased blood flow inhibits neointimal hyperplasia in endothelialized vascular grafts. *Circ Res* **69**, 1557-65.

Kornet, L., Lambregts, J., Hoeks, A. P. and Reneman, R. S. (1998) Differences in near-wall shear rate in the carotid artery within subjects are associated with different intima-media thicknesses. *Arterioscler Thromb Vasc Biol* **18**, 1877-84.

Ku, D. N., Giddens, D. P., Zarins, C. K. and Glagov, S. (1985) Pulsatile flow and atherosclerosis in the human carotid bifurcation. Positive correlation between plaque location and low oscillating shear stress. *Arteriosclerosis* **5**, 293-302.

Lafont, A. M., Chisolm, G. M., Whitlow, P. L., Goormastic, M. and Cornhill, J. F. (1993) Post-angioplasty restenosis in the atherosclerotic rabbit: Proliferative response or chronic constriction ? *Circulation* **88**, I-521(abstr).

Langille, B. L. (1993) Remodeling of developing and mature arteries: endothelium, smooth muscle, and matrix. [Review]. *J Cardiovasc Pharmacol* **21**, S11-7.

Li, W. (1997) Image and signal processing in intravascular ultrasound. *dissertation* Erasmus University Rotterdam.

Lie, M., Sejersted, O. M. and Kiil, F. (1970) Local regulation of vascular cross section during changes in femoral arterial blood flow in dogs. *Circ Res* **27**, 727-37.

Litvack, F., Grundfest, W., Eigler, N., Tsoi, D., Goldenberg, T., Laudenslager, J. and Forrester, J. (1989) Percutaneous excimer laser coronary angioplasty [letter]. *Lancet* **2**, 102-3.

Liu, S. Q. (1998) Prevention of focal intimal hyperplasia in rat vein grafts by using a tissue engineering approach. *Atherosclerosis* **140**, 365-77.

Maier, S., Meier, D., Boesiger, P., Moser, U. and Vieli, A. (1989) Comparative measurements of the flow in human abdominal aorta with MR and multigate ultrasonic doppler. *Radiology* **171**, 487.

Masawa, N., Glagov, S. and Zarins, C. K. (1994) Quantitative morphologic study of intimal thickening at the human carotid bifurcation: I. Axial and circumferential distribution of maximum intimal thickening in asymptomatic, uncomplicated plaques. *Atherosclerosis* **107**, 137-46.

Mattsson, E. J., Kohler, T. R., Vergel, S. M. and Clowes, A. W. (1997) Increased blood flow induces regression of intimal hyperplasia. *Arterioscler Thromb Vasc Biol* **17**, 2245-9.

McIntire, L. V. (1994) 1992 ALZA Distinguished Lecture: bioengineering and vascular biology. *Ann Biomed Eng* **22**, 2-13.

Meier, D., Maier, S. and Boesiger, P. (1988) Quantitative flow measurements on phantoms and on blood vessels with MR. *Magnetic resonance in medicine* **8**, 25-34.

Meng, X., Mavromatis, K. and Galis, Z. S. (1999) Mechanical stretching of human saphenous vein grafts induces expression and activation of matrix-degrading enzymes associated with vascular tissue injury and repair [In Process Citation]. *Exp Mol Pathol* **66**, 227-37.

Mintz, G. S., Kent, K. M., Pichard, A. D., Popma, J. J., Satler, L. F. and Leon, M. B. (1997) Intravascular ultrasound insights into mechanisms of stenosis formation and restenosis. *Cardiol Clin* **15**, 17-29.

Mintz, G. S., Kovach, J. A., Javier, S. P., Ditrano, C. J. and Leon, M. B. (1993) Geometric remodeling is the predominant mechanism of late lumen loss after coronary angioplasty. *Circulation* **88**, I-654(abst).

Moore, J., Jr., Xu, C., Glagov, S., Zarins, C. K. and Ku, D. N. (1994) Fluid wall shear stress measurements in a model of the human abdominal aorta: oscillatory behavior and relationship to atherosclerosis. *Atherosclerosis* **110**, 225-40.

Muhlestein, J., Zhang, Q., Parker, D., Horn, S., Parker, D. and Anderson, J. (1997) A comparison of the accuracy and reproducibility of digital three-dimensional coronary artery reconstructions using edge detection or videodensitometry. *Comput Biomed Res* **30**, 415 -26.

Ono, O., Ando, J., Kamiya, A., Kuboki, Y. and Yasuda, H. (1991) Flow effects on cultured vascular endothelial and smooth muscle cell functions. *Cell Struct Funct* **16**, 365-74.

Parker, D., Pope, D., Van Bree, R. and Marshall, H. (1987) Three-dimensional reconstruction of moving arterial beds from digital subtraction angiography. *Comput Biomed Res* **20**, 166-85.

Post, M. J., Borst, C. and Kuntz, R. E. (1994) The relative importance of arterial remodeling compared with intimal hyperplasia in lumen renarrowing after balloon angioplasty. A study in the normal rabbit and the hypercholesterolemic Yucatan micropig [see comments]. *Circulation* **89**, 2816-21.

Predel, H. G., Yang, Z., von Segesser, L., Turina, M., Buhler, F. R. and Luscher, T. F. (1992) Implications of pulsatile stretch on growth of saphenous vein and mammary artery smooth muscle. *Lancet* **340**, 878-9.

Redmond, E. M., Cahill, P. A. and Sitzmann, J.V. (1997) Flow-mediated regulation of endothelium receptors in cocultered vascular smooth muscle cells: an endothelium-dependent effect. *Vasc. Res.* **34**, 425-435.

Reneman, R. S., van Merode, T., Hick, P. and Hoeks, A. P. (1986) Cardiovascular applications of multi-gate pulsed Doppler systems. *Ultrasound Med Biol* **12**, 357-70. Reneman, R. S., van Merode, T., Hick, P. and Hoeks, A. P. (1986) Cardiovascular applications of multi-gate pulsed Doppler systems. *Ultrasound Med Biol* **12**, 357-70.

Resnick, N., Yahav, H., Khachigian L. M., Collins, T., Anderson, K. R., Dewey F. C. and Gimbrone, M. A. (1997) Endothelial gene regulation by laminar shear stress. *Analytical and Quantitative Cardiology* **chapter 13**, 155-164.

Rittgers, S. E., Fei, D.Y., Kraft, K. A., Fatouros, P. P. and Kishore, P. R. S. (1988) Velocity profiles in stenosed tube models using magnetic resonance imaging. *Transactions of the ASME* **110**, 180-184.

Ross, R. (1976) The pathogenesis of atherosclerosis (first of two parts). *NEJM* **295**, 369-425.

Sabbah, H. N., Khaja, F., Brymer, J. F., Hawkins, E. T. and Stein, P. D. (1984) Blood velocity in the right coronary artery: relation to the distribution of atherosclerotic lesions. *Am J Cardiol* **53**, 1008-12.

Sabbah, H. N., Khaja, F., Hawkins, E. T., Brymer, J. F., McFarland, T. M., van der Bel-Kahn, J., Doerger, P. T. and Stein, P. D. (1986) Relation of atherosclerosis to arterial wall shear in the left anterior descending coronary artery of man. *Am Heart J* **112**, 453-8.

Salam, T., Lumsden, A., Suggs, W. and Ku, D. (1996) Low shear stress promotes intimal hyperplasia thickening. *Journal of vascular investigation* **2**, 12-22.

Sawchuk, A., Unthank, J., Davis, T. and Dalsing, M. (1994) Prospective, in- vivo study of the relationship between blood-flow hemodynamics and atherosclerosis in a hyperlipidemic swine model. *Journal of vascular surgery* **19**, 58-64.

Serruys, P., de Jaegere, P., Kiemeneij, F., Macaya, C., Rutsch, W., Heyndrickx, G., Emanuelsson, H., Marco, J., Legrand, V., Materne, P., Belardi, J., Sigwart, U., Colombo, A., Goy, J., van den Heuvel, P., Delcan, J. and Morel, M. (1994) A comparison of balloon-expandable-stent implantation with balloon angioplasty in patients with coronary artery disease. *N Engl J Med* **331**, 489-495.

Serruys, P. W., Strauss, B. H., Beatt, K. J., Bertrand, M. E., Puel, J., Rickards, A. F., Meier, B., Goy, J. J., Vogt, P., Kappenberger, L. and et al. (1991) Angiographic follow-up after placement of a self-expanding coronary-artery stent [see comments]. *N Engl J Med* **324**, 13-7.

Sigwart, U., Puel, J., Mirkovitch, V., Joffre, F. and Kappenberger, L. (1987) Intravascular stents to prevent occlusion and restenosis after transluminal angioplasty. *N Engl J Med* **316**, 701-6.

Singer, J. R. (1959) Blood flow rates by nuclear magnetic resonance measurements. *Science* **130**, 1652-1653.

Smedby, O., Johansson, J., Molgaard, J., Olsson, A. G., Walldius, G. and Erikson, U. (1995) Predilection of atherosclerosis for the inner curvature in the femoral artery. A digitized angiography study. *Arterioscler Thromb Vasc Biol* **15**, 912-7.

Sprague, E. A., Luo, J. and Palmaz, J. C. (1997) Human aortic endothelial cell migration onto stent surfaces under static and flow conditions. *J Vasc Interv Radiol* **8**, 83-92.

Takahashi, M., Ishida, T., Traub, O., Corson, M. A. and Berk, B. C. (1997) Mechanotransduction in endothelial cells: temporal signaling events in response to shear stress. *J Vasc Res* **34**, 212-9.

Thubrikar, M. J. and Robicsek, F. (1995) Pressure-induced arterial wall stress and atherosclerosis. *Ann Thorac Surg* **59**, 1594-603.

Tortoli, P., Guidi, F., Guidi, G. and Atzeni, C. (1996) Spectral velocity profiles for detailed ultrasound flow analysis. *Member IEEE* **43**, 654-659.

Tortoli, P., Guidi, G., Berti, P., Guidi, F. and Righi, D. (1997) An FFT-based flow profiler for high-resolution in vivo investigations. *Ultrasound Med Biol* **23**, 899-910.

Tronc, F., Wassef, M., Esposito, B., Henrion, D., Glagov, S. and Tedgui, A. (1996) Role of NO in flow-induced remodeling of the rabbit common carotid artery. *Arterioscler Thromb Vasc Biol* **16**, 1256-62.

van Geuns, R. J. M., de Bruin, H. G., Rensing, B. J. W. M., Wielopolski, P. A., Hulshoff, M. D., van Ooijen, P. M. A., Oudkerk, M. and de Feyter, P. (1999) Magnatic resonance imaging of the coronary arteries: clinical results from the three dimensional evaluation of a respiratory gated technique. *Heart* **82**, 515-519.

Vorwerk, D., Redha, F., Neuerburg, J., Clerc, C. and Gunther, R. W. (1994) Neointima formation following arterial placement of self-expanding stents of different radial force: experimental results. *Cardiovasc Intervent Radiol* **17**, 27-32.

Wahle, A., Wellnhofer, E., Mugaragu, I., Sauer, H., Oswald, H. and Fleck, E. (1995) Assessment of diffuse coronary artery disease by quantitative analysis of coronary morphology based upon 3-D reconstruction from biplane angiograms. *IEEE Transactions on medical imaging* **14**, 230-241.

Waters, C. M. (1996) Flow-induced modulation of the permeability of endothelial cells cultured on microcarrier beads. *J Cell Physiol* **168**, 403-11.

Wolinsky, H. (1970) Response of the rat aortic media to hypertension. Morphological and chemical studies. *Circ Res* **26**, 507-22.

Zarins, C. K., Zatina, M. A., Giddens, D. P., Ku, D. N. and Glagov, S. (1987) Shear stress regulation of artery lumen diameter in experimental atherogenesis. *J Vasc Surg* **5**, 413-20.

Zempo, N., Kenagy, R. D., Au, Y. P., Bendeck, M., Clowes, M. M., Reidy, M. A. and Clowes, A. W. (1994) Matrix metalloproteinases of vascular wall cells are increased in balloon-injured rat carotid artery. *J Vasc Surg* **20**, 209-17.

Zempo, N., Koyama, N., Kenagy, R. D., Lea, H. J. and Clowes, A. W. (1996) Regulation of vascular smooth muscle cell migration and proliferation in vitro and in injured rat arteries by a synthetic matrix metalloproteinase inhibitor. *Arterioscler Thromb Vasc Biol* **16**, 28-33.

Effect of Catheter Placement on 3-D Velocity Profiles

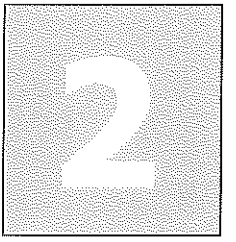

Two Studies based on Computational Fluid Dynamics

Disturbance of 3-D Velocity Profiles Induced by an IVUS Catheter

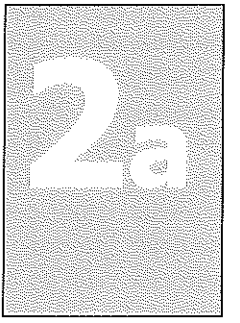

Evaluation with Computational Fluid Dynamics

JJ Wentzel, R Krams, AFW van der Steen, W Li,
EI Céspedes, N Bom, CJ Slager
Comput. Cardiol. IEEE, ***24****, 597-599,1997*

Chapter 2, effect of catheter placement

New IVUS-based blood velocity profile measurements are under development. For these velocity measurements catheter placement in an artery is necessary, but induces disturbances in the native velocity profiles. To what degree the velocity profiles are disturbed by the catheter is studied by computational fluid dynamics. Therefore a straight tube having a catheter inside, is studied for 4 inflow velocities (0.05, 0.1, 0.2, 0.4 m/s) and two catheter positions (in the center and out of the center of the tube). The influence of the catheter size on the velocity profiles is studied as well. Central catheter placement reduced the peak to mean velocity ratio, compared to no catheter inside the tube, by 24%. In contrast, catheter placement out of the center of the tube increased the peak to mean velocity ratio by 14%. These values are independent of the inflow velocities and minimally dependent on changes in catheter size. The shear stress values, however, are dependent on both catheter location and catheter size.

A new technique is under development to measure blood velocity profiles by commercially available IVUS-catheters (Li, 1997). However, the necessity to place the catheter inside the artery when the velocity measurements are performed, might induce disturbances in the velocity profile. The aim of the present report is therefore to better understand the influence of the catheter on the velocity profiles by applying computational fluid dynamics.

2.2.1 Mesh generation

We studied a straight tube with a diameter of $3*10^{-3}$ m and a length of $5*10^{-2}$ m. A catheter was placed either in the center or $0.75*10^{-3}$ m out of the center of the tube. The catheter's diameter was varied from $0.2*10^{-3}$ to $1*10^{-3}$ m and its length was equal to the tube's length. To use a finite element software package to calculate the velocity profiles, the 3-D geometry was filled with 3-D bricks (Figure 1). The tube was divided into 16 cross sections and each cross section consists of 80 bricks. Each brick contains 27 nodes. This resulted in a resolution along the tube of $1.6*10^{-3}$ m and a resolution in a cross section of $0.125*10^{-3}$ m for a central positioned catheter. The resolution in a cross section, when the catheter was positioned out of the center of the tube, ranged from $0.03*10^{-3}$ m to $0.22*10^{-3}$ m, while the axial resolution was unchanged.

2.2.2 Computational fluid dynamics

The incompressible Navier Stokes equations describe the motion of fluids. These differential equations were implemented in each node of the mesh. The Newton-Raphson method was applied to linearize the nonlinear convective terms and the penalty method ($\varepsilon=1*10^{-6}$) was used to obtain the pressure unknowns. We assumed that blood behaves as a Newtonian fluid with a viscosity of $3*10^{-3}$ Pa.s and a density of 1000 kg/m^3. In order to solve these differential equations boundary conditions need to be defined. At the inflow a uniform entrance velocity profile, at the wall no slip condition, and at the outflow zero secondary velocity profiles were assumed ($u_t=0$, $\sigma^{nn}=0$). The numerical accuracy was set to $1*10^{-4}$ m/s and the numerical solution was obtained by a well validated finite element software package (Sepran, Sepra, Leiden, The Netherlands) (Van de Vosse, 1989), which was implemented on a workstation (HP 715/80).

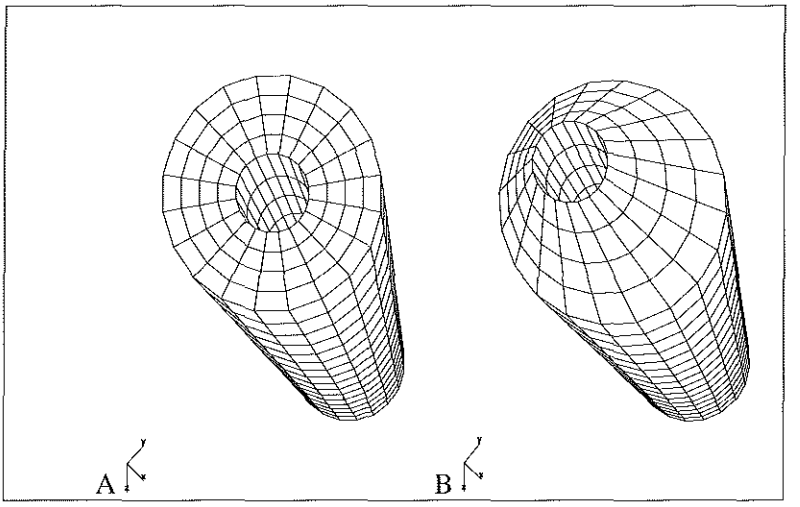

Figure 1: A) 3-D mesh with central positioned catheter B) 3-D mesh with catheter positioned out the of center of the tube.

2.3.1 Numerical accuracy

Numerical checks were performed to be certain that the obtained results are not influenced by numerical inaccuracy. In each of the following cases, results were assumed to be equal when the relative difference between the two situations was less than 1%.

Development of velocity profiles

Development of a uniform entrance velocity profile into a fully developed velocity profile was studied in detail. In case the maximal velocity at the exit of the tube, was less than 1% different from the maximal velocity at the studied cross section, the flow was considered to be fully developed at the studied cross section. Therefore, to study the relative difference at $37.5*10^{-3}$m from the entrance, the relative difference (d_r) was calculated as maximum velocity at $37.5*10^{-3}$ m from the entrance minus maximum velocity at outflow divided by maximum velocity at outflow. The cross section for which the flow was fully developed was defined as C_{dv}. For the catheter placed either in the center or out of the center of the tube, the maximal velocity was given at $25*10^{-3}$ m, $37.5*10^{-3}$m, $46.9*10^{-3}$ m and $50*10^{-3}$ m for four different entrance velocities (see 2.3.2).

Variations in mesh resolution

A reduction of 25% in the cross sectional grid resolution was performed to check the influence of the grid size on our results. In case similar results were obtained for differently sized meshes, we assumed that for the mesh with the highest resolution the results are accurate. The resolution check was applied to a situation with high velocity gradients in one cross section: catheter placed out of the center of the tube with an entrance velocity of 0.2 and 0.4 m/s. In this case each cross section contained 60 bricks consisting of 27 nodes, resulting in a resolution that ranged from $0.04*10^{-3}$ m to $0.29*10^{-3}$ m.

Influence of boundary conditions

To study the influence of the boundary conditions on our data, the boundary conditions defining the outflow were changed from the zero secondary velocity profiles condition ($u_t=0$ and $\sigma^{nn}=0$), to the zero stress outflow condition ($\sigma^{nn}=0$, $\sigma^{tt}=0$). This test was performed on a 3-D mesh with a catheter placed out of the tube's center and with an entrance velocity of 0.4 m/s.

2.3.2 Influence of catheter location and catheter dimension

In a tube with a catheter, placed either in the center or out of the center of the tube, the velocity profiles were calculated for four entrance velocities (0.05, 0.1, 0.2, 0.4 m/s). The catheter diameter was $1*10^{-3}$ m.

The diameter of the catheter was varied from $1*10^{-3}$ m, $0.5*10^{-3}$ m to $0.2*10^{-3}$ m, while the catheter was positioned in the center and out of the center of the tube. The velocity profiles were calculated for an entrance velocity of 0.2 m/s.

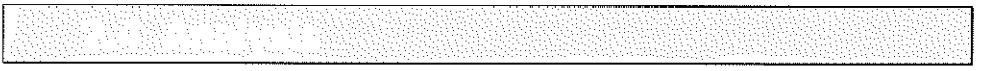

The following parameters were derived from the calculated velocity profiles:

1) velocity ratio: the maximal velocity in the direction of the tube normalized by the mean velocity at C_{dv}
2) normalized shear stress: the shear stress at C_{dv} normalized by the shear stress in case no catheter was inside the tube with the same flow as in the tube with the catheter inside
3) secondary velocity profile.

2.5.1 Numerical accuracy

Development of velocity profiles

Table I shows the maximum velocity in the axial direction at four different locations along the tube for the two geometries and for four different mean velocities. When the catheter is placed in the center of the tube, the maximal velocity at the four locations is always less than 1% different from the maximal velocity at the outflow. For this situation the C_{dv} is at $37.5*10^{-3}$ m. In case the catheter is placed out of the center of the tube, in all conditions except for 0.4 m/s, full development was reached at $37.5*10^{-3}$ m from the entrance, which was used as C_{dv} for further analysis. For 0.4 m/s the cross section at $50*10^{-3}$ m was used as C_{dv} for further analysis.

Variations in mesh resolution

The maximum difference between the velocity, obtained with the high resolution mesh, and the velocity obtained with the low resolution mesh for an entrance velocity of 0.2 m/s is $4*10^{-4}$ m/s. The result for an entrance velocity of 0.4 m/s is $11*10^{-4}$ m/s. Both errors are less than 1% different from the solution obtained with the high resolution mesh.

Influence of boundary conditions

The maximal velocity, obtained with the zero stress outflow condition at C_{dv} is 0.8949 m/s, while the maximal velocity with the zero secondary velocity profiles outflow condition is: 0.8946 m/s. The difference between both velocities was less than 1%.

2.5.2 Influence catheter location and variation in catheter dimensions

Figure 2 and 3 show velocity profiles for a catheter placed respectively in the center and placed out of the center of the tube. The velocity ratio is 1.52 when the catheter is positioned in the center of the tube and 2.28 when the catheter is positioned out of the center of the tube. These ratios are independent of the mean entrance velocity (Table I). The normalized shear stress at the tube's wall, when the catheter is placed in the center of the tube for a mean velocity of 0.2 m/s, is 2.12. Placing the catheter out of the center of the tube the normalized shear stress

Table I: maximum velocities in the axial direction at four locations along the tube specified as distance from the entrance.

V_{mean} (m/s)	maximum velocity (m/s)					
	$25*10^{-3}$ m	$37.5*10^{-3}$ m	$46.9*10^{-3}$ m	$50*10^{-3}$ m	velocity ratio	d_r
	catheter placed in the center of the tube					
0.05	0.0760	*0.0759*	0.0759	0.0759	1.52	<< 1%
0.1	0.1520	*0.1519*	0.1519	0.1519	1.52	<< 1%
0.2	0.3039	*0.3038*	0.3038	0.3037	1.52	<< 1%
0.4	0.6075	*0.6075*	0.6075	0.6075	1.52	<< 1%
	catheter placed out of the center of the tube					
0.05	0.1140	*0.1140*	0.1140	0.1140	2.28	<< 1%
0.1	0.2277	*0.2280*	0.2280	0.2280	2.28	<< 1%
0.2	0.4468	*0.4536*	0.4552	0.4554	2.28	<1%
0.4	0.8394	0.8771	0.8913	*0.8946*	2.24	2%

First column: inflow conditions; second, third, fourth and fifth columns are the different locations along the tube as displayed in the second row; last column: d_r=relative difference; V_{mean}: mean entrance velocity, italic: developed velocity profile: used for analysis.

opposite of the catheter is 1.83. Both normalized shear stress values are independent of the mean velocity.

For the catheter placed in the center, the secondary velocities range from $2.1*10^{-5}$ m/s at an entrance velocity of 0.05 m/s to $6.1*10^{-4}$ m/s for an entrance velocity of 0.4 m/s at C_{dv}. For a catheter placed out of the center of the tube the secondary velocities range from $2.4*10^{-4}$ m/s at an entrance velocity of 0.05 m/s at C_{dv} to $5.1*10^{-4}$ for an entrance velocity of 0.4 m/s at $46.9*10^{-3}$ m.

The variations in catheter size minimally influence the velocity ratio in case the catheter was placed in the center of the tube. The velocity ratio increases up to 1.55 and 1.58 for catheters with a diameter of $0.5*10^{-3}$ m and $0.2*10^{-3}$ m, respectively.

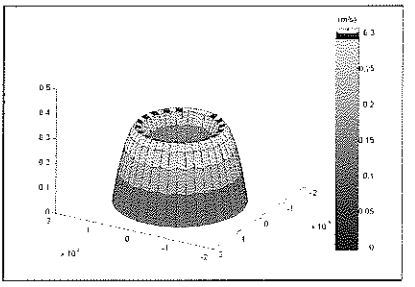

Figure 2: velocity profile for catheter placed in the center of the tube at C_{dv} (entrance velocity: 0.2 m/s)

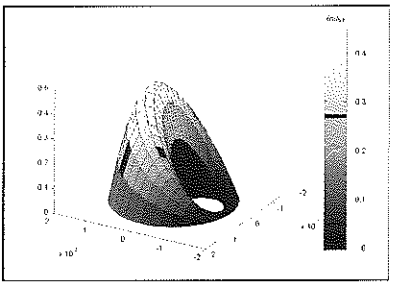

Figure 3: velocity profile for catheter placed out of the center of the tube at C_{dv} (entrance velocity: 0.2 m/s)

Chapter 2, effect of catheter placement

When the catheter is placed out of the center of the tube the velocity ratio decreases from 2.19 to 2.11 for decreasing catheter diameters ($0.5*10^{-3}$ m, $0.2*10^{-3}$ m, respectively).

The normalized shear stress at the tube's wall, in case the catheter is placed in the center of the tube, is 1.50 and 1.26 for catheter diameters of $0.5*10^{-3}$ m and $0.2*10^{-3}$ m respectively. The normalized shear stress becomes: 1.40 and 1.22 for catheter diameters of $0.5*10^{-3}$ m and $0.2*10^{-3}$ m, respectively, when the catheter is placed out of the center of the tube .

During clinical interventions, for instance after PTCA, IVUS-catheters are applied to visualize the vessel wall from inside of the vessel. A new technique is under development (Li, 1997) to measure velocity profiles with an IVUS-catheter at the same location as the imaging is performed. Although blood flow is accurately reflected by this technique (Li, 1997), it is presently unknown how and to what degree the velocity profile is affected by placing the catheter inside the vessel. Hence in this study, the disturbance of the velocity profiles due to catheter placement in a straight tube was investigated. First, some numerical checks were performed. Both the variation in mesh resolution and the boundary conditions did not effect the calculations. Only the check on profile development did not meet the upper limit of 1% for an entrance velocity of 0.4 m/s. For the other inflow conditions velocity profile was fully developed.

For a straight tube without a catheter inside, under steady conditions and sufficient entrance length, velocity develops into a parabolic profile, with a velocity ratio of 2 (Milnor, 1992). When the catheter was placed either in the center or out of the center of the tube, the velocity ratio changed, which implies that the original parabolic profile was altered. Remarkably, the velocity ratio was minimally related to the catheter dimension, but strongly to the catheter location. However, the normalized shear stress was influenced by both the catheter location and the catheter's dimension. Hence, reducing the catheter dimension results in a smaller overestimation of the local shear stress, but minimally alters the measured velocity ratio.

The friction forces are responsible for the low velocity close to the tube's and catheter's wall. When a catheter is placed centrally, this results in a peak velocity distributed over a large area, and to maintain the same flow the peak velocity is reduced. When the catheter is placed out of the center of the tube the resistance in the narrow space between the catheter and the wall, is much higher than in the other part of the cross section and so the same flow has to be transported through a small area which increased the peak velocity.

Flow can be derived from velocity profiles. Only velocity components perpendicular to the studied cross section contribute to the flow through that cross section. However, the current velocity measurements by the new IVUS technique are partially influenced by at least one component of the secondary velocity profiles. For the straight tube no secondary velocity components could be calculated. The observed values are negligible remnants of the selected entrance flow condition. For this situation flow can be measured accurately with this new technique. For curved tubes more research has to be done as in this situation secondary velocities are an essential part of the velocity profile.

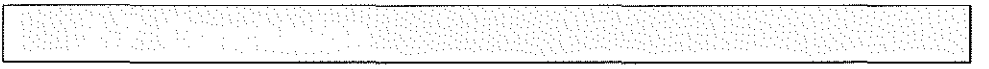

By catheter insertion the original velocity profiles are disturbed. The main factor disturbing the velocity profiles, by catheter insertion, is not the dimension of the catheter but it's location in the artery. However shear stress measurements are influenced by both the catheter location and its diameter.

Li, W. (1997) Image and signal processing in intravascular ultrasound. In *Experimental echography*, pp. 173. Erasmus University Rotterdam, Rotterdam.

Milnor, W. R. (1992) Hemodynamics. In *Hemodynamics*, Wilkins, W. ed, pp. 1-390. Waverly Press Inc., Baltimore.

Van de Vosse, F. N. (1989) A finite element analysis of the steady laminar entrance flow in a 90 curved tube. *Int . J. num. method in fluids* **9**, 275-287.

Effect of Catheter Placement on 3-D Velocity Profiles in Curved Tubes Resembling the Human Coronary System

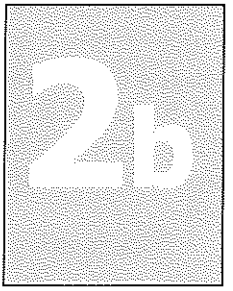

R Krams, JJ Wentzel, I Céspedes, S Carlier, AFW van der Steen, CT Lancée, CJ Slager

Ultrasound Med Biol ***Jun;25(5)****, 803-10, 1999*

Chapter 2, effect of catheter placement

Novel measurement techniques based on IVUS technology ('IVUS-Flowmetry') require the location of a catheter inside the coronary bed. The present study quantifies disturbances in the 3-D velocity profile induced by catheter placement inside a tube, applying computational fluid dynamics. Two curved, circular meshes (curvature κ=0.025 m and κ=0.035 m) with and without a catheter inside the lumen were applied. The catheter was located at the inner curve, the outer curve and at the top position. Boundary conditions were: no slip on the wall, zero stress at the outlet, uniform inflow with entrance velocities of 0.1, 0.2 and 0.4 m/s.

Curvature associated centrifugal forces shifted the maximal velocity to the outer curve and introduced two symmetrical vortices. Additional catheter placement redistributed the 3-D axial velocity field away from the catheter, which was accompanied by the appearance of multiple, low strength vortices. In addition, peak axial velocity increased, peak secondary velocities decreased, axial pressure drop increased and shear stress increased. Flow calculations simulated to resemble IVUS-based flowmetry changed by only 1% after considering secondary velocity.

In conclusion, placement of a catheter inside a curved tube resembling the human coronary system changes the velocity field and reduces secondary patterns. The present study supports the usefulness of catheter based flowmetry during resting flow conditions. During hyperemic flow conditions flow measurements might be accompanied by large axial pressure drops as the catheter itself might act as a significant stenosis.

Steady flow in cylindrical tubes distant from curved segments and side branches may be considered parabolic ("Poisseuille flow"). The velocity field, during these conditions, is described by a velocity vector oriented parallel to the axes of the artery (Milnor, 1982). The human arterial system, however, is a complex three dimensional (3-D) structure consisting of straight and curved segments with multiple side branches (Milnor, 1982). During these circumstances, non-axially directed velocity components ('secondary velocity') have been identified (Kilner, *et al.,* 1993; Moore *et al.,* 1992). These secondary velocities might be implicated in the progression of atherosclerosis and might affect the ultrasonic measurement of blood flow (Tortoli *et al.,* 1995; Li *et al.,* 1998; Carlier *et al.,* 1998).

In general, blood flow measurement techniques measure blood velocity in the direction of the ultrasound beam and assume *Poisseuille* blood flow in order to evaluate flow (Tortoli *et al.,* 1995). Recently, a novel technique for intravascular applications has been developed, that applies a modification of the transit time method to estimate local blood velocity (Li *et al.,* 1998). Due to its high in-plane resolution, this method not only enables to calculate complete 2-D velocity profiles, but due its combination with intravascular ultrasound one can also measure cross sectional area, which allows the calculation of blood flow (Li *et al.,* 1998).

Early results are very promising (Li *et al.,* 1997, Li *et al.,* 1998), but limitations of the method are still under investigation. One of these limitations might be that velocity in only two directions is estimated, (i.e. along and across the ultrasound beam), thereby missing the circumferential component in the plane of imaging (Li *et al.,* 1997). Hence, velocity components in the axial and in-plane direction cannot be completely separated. Consequently, significant secondary velocities could lead to an overestimation of the true blood flow. One other inherent limitation of the technique is introduced by the presence of the catheter which might increase the pressure gradient or disturb the velocity patterns and preclude the possibility to obtain physiological velocity profiles in vivo (Wentzel *et al.,* 1997).

The aim of the present study was multiple. First, the relative contribution of the secondary velocity components to blood flow is evaluated in curved tubes resembling the curvature of the human coronary arteries (Krams *et al.,* 1997), before and after placement of a catheter. Second, the axial pressure gradient is reported and because the axial pressure gradient is affected by flow, vascular resistance was evaluated. Third, due to the reported effect of shear stress on atherosclerosis, we also evaluated how shear stress is affected by the introduction of a catheter inside the lumen. Finally, in order to understand the nature of these disturbances in more detail, the modulating effect of the degree of curvature, tube diameter to catheter radius and Reynolds number are evaluated on these parameters.

Simulated fluid flow can be studied in detail if the equations of motion are solved. Analytical solutions of these equations are only possible under certain simplified conditions (Bovendeerd *et al.*, 1987). For the present study, these simplified conditions are not met and the full non-linear partial differential ('Navier-Stokes') equations have to be solved numerically (Bovendeerd *et al.*, 1987). The numerical technique is based on the discretization of the region of interest with finite elements ('3-D mesh').

2.10.1 3-D mesh formulation

To resemble the human coronary arteries (Krams *et al.*, 1997) we generated a 3-D geometry consisting of a curved, circular tube with a radius of curvature of either 0.025 or 0.035 m and a diameter of 0.003 m (Figure 1). The resulting vessel segments, which occupied a quarter of a circle, were represented by 16 cross-sections along the tube. This resulted in an axial resolution of $2.45*10^{-3}$ m and $3.45*10^{-3}$ m for radii of curvatures of 0.025 and 0.035 m. In the absence of a catheter, 32 elements were placed in each cross section. When a catheter was located inside the tube, 80 elements were located in each cross section to account for the increased geometrical complexities. The cross sectional in-plane resolution was $2.2*10^{-7}$ m^2 for the 3-D mesh without a catheter and $8.9*10^{-8}$ m^2 for a 3-D mesh with a catheter.

2.10.2 Computational fluid dynamics

Each 3-D element of the mesh consists of an isoparametric hexahedral element with 27 nodes per element. At each nodal point, the non-linear partial differential equations ('Navier-Stokes equations') for incompressible, isothermal fluids are implemented. These equations are solved with a standard, finite element method, implemented in the finite element package Sepran (Sepra, Leiden, Netherlands). The non-linear convective term in the Navier-Stokes equations is linearized with a Newton-Raphson approach and solved with a cut-off error of 10^{-4} (m/s). To obtain the pressure unknowns from the discrete Navier-Stokes equations, a penalty function approach was used. Eliminating the pressure unknowns with the penalty method and linearizing of the convective term results in a set of linear equations with velocity unknowns.

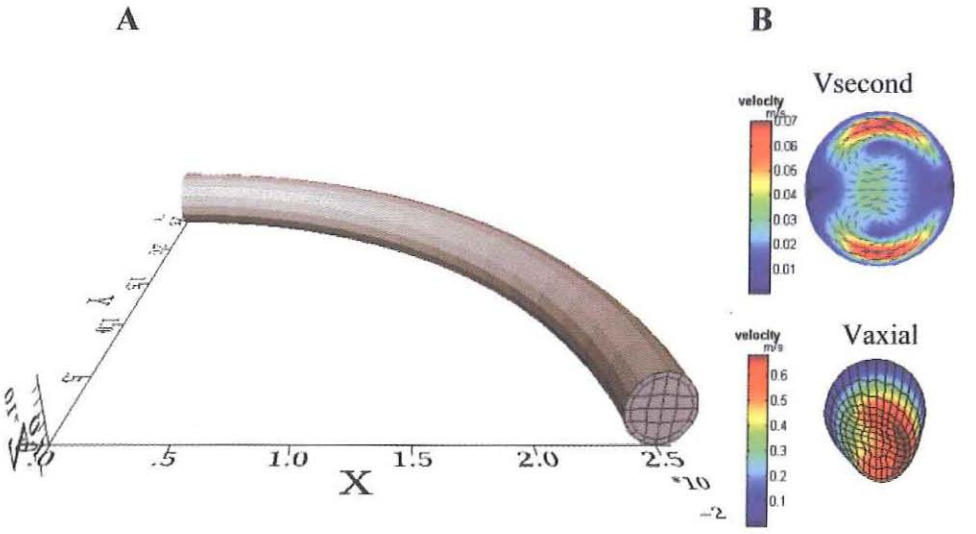

Figure 1: Example of the curved mesh (panel A). Panel B shows the calculated velocity profiles (Vaxial) and secondary velocities (Vsecond).

A numerical solver, applying a direct profile method, of the well-validated (Bovendeerd *et al.,* 1987), commercially available finite element package, which was implemented on a workstation (HP 715/80), solved the resulting matrices.

The following boundary conditions were imposed: uniform steady inflow at the entrance of the vessel, constant zero stress at the outlet and no-slip conditions at the tube wall (Bovendeerd *et al.,* 1987). We further assumed that blood behaved as a Newtonian fluid with a density of 1050 kg/m^3 and a viscosity of $3*10^{-3}$ (Pa.s) (Bovendeerd *et al.,* 1987).

2.11 Protocols and analysis

2.11.1 Adequacy of mesh resolution and fully developed flow conditions

To determine the cross section where flow was fully developed we calculated the relative velocity difference, defined as $(v_i-v_{i-1}/v_{i-1})*100$ %. V_i signifies the points of the 3-D velocity profile at cross section i and V_{i-1} the velocity profile at the previous cross section. A root means squared difference smaller than 1% between successive 3-D velocity profiles was defined as fully developed.

Second, subsequent increments in mesh resolution by 50 % were applied to evaluate whether the lowest mesh resolution was adequate to obtain accurate

solutions. A solution (3-D velocity field), in a given cross section, was defined as accurate when the 3-D velocity field did not change more than 1% after increasing the mesh resolution. The difference between the 3-D velocity fields of both meshes was defined as $(v_l-v_h/v_l)*100$, where l and h refer to the low and high-resolution mesh.

2.11.2 Absence of catheter

3-D velocity vector fields were calculated in curved tubes with radii of curvature of 0.035 m and 0.025 m and a tube diameter of 0.003 m. To cover a wide range of Reynolds values, three different entrance velocities (0.1 m/s, 0.2 m/s and 0.4 m/s) were applied to each radius of curvature adding up to 6 different conditions.

2.11.3 Presence of catheter

We also evaluated to what extent placement of a catheter inside the lumen of a curved tube affected the 3-D velocity field. As idealized for the real situation, we positioned the catheter at the inner curve (9 o'clock), the outer curve (3 o'clock) and at the top (12 o'clock) position of the curved tube. These catheter positions were studied at two different curvatures (0.025 m and 0.035 m) and at three different entrance velocities (0.1, 0.2 and 0.4 m/s). This adds up to 18 different conditions.

2.11.4 Effect of tube size

To study the effect of tube size, we used tubes with a diameter of 0.003 m and of 0.002 m, while catheter diameter was kept constant at 0.001 m. The catheter was located at the outer wall and the radius of curvature was 0.025 m. Entrance velocities were 0.1 m/s, 0.2 m/s and 0.4 m/s.

2.11.5 Analysis

The three-components of the velocity field (u, v and w) were calculated. U and v are the cross sectional in-plane velocity components and w the axial velocity component, (i.e. along the tube). The in-plane velocity vectors u and v were added (vector addition) and are presented as secondary velocity components. Maximal axial ($V_{max,ax}$) and maximal secondary velocity ($V_{max,sec}$) were calculated for each condition and normalized to mean entrance velocity. In addition, the location of the maximal axial velocity component with respect to the center of mass of each cross section was calculated. This location was subsequently normalized to the radius of the tube and presented as percentage shift (%shift).

Comparison between meshes of different size and resolution was accomplished by interpolating the data points of the mesh with the lowest resolution to the mesh with the highest resolution, applying a linear interpolation method (MATLAB, Mathworks Inc, USA).

To simulate conditions resembling IVUS flowmetry we calculated flow in two ways: Total flow was defined as the magnitude of the velocity vector multiplied with the cross sectional area. Axial flow was the product of axial flow and cross sectional area, in which axial velocity was defined as the magnitude of the velocity vector multiplied with normal on the cross section. Due to the discretization of the mesh we defined both parameters locally and summarized over the elements of the mesh. Regional area was calculated as 0.5(|cross(a,b)|+|cross(c,d)|), where a, b, c and d are the sides of a quadrangle in the cross section of interest (cross signifies the vector cross product). Local velocity was calculated from the average of magnitudes of the four velocity vectors located at the vertices of the local area. The error in flow estimation was defined as ((totalflow-axialflow)/totalflow)*100.

Shear stress, calculated from the product of viscosity and the local gradient of the velocity field, was evaluated at the inner and outer curve of the curved tube. For each location, shear stress was normalized to the shear stress values obtained before catheter placement. In addition, a shear stress ratio is defined as the shear stress at the inner curve divided by the shear stress at the outer curve.

The pressure gradient was obtained directly from the output of the FEM package. Pressure difference was the total pressure drop and is reported in mmHg (1 kPa= 7.5 mmHg). To compare different tubes with different lengths, we normalized the pressure difference per length unit (mmHg/10 cm).

Reynolds number ($Re = (v*d*\rho)/\eta$) was calculated during fully developed conditions. In these formulas v signifies the average velocity (m/s), d the tube diameter (m), ρ density (kg/m^3) and η viscosity (Pa.s).

2.12.1 Fully developed flow conditions and adequacy of mesh

The relative difference between the 3-D velocity fields at subsequent cross sections in curved tubes without catheter placement decreased from 7.5% at cross section 2 to less than 1% at cross sections 11 to 14. In addition, increasing the mesh resolution by a factor of 1.5 did not change the 3-D velocity field by more than 1% at cross section 11 to 14. A similar analysis after catheter placement revealed fully development of the velocity field at cross section 5 to 15 and accurate solutions at cross sections 9 to 14. Hence, cross section 12, which corresponds to an axial distance of 0.0295 m (± 10 times the diameter), was used throughout the present analysis.

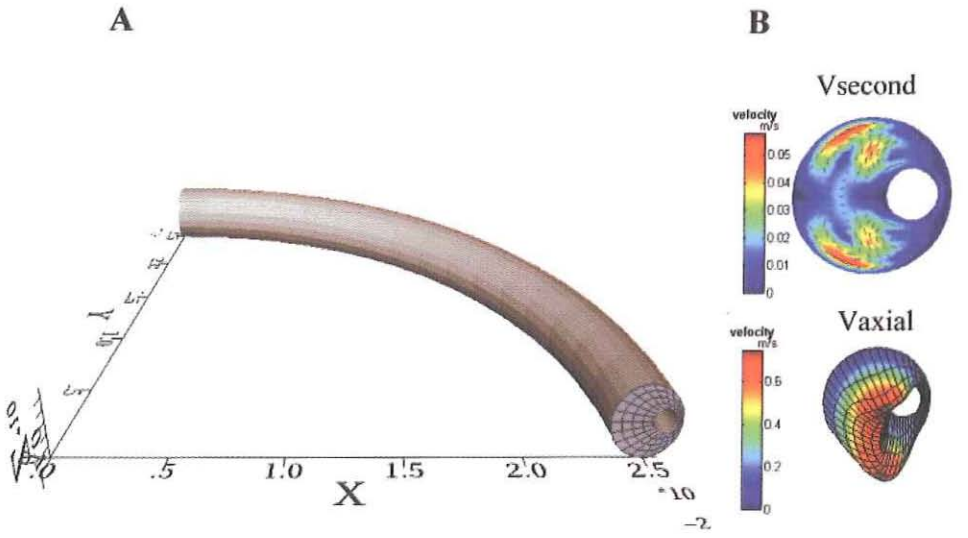

Figure 2: Example of the curved mesh with a catheter located in the outer curve (panel A). Panel B shows the calculated 3-D velocity profiles in the axial direction (Vaxial) and secondary velocities (Vsecond).

2.12.2 Axial velocity

In the absence of a catheter the interplay of viscous, inertial and centrifugal forces in the curved tube redistributes the 3-D velocity field such that maximal axial velocity ($V_{max,ax}$) is shifted outward (Figure 1 and Figure 3, upper row and Table 1). The outward shift increases linearly with entrance velocity, but is unaffected by the radii of curvature as applied in the present study (Table 1). Insertion of a catheter modulates the distribution of the axial velocity field (Figure 3, first column) in such a way that maximal axial velocity is shifted more outward when the catheter is in the inner and top position. When the catheter is in the outer curve the velocity field is shifted towards the inner curve, introducing high gradients on the tube wall (Figure 2 and Figure 3, first column and Table 1). The location (%shift) of the maximal axial velocity is hardly affected by entrance velocity after the insertion of a catheter (Table 1).

$V_{max,ax}$ increased in parallel with entrance velocity and after catheter placement (Table 1). The largest increase of $V_{max,ax}$, at a constant entrance velocity, was calculated when the catheter was located in the inner curve (22%, Table 1), smaller increments were calculated when the catheter was in the top (18%, Table 1) and outer position (12%, Table 1).

Table 1: Characteristic parameters obtained from the 3-D velocity field obtained from the solutions of the Navier-Stokes equations

	Curvature 0.025 m			*Curvature 0.035 m*		
	$Shift_{ax}$(%)	*$V_{max,ax}$(m/s)*	*$V_{max,sec}$(m/s)*	*$Shift_{ax}$(%)*	*$V_{max,ax}$(m/s)*	*$V_{max,sec}$(m/s)*
No catheter						
0.1 m/sec	8	0.19	0.0115	8	0.19	0.0088
0.2 m/sec	11	0.36	0.0334	11	0.37	0.0260
0.4 m/sec	15	0.68	0.0730	15	0.69	0.0586
Catheter out						
0.1 m/sec	14	0.22	0.0092	14	0.22	0.0070
0.2 m/sec	14	0.40	0.0254	14	0.41	0.0197
0.4 m/sec	17	0.74	0.0578	17	0.76	0.0451
Catheter in						
0.1 m/sec	16	0.23	0.0094	16	0.23	0.0074
0.2 m/sec	20	0.44	0.0274	20	0.44	0.0226
0.4 m/sec	20	0.83	0.0677	20	0.83	0.0571
Catheter top						
0.1 m/sec	17	0.22	0.0097	16	0.22	0.0075
0.2 m/sec	20	0.43	0.0311	17	0.44	0.0232
0.4 m/sec	17	0.81	0.0710	17	0.83	0.0572

% shift; relative position of maximal axial velocity with respect to the center of the tube (%); $V_{max,ax}$ magnitude of maximal axial velocity (m/s); $V_{max,sec}$ magnitude of maximal secondary velocity (m/s).

2.12.3 Secondary velocity

In the absence of a catheter, two symmetrical vortices appeared at cross section 12 for both curvatures (Figure 1 and Figure 3, first row and second column). The distribution of these secondary velocity patterns and the maximum of the secondary velocity field were affected both by entrance velocity ($V_{max,sec}$, Table 1) and by curvature (Table 1). Placement of a catheter either at the inner wall or at the top position shifted the vortices further outward, placement at the inner curve moved the vortices towards the inner curve (Figure 3, second column).

Relative secondary velocities, (i.e. normalized to mean axial velocity), varied between 11 to 19 % in the absence of a catheter and between 9 and 18% after introduction of a catheter (Table 1). Hence, the catheter reduced secondary velocities.

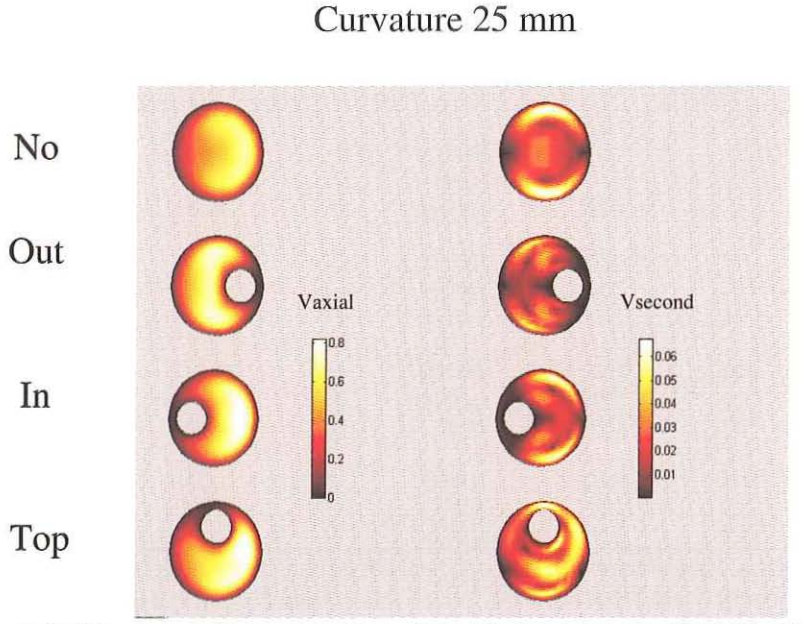

Figure 3: Color-map and iso-contour lines of the 3-D Axial Velocity Field (First Column) and 3-D Secondary Velocity Field (Second Column) at a curvature of 25 mm. The upper row is in the absence of a catheter (NO), the second row a catheter in the outer position (OUT), the third row in the inner position (IN) and the bottom row for a catheter in the top position (TOP). Vaxial is the axial velocity (m/s); Vsecond signifies the secondary velocities (m/s).

2.12.4 Flow calculations

The ratio of axial regional flow over flow varied between 0.5 and 1% and remained in this range after catheter placement. Neither the different entrance velocity nor the placement of a catheter affected these values.

Shear stress

In the absence of a catheter, shear stress was higher in the outer curve as compared to the inner curve leading to shear stress ratios of 1.44 for 0.025 m and 1.37 for 0.035 m curvatures for an entrance velocity of 0.1 m/s. In addition, the shear stress ratio increased to 2.00 and 2.39 with entrance velocity to 0.2 m/s and to 0.4 m/s for 0.025 m curvatures and to 1.90 and to 2.30 for 0.035 m curvatures. Catheter placement decreases shear stress in its own vicinity and increases shear stress at the opposite free wall (Table 2). Consequently, the shear stress ratio increases to values of 6.67, 7.87 and 8.55 for a catheter located at the inner wall of a 0.025 m curved tube at 0.1, 0.2 and 0.4 m/s entrance velocity. Changes to 1.14, 1.65 and 2.14 for a catheter located in the top position for a 0.025 m curved tube was calculated at 0.1, 0.2 and 0.4 m/s. For a catheter in the outer position,

inner curve shear stress values increased over outer curve shear stress values leading to shear stress ratio's of 0.19, 0.23 and 0.29 (Table 2). Minimal additional differences in the effects were noted for 0.035 m curved vessels.

Pressure gradient and tube resistance

The pressure difference calculated along the entire tube varies linearly with entrance velocity from 0.4 to 4.2 mmHg (Table 2). For comparison, between 0.025 m and 0.035 m curved tubes, we corrected the pressure difference for the different length of the tubes (Figure 4). Catheter placement approximately doubles the normalized pressure gradient at each entrance velocity for tubes of 0.003 m. For tubes of 0.002 m in diameter a 7-fold increase in normalized pressure difference was noted (Figure 4). Note that tube resistance, which is the ratio of pressure gradient over flow, increases with entrance flow: 6.8, 8.7 and 10.4 mmHg*s/m^2, i.e. 267%, 271% and 259% at 0.1, 0.2 and 0.4 m/sec entrance velocity for tubes of 0.003 m, independently of catheter location. For the 0.002 m tube, resistance increases up to 38.2 mmHg*s/m^2.

The complex velocity patterns that have been identified in the arterial bed of humans (Milnor *et al.*, 1982; Kilner *et al.*, 1993; Moore *et al.*, 1992) are of significance because specific characteristics of those velocity patterns have been associated with the progression and regression of atherosclerosis (Kilner *et al.*, 1993; Moore *et al.*, 1992). At present, the Doppler based methods assume Poisseuille flow conditions to calculate particle velocity from the Doppler shift. Recently, a novel technique, based on IVUS technology, has been developed that overcomes the simplifications induced by the Doppler methods (Li *et al.*, 1998).

Some potential limitations of this novel method are currently under investigation. In this paper, we consider the fact that secondary velocity is not fully taken into account (Li *et al.*, 1998) and secondly that the catheter itself disturbs the velocity profile. We applied a computational fluid dynamical (CFD) technique to quantify these effects. We will first discuss disturbances induced in the 3-D velocity field, followed by the effect on shear stress, flow and the pressure difference.

2.13.1 3-D velocity field

With laminar flow, in a straight tube with a Newtonian fluid, the velocity profiles are parabolic without secondary velocity components. In curved vessels, the 3-D velocity profile is distributed towards the outer curve, a phenomenon that is accompanied by secondary velocities.

Table 2: Shear stress and axial pressure gradient calculated from the solutions of the Navier-Stokes equations.

	Curvature 0.025 m				*Curvature 0.035 m*		
	SS_{in} (N/m^2)	SS_{out} (N/m^2)	Δp_3 *(mmHg)*	Δp_2 *(mmHg)*	SS_{in} (N/m^2)	SS_{out} (N/m^2)	Δp_3 *(mmHg)*
No catheter							
0.1 m/sec	0.727	1.049	0.40	n.a.	0.727	0.996	0.53
0.2 m/sec	1.383	2.766	0.95	n.a.	1.380	2.635	1.22
0.4 m/sec	2.679	6.411	2.35	n.a.	2.700	8.199	2.97
Catheter out							
0.1 m/sec	1.117	0.225	0.72	3.55	1.200	0.231	0.96
0.2 m/sec	2.052	0.482	2.02	7.27	2.098	0.491	2.11
0.4 m/sec	3.818	1.107	3.86	15.28	3.890	1.094	4.91
Catheter in							
0.1 m/sec	0.240	1.564	0.68	n.a.	0.206	1.517	1.01
0.2 m/sec	0.513	4.057	1.73	n.a.	0.441	3.863	2.36
0.4 m/sec	1.167	10.010	4.14	n.a.	1.051	10.010	5.27
Catheter top							
0.1 m/sec	1.119	1.271	0.75	n.a.	1.111	1.243	0.98
0.2 m/sec	2.116	3.484	1.70	n.a.	2.100	3.291	2.20
0.4 m/sec	4.024	8.595	4.23	n.a.	4.124	8.393	5.33

SS_{in}; shear stress at inner curve (N/m^2); SS_{out} Shear stress at outer curve (N/m^2); Δp_3 and Δp_2 denote the axial pressure differences (mmHg) for tubes of 0.003 m and 0.002 m in diameter, respectively; n.a.: not available.

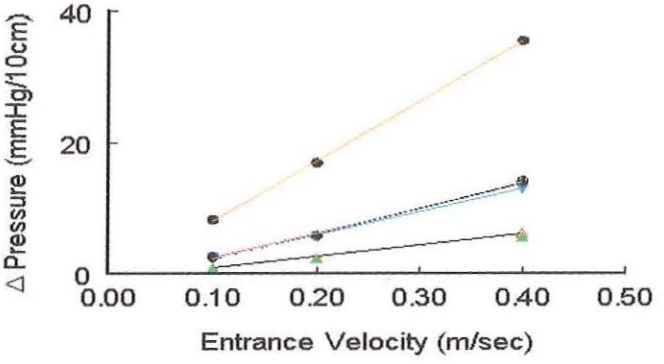

Figure 4: Normalized pressure gradient versus entrance velocity for different conditions. Δ and ▲ denotes absence of catheter;∇ and ▼ denotes catheter in outer curve; ◊ and ♦ denotes catheter in the inner curve; O denotes catheter in the upper position. • Catheter in outer position in 0.002 m tube. Open en closed symbols signify 0.025 and 0.035 m curvatures, respectively.

These secondary velocities arise as a consequence of the curvature-related centrifugal forces acting on the fluid elements in combination with viscous and inertial forces (Bovendeerd *et al.*, 1987; Chang and Tarbell, 1988; Nosovitsky *et al.*, 1997). These forces induce pressure differences perpendicular to the axial direction of the tube, which induces the in-plane velocity ('secondary velocity'). In the present study, secondary velocities in the order of 10-15% were calculated, which is large compared to the values reported by Perktold et.al. (1991). However these authors used smaller curvatures than we did to simulate the coronary epicardial bed. We derived representative curvature values from 3-D reconstructions obtained directly from the coronary system of humans (Krams *et al.*, 1997).

Secondary velocities decreased after inserting a catheter in the curved tubes. Insertion of a catheter also induces a shorter entrance length for flow development. These observations might be due to the existence of an additional boundary layer surrounding the catheter, which reduces the "freedom" to induce in-plane pressure gradients. Support for this explanation is found in the fact that the effect of the catheter is the smallest where the boundary layer is minimal, (i.e. when the catheter is located at the outer curve).

The observation that maximal axial velocity increases after catheter placement, even when normalized for mean velocity might be explained by similar arguments. Due to the additional boundary layer of the catheter, the 'effective' flow region decreases more than is expected on basis of decrements in cross sectional area caused by the insertion of the catheter. Hence, a similar flow has to pass through a smaller region and the fluid elements need a higher velocity.

Because the secondary velocities do not add to the forward flow, we also evaluated their effect on potential errors in volume flow measurements based on transit time velocity measurement technique ("IVUS-Flowmetry"). We calculated that under the present conditions, the secondary velocity components were in the order of 5-15% of total velocity. We calculated a deviation in the flow smaller than 1% when flow calculations based exclusively on axial velocity were compared to flow calculations based on the magnitude of the entire velocity vector. The small error arises because the magnitude of axial velocity is a projection (cosine) of total velocity vector. The estimated angle of the cosine was approximately 8 degrees, which leads to an error of below 1%.

2.13.2 Shear stress and pressure difference

The catheter acts as a long stenosis and, consequently, it affects the pressure gradient in our flow driven system. We calculated an increase in pressure gradient of 2 mmHg for a on area stenosis of 11% (0.001 m catheter in a 0.003 m tube) and of 15 mmHg for an area stenosis of 25% (0.001 m catheter in a 0.002 m diameter tube). This highly non-linear effect can be reconciled by the non-linear

relationship between pressure gradient and area stenosis, which is due to the fourth order relationship between resistance and diameter (Milnor, 1982).

Shear stress at the wall decreases near the catheter, while an increase in shear stress opposite to the catheter position was noted. The latter finding may be explained again by the existence of an additional boundary layer. Therefore, velocity and shear rate decrease near the catheter and increase distant from the catheter. At constant viscosity, shear stress changes in parallel with shear rate.

2.13.3 Limitations of the method

Entrance and outlet conditions and the grid resolution may affect computational fluid dynamics. We tested whether the flow was fully developed to evaluate whether restrictions imposed by the boundary conditions were of importance. It could be shown that the flow field at cross section 12 (60 degrees of the bend) was fully developed and hence independent of axial location in the tube. This finding is in accordance with theoretical estimates of 6 times the radius of the tube for fully flow development, which is equivalent to 0.018 m of arc length (Olsen and Snyder, 1985; Bovendeerd *et al.*, 1987). The cross section of analysis (i.e. cross section 12) was positioned at approximately 0.032 m of arc length. Hence the present analysis is independent of in- and outlet conditions and pertains to steady state conditions. Increasing the resolution of the mesh did not affect the 3-D velocity vector field, at cross section 12 under our conditions, hence the axial velocity component is accurately calculated by this approach.

Although blood is a shear thinning viscoelastic fluid (Krams *et al.*, 1997; Bovendeerd *et al.*, 1987), as a first approach we assumed the fluid applied in the present calculations to be Newtonian. This assumption is not very restrictive, as the velocity gradients of the present calculations are high, especially after catheter placement. Blood can be considered Newtonian for shear rates higher than $100s^{-1}$. Consequently, non-Newtonian effects are expected to be minimal under the present conditions.

Coronary flow and not coronary velocity is kept relatively constant by the impedance of the microcirculation, due to autoregulation. However, the pressure difference calculated in the present conditions were so high that autoregulation would not be able to keep flow constant. Furthermore, the same autoregulation would induce a shear-dependent diameter expansion in the vessel segment under study. Hence, to avoid these complexities, we have assumed constant entrance velocity. Consequently, our data should be interpreted with caution because in practice, both above-mentioned factors (i.e., velocity and shear stress) may change after catheter placement.

We did not include side branches and elasticity of the walls to make the problem easy to solve analytically and numerically (Bovendeerd *et al.*, 1987; Olsen and Snyder, 1985; Berger and Talbot, 1983). In addition, out of plane curvature has been measured in the human coronary system (Asakura and Karino,

1990). The present analysis should therefore be considered as a first order analysis.

In summary, placement of a catheter inside a curved tube resembling the human coronary system affects the distribution of the velocity field, and appears to have a secondary velocity reducing effect. Because the effect of secondary velocity on flow calculations is already small in the absence of a catheter, the present study supports the usefulness of catheter based flowmetry during resting flow conditions. During hyperemic flow conditions flow, calculations might be accompanied by large axial pressure drops because the catheter itself might act as a significant stenosis. This effect is particularly pronounced in small tubes and in the presence of a stenosis. Consequently, hyperemic flow might be reduced despite accurate measurement of flow.

Acknowledgements Financial support from the Intercardiology Institute of the Netherlands for JJ Wentzel (Project 18) is greatly acknowledged.

Asakura, T. and Karino, T. (1990) Flow patterns and spatial distribution of atherosclerotic lesions in human coronary arteries. *Circ. Res.* **66**, 1045-1066,

Berger, S. A. and Talbot, L. (1983) Flow in curved pipes. *Ann. Rev. Fluid. Mech*, **15**, 461- 512.

Bovendeerd, P. H. M., van Steenhoven, A. A., van de Vosse, F. N. and Vossers, G. (1987) Steady entry flow in a curved pipe. *J. Fluid. Mech* **177**, 233-246.

Carlier, S. G., Li, W., Céspedes, E. I., van der Steen, A. F. W., Hamburger, J. N., Bom, N. and Serruys, P W . (1998) Simultaneous morphological and functional assesment of a renal artery stent intervention with intravascular ultrasound. *Circulation* **97**, 2575-2576.

Chang, L. J. and Tarbell, J. M. (1988) A numerical study of flow in curved tubes simulating coronary arteries *J. Biomechanics* **21**, 927-937,

Kilner, P. J., Yang, G. Z., Mohiaddin, R. H., Firmin, D. N. and Longmore, D. B. (1993) Helical and retrograde secondary flow patterns in the aortic arch studied by three directional magnetic velocity mapping. *Circulation* **88**, 2235 -2247.

Krams, R., Wentzel, J. J., Oomen, J. A. F., Vinke, R., Schuurbiers, J. C. H, De Feyter, P. J., Serruys, P. W. and Slager, C.J. (1997) Evaluation of endothelial shear stress and 3D geometry as factors determining the development of atherosclerosis and remodeling in human coronary arteries. *Arterioscl Trombosis and Vasc. Biology* **17**,2061-2066.

Li, W., van der Steen, A. F., Lancée, C. T., Céspedes, I. and Bom, N. (1998) Blood flow imaging and volume flow quantitation with intravascular ultrasound. *Ultrasound Med. Biol.* **24**, 203-214.

Li, W., van der Steen, A. F., Lancée, C. T., Céspedes, E.I., Carlier, S., Gussenhoven, E. J. and Bom, N. (1997), Potential of volumetric blood flow measurements. *Sem. Interv. Cardiol.* **2**, 49-54.

Milnor, W. R. In Hemodynamics. Williams and Wilkins, Baltimore, MD 21202, USA, 1982.

Moore, J. F., Ku, D. N., Zarins, C. U. and Glagov, S. (1992) Pulsatile flow visualization in the abdominal aorta under differing physiological conditions: implications for increased susceptibility to atherosclerosis. *J. Biomed. Eng* **114**, 391-397.

Nosovitsky, V. A., Ilegbusi, O. J., Jiang, J., Stone, P. H. and Feldman, C. L. (1997) Effects of Curvature and Stenosis-Like Narrowing on wall shear stress in a coronary artery model with phasic flow. *Comp. And Biom. Res.* **30**, 61-82.

Olsen, D. E. and Snyder, B. (1985) The upstream scale development in curved circular pipes. *J. Fluid Mech* **150,** 139-158.

Perktold, K., Nerem, R. M. and Peter, P. O. (1991) A numerical calculation of flow in a curved tube model of the left main coronary artery. *J. Biomech.* **24**, 175-189.

Tortoli, P,. Guidi, G. and Newhouse, V. L. (1995). Improved blood velocity estimation using the maximum Doppler frequency. *Ultrasound in Medicine and Biology,* **21(4),** 527-532.

Wentzel, J. J., Krams, R., Vinke, R., Oomen, J. A. F., Schuurbiers, J. C. H. and Slager, C. J. (1997) Disturbance of 3D velocity profiles induced by IVUS catheter, evaluation with computational fluid dynamics. *Comput. Cardiol. IEEE* **24**, 597-599.

True 3-D Reconstruction of Coronary Arteries in Patients by fusion of Angiography and IVUS (ANGUS) and its Quantitative Validation

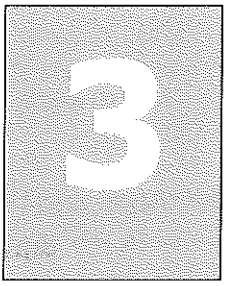

CJ Slager , JJ Wentzel, JCH Schuurbiers, JAF Oomen, J Kloet, R Krams, C von Birgelen, WJ van der Giessen, PW Serruys, PJ de Feyter

Background

True 3-D coronary vessel reconstruction based on intravascular ultrasound (IVUS), requires reconstruction of both the ultrasound beam location and orientation over the pull back trajectory. For this purpose, we developed a new 3-D reconstruction method incorporating angiographic and IVUS information (ANGUS).

Methods and results

First, the pull back trajectory of a sheath based IVUS catheter is predicted from a single set of end-diastolic biplane images to reduce respiratory motion artifacts. R-wave triggering of the IVUS image acquisition eliminates cardiac motion. Secondly, IVUS contours of lumen or stent are obtained and combined with the 3-D trajectory. Quantitative matching of the silhouette of the 3-D reconstruction with the angiogram is used to reconstruct the ultrasound beam orientation. The feasibility and accuracy of ANGUS was tested in 16 patients who were investigated at follow up after stent placement.

Reconstructions were obtained in 12 patients. The accuracy determined by comparing the actual length of the pull back trajectory with the reconstructed path length was good (r =0.99). Computer calculated silhouette images of 3-D catheter, lumen and stent reconstructions correlated closely with the actual X-ray images. Comparing corresponding distances in these images showed correlation factors between 0.84 and 0.97. Multiple measurements of the stent diameters in the 3-D IVUS silhouette images (D_{silh}) almost equaled those in the X-ray images: D_{silh} = 1.02 $D_{x\text{-}ray}$ - 0.06 mm (n = 1106, r = 0.92)

Conclusion

With ANGUS, 3-D reconstructions of coronary arteries can be successfully and accurately obtained in clinical practice.

Intravascular ultrasound (IVUS) generates images with a high temporal and spatial resolution (Nissen *et al.*, 1991; Yock and Linker, 1990) and is useful to evaluate both vessel wall morphology and dimensions before and after catheter-based interventional procedures (Hodgson *et al.*, 1993). Therefore, IVUS imaging is of great value in serial studies, to provide new insights in the process of restenosis (Di Mario *et al.*, 1995), vascular remodeling (Pasterkamp *et al.*, 1995) and progression or regression of atherosclerosis (von Birgelen *et al.*, 1997).

However, IVUS imaging is a tomographic technique, which makes it rather difficult to grasp an overview of an investigated vessel segment. To partly overcome this limitation, multiple images can be acquired during a catheter pull back. 3-D stacking of these images can provide a useful overview of the IVUS information (Kitney *et al.*, 1989; Roelandt *et al.*, 1994; Rosenfield *et al.*, 1991) assuming that the catheter moved along a straight path. However, the catheter generally moves along a curved trajectory and "straight" 3-D reconstructions have a limited applicability. For example, the orientation of eccentric plaques or intimal proliferation cannot be related to characteristics of local vessel curvature. In addition, accuracy of plaque volume quantification (Wiet *et al.*, 1996) decreases when neglecting curvature.

To resolve these shortcomings, 3-D reconstruction methods have been devised that take into account the curved path of the transducer during pull back (Evans *et al.*, 1996; Klein Hans-Martin *et al.*, 1992; Koch *et al.*, 1993). This path was reconstructed from *multiple* biplane X-ray recordings of successive transducer locations. However, some important reconstruction problems such as the determination of the rotation of the IVUS cross sections around the reconstructed path and susceptibility to respiratory motion remained to be solved.

We developed a new 3-D reconstruction method to solve these problems. This method, called ANGUS, combines data from angiographic and ultrasound images (Laban *et al.*, 1995; Slager *et al.*, 1995; Slager *et al.*, 1997) and unlike earlier methods, only a *single* set of biplane images of the IVUS catheter suffices to predict the pullback trajectory. Furthermore, a quantitative technique that compares the silhouette of the IVUS reconstruction with the angiogram was developed, which enables determination of the IVUS cross sectional rotation. The safety, feasibility and accuracy of ANGUS were clinically evaluated.

3.2.1 Basics of true 3-D IVUS reconstruction.

3-D reconstruction requires definition of a 3-D coordinate system in the heart catheterization laboratory. For this purpose, a calibration cube showing x, y and z-axes (length 40 mm) is placed in the isocenter of the X-ray system and recorded in biplane (Figure 1A). When imaging a single point object with this calibrated geometry, the 3-D position of the object can be reconstructed from the biplane images (McKay *et al.*, 1982). In this way, the earlier methods reconstructed the 3-D pull back trajectory from multiple *transducer* positions (Figure 2A). However, artifacts induced by respiration may be severe (Figure 2B). We reconstruct the 3-D position of a sheath based *catheter* (Figure 2C) and use this as a "backbone" for the 3-D vessel reconstruction. This reduces susceptibility to respiratory motion. To reduce the effect of cardiac motion, acquisition of the IVUS images is ECG triggered. Both the catheter and the IVUS images are acquired at the same cardiac phase. This determines the phase of the reconstruction.

Repositioning an IVUS cross section on a reconstructed trajectory involves three steps, which are clearly distinct. *First,* the center of the cross sectional image is translated to a reconstructed transducer location. *Secondly,* at that location (Figure 2D and 2E) the reconstructed IVUS imaging plane is assumed perpendicular to the local trajectory. *Thirdly,* the cross sectional image needs to be rotated around the trajectory to achieve a correct spatial reconstruction. As an example, Figures 2D and 2E show two different rotations. When assuming that images 2C and 2D are observed from a similar point of view, the rotation shown in Figure 2D corresponds best with the actual imaging position I_1. In that case, the thickest part of the wall is located at the inner curve of the pull back trajectory in both images.

3.2.2 In vitro models

To validate the accuracy of catheter reconstruction, a helical wire model (length 100 mm, radius 35 mm, pitch 65 mm) was used on which 11 radio opaque markers were attached at 10 mm intervals.

A second model allowed angiographic and IVUS lumen imaging. This model consisted of a helical gutter (pitch 100 mm) that was machined in the surface of a 120 mm diameter plastic cylinder. The gutter was watertight closed by a flat strip. Consequently, gutter cross sections had a flat side aligned to the cylinder surface. Gutter width and depth were 3 mm. At two locations, small eccentric stenoses were added to the gutter. A 9F catheter introducer sheath was fixed to both ends.

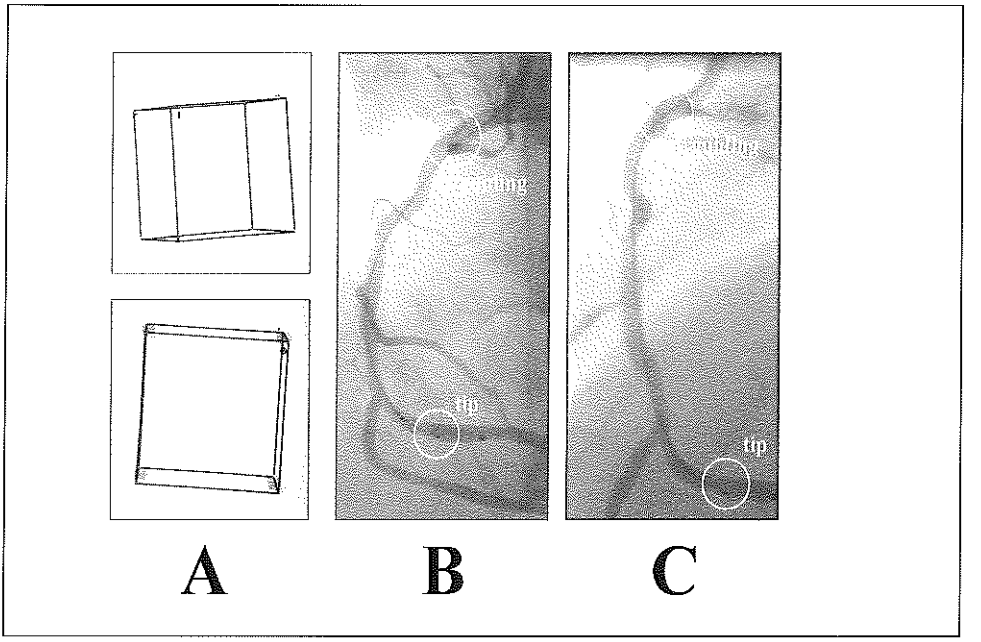

Figure 1: **A** Biplane images of the calibration cube. Top: LAO 19°, Cranial 5°, Bottom: LAO 91°, Cranial 0°. Markers at the origin (large dot) and at the x, y and z axes aid in recognizing the cube's orientation. **B** and **C**. Biplane images of a sheath-based catheter in a right coronary artery just after the start of pull back. The lumen is filled with diluted contrast. The catheter centerlines (corelines) between tip (distal) and guiding entrance (proximal) are used to predict the 3-D path followed by the transducer during pullback.

3.2.3 Patient study

To test the feasibility and accuracy of ANGUS in the clinical setting, 16 patients who gave informed consent, were investigated 6 months after Wallstent implantation in a study that was approved by the institutional medical ethical committee. Vessels studied in these patients were LAD (6), RCA (9) and LCX (1).

3.2.4 Acquisition of X-ray Images

After starting the IVUS pull back, biplane X-ray filming at 25 frames/s (BICOR, Siemens, A.G., Erlangen, Germany) recorded the position of the ultrasound catheter. In addition, an angiogram was made by manually injecting radio opaque dye (Iopamiro 379, Bracco, Italy, diluted with saline in a ratio of 2:1) through the guiding catheter (8F).

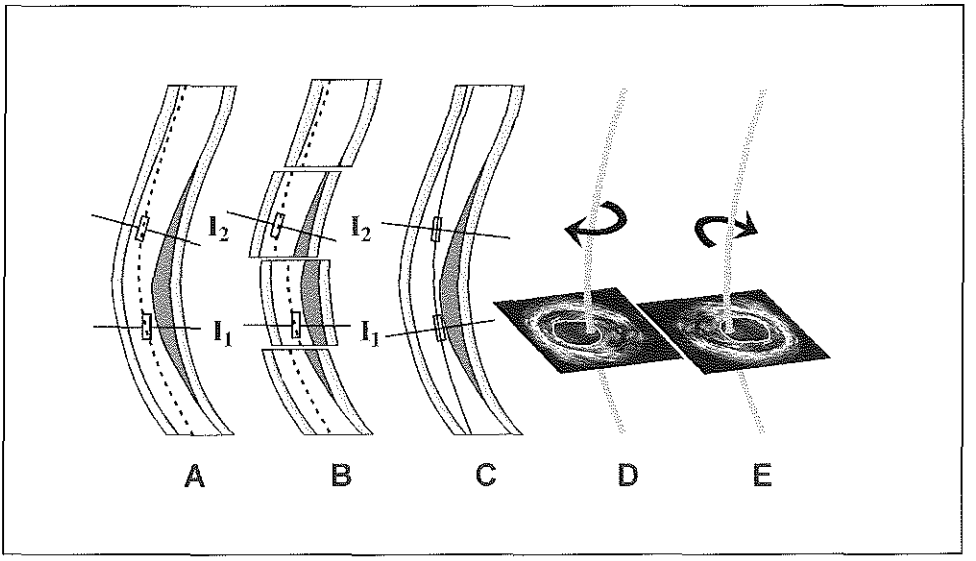

Figure 2: **A** and **C**, show longitudinal cut planes through a vessel for two different types of IVUS catheters. The ultrasound transducer is indicated at two locations. **A** shows a free floating catheter and **C** shows a sheath-based type. The imaging planes ($\mathbf{I_1}$, $\mathbf{I_2}$) are drawn perpendicular to the centerline of the catheter. Note that in **A**, the imaging plane is not necessarily perpendicular to the interpolated path that connects successive transducer positions. **B** shows possible distortion of the path due to cardiac motion induced by respiration. **D** and **E** show in perspective views a 3-D reconstructed catheter coreline and an IVUS cross sectional plane for two arbitrary angular rotations. If **C** and **D** show similar perspective views, the angular rotation shown in **D** is in agreement with the location of the intimal thickening as shown in **C.**

The gutter phantom was filmed in an identical way. Films were stored in DICOM format (8 bits, 512 x 512 pixels) on a compact disk.

To enable synchronization of the X-ray and IVUS images, a multi-channel data acquisition system ACODAS (DATAQ Instruments Inc., Akron, Ohio, USA) was used to record the X-ray flashes. At the end of the investigation, the calibration cube was filmed using the previously stored X-ray geometrical settings. In addition, a flat calibration grid was filmed in contact with the image intensifiers' entrance screens to allow calibration at this level of the imaging chain.

3.2.5 Acquisition of IVUS Images

IVUS images were acquired using a 2.9F sheath based catheter (MicroView, Cardiovascular Imaging Systems, Sunnyvale, California, USA). This catheter has an ultrasound transparent distal sheath that either contains the guide wire (during

catheter introduction) or the rotating imaging core. Imaging is applied with the core rotating at 1800 rpm. Ultrasound frequency is 30 MHz.

IVUS images were acquired at the top of the R-wave of the ECG after detection of a regular R-R interval. Then, the catheter was pulled back by 0.5 mm using a stepping motor (Bruining *et al.*, 1995). Pull back was stopped after the transducer entered the guiding catheter. The electrocardiogram and stepping pulses were recorded by ACODAS for synchronization purposes. IVUS images were stored in digital format (8-bit, 256x256 pixels) in a personal computer. During pull back also a continuous VHS video tape recording was made of all IVUS images.

3.2.6 Processing of X-ray images

From the X-ray recordings, a biplane set of end-diastolic frames was selected that optimally displayed the catheter and the contrast filled lumen. These frames were stored in a personal computer and first used to draw the catheter centerline (coreline) starting at the X-ray opaque tip (distal) until its intersection with the entrance of the guiding catheter (proximal; Figure 1B, 1C). Secondly, the borders of the lumen and the stents were drawn. Drawings were made using custom-made software, which contains special features to aid recognition of image details. Near side branches or border areas being too difficult to interpret, no borders were drawn. In the calibration images, edges of the calibration cube and a 5x5 cm area of the grid were indicated.

3.2.7 Processing of Ultrasound images

To determine borders in the IVUS images a semi-automatic contour detection program was used (Li *et al.*, 1993). This program presents to the operator a cross sectional image and two longitudinal cut planes through the stack of images. As a first step, the program detects contours in the longitudinal views at the interface of lumen to wall and at the external elastic lamina or at the inner border of the stent. From these longitudinal detection results, 4 points become available to start the detection in each cross section. At less well-defined locations, the operator can add corrections. At this stage, display of the IVUS videotape recording significantly aids border recognition. Lumen, stent and external wall contours will respectively be used to 3-D reconstruct the arterial lumen, the stent and the outer vessel border.

For further processing, the contours are described in Fourier terms. In the cross sectional plane, 16 harmonic terms are used and in the axial vessel direction, the number of terms is a quarter of the number of cross sections.

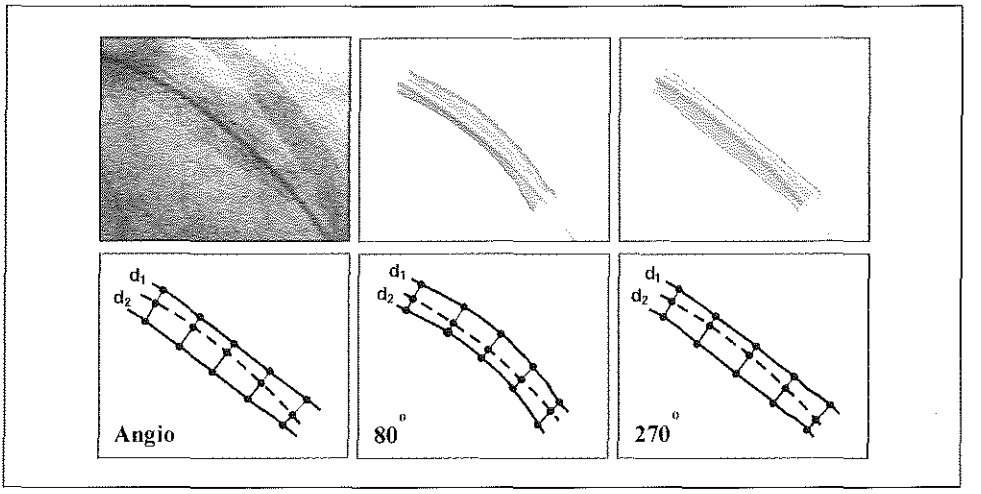

Figure 3: These panels illustrate how the "absolute" angular orientation of the IVUS cross sections can be determined. In the left upper panel, one of the biplane views of a stent is shown. The other top panels show two reconstructions, which started with different angular orientations of the distal contour. The reconstructions are shown from the same point of view as the angiogram. The lower panels illustrate how in the respective projection images, *distances* (d_1, d_2) can be measured from the catheter coreline to the stent border at corresponding locations. Obviously, there is best correspondence between the angio and the 270° reconstruction. Note that for this stent a *diameter* comparison would not be helpful to determine angular rotation

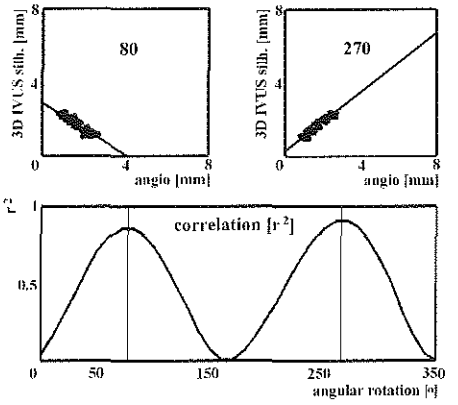

Figure 4: For the stent reconstruction shown in Figure 3, the lower panel shows the squared linear correlation coefficient (r^2) of the comparison between coreline to stent *distances* in the IVUS silhouette and in stent angio images, as a function of angular rotation. As shown in the upper right panel, the peak at 270° has a positive slope. At 80°, a mirror solution with a negative slope is observed.

Both selections imply some filtering of the reconstruction (Laban *et al.*, 1995). Adding surface elements that bridge the gap between successive contours, allow a closed surface description of the reconstruction.

3.2.8 Reconstruction of the catheter centerline (coreline)

The method to reconstruct a *single* point in 3-D space from its biplane projections was introduced by McKay et al. (McKay *et al.*, 1982) and has been adapted by many investigators (Evans *et al.*, 1996; Guggenheim *et al.*, 1992; Klein Hans-Martin *et al.*, 1992; Koch *et al.*, 1993). To determine the involved mathematical descriptions (matrices), at least 6 non-coplanar 3-D calibration points are required. We used the 8 corner points of the calibration cube for that purpose, which were derived from the drawn cube edges.

3-D reconstruction of the *coreline* requires a quite different approach than reconstruction of a single point. First, the only 2 available unique matching points at the ends of the coreline are directly reconstructed in 3-D space. In between these two reconstructed points, a circular segment is defined that serves as a first 3-D approximation for the coreline to be reconstructed. Next, this first approximation is adapted in 3-D in a number of steps (for details see Appendix) until its simulated biplane projections optimally match with the drawings of the coreline. For this matching purpose, 128 points are defined on the 3-D coreline, which projections are compared with the positions of 128 corresponding points assigned to each of the coreline drawings. Root mean square distance between corresponding points specifies the correspondence between both projection images.

The 3-D length of the reconstructed coreline, minus a fixed 8.5 mm (distance from tip to transducer), is compared to the total pull back distance from distal to proximal.

3.2.9 Reconstruction of the cross sectional planes

The locations of the IVUS cross sections along the coreline from distal to proximal are distributed at equidistant intervals. At a reconstructed location, the accompanying cross sectional plane is positioned perpendicular to the coreline. At this phase of reconstruction, the angular rotation of the imaging plane (Fig. 2 D and E) cannot be determined. A first guess for the reconstruction is obtained by choosing an arbitrary angular rotation for the distal imaging plane. From distal to proximal, the orientation of each consecutive plane can be derived from each preceding plane by use of a simple "bending" algorithm (Laban *et al.*, 1995; Prause *et al.*, 1997) that operates in accordance with the bends in the coreline. This algorithm automatically corrects for a twist like phenomenon (Laban *et al.*, 1995) that shows a rotation of the IVUS images when the catheter passes through helical curves (Figure 5A).

3.2.10 Determination of the angular rotation

To check whether the angular rotation of the distal plane makes sense, biplane X-ray shadow images of the reconstructed lumen or stent surface are simulated and compared with the actual X-ray images. In Figure 3, this is illustrated for a stent for two different rotations. To allow a quantitative comparison, distances (d_1, d_2) are measured from the coreline to the stent border in the stent angiogram and in the simulated images. Actually, in each biplane view 60 coreline locations are defined from distal to proximal to measure distances. Thus, a maximum of 240 distance comparisons can be made for the combined biplane views. In general, the actual number will be less because of local omissions in the border drawings. Distance data are normalized to an X-ray geometrical magnification of 1. Then, silhouette dimensions equal those that would be observed on an image intensifier plane located in the isocenter. Correlation between distances is determined by linear regression analysis as a function of the angular rotation in 10 degrees steps. Figure 4 shows the correlation coefficient (squared) as a function of angular rotation for the example of Figure 3. Maximum positive correlation defines the optimal angular rotation of the distal IVUS plane.

3.2.11 Diameter measurements

Adding adjacent distances renders local lumen and stent *diameters* in the projected images. Combining both views, a maximum of 120 diameter measurements can be obtained.

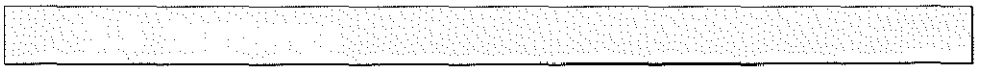

Data are summarized as means ± standard deviation. For determining the relationship between X-ray and IVUS related dimensions in the projection (silhouette) images at optimal angular orientation, orthogonal regression analysis is applied.

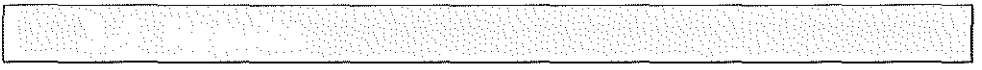

3.4.1 Wire model

The reconstructed "coreline" length was 99.7 mm, which is only 0.3 mm less than the actual 100 mm length of the model. The "coreline" projections showed close matching with the drawn wire centerlines. Root mean square distance between corresponding points was 0.57 mm (n = 256 points).

The projections of the individual markers (22 points) allowed "single point" reconstruction of 11 marker locations in 3-D. The locations of 11 corresponding points *on the reconstructed coreline*, distributed at equal distance intervals were

also calculated. Root mean square distance *in 3-D* between the 11 "coreline" points and the reconstructed marker locations was 0.61 ± 0.36 mm, which is small compared to the 100 mm length of the model.

3.4.2 Gutter model

Length of the reconstructed 3-D coreline from distal to proximal was 108.5 mm. Pull back distance was 106.4 mm. The projections of the reconstructed coreline fitted accurately with the actual drawn corelines. Root mean square distance between both curves was only 0.26 mm (n = 256).

The angiographic coreline to lumen border *distances* (n = 178) compared with those from the simulated gutter projections correlated best ($r^2 = 0.86$) at 80 degrees of angular rotation. This rotation was also found when determining the optimum rotation for the frontal and lateral views separately or when using the combined *diameter* data. For this 80 degrees rotation, comparison between diameters derived from the angiogram and from the 3-D reconstruction silhouette yielded: $D_{silh} = 1.06\ D_{angio} - 0.06$ mm ($r^2 = 0.90$, n= 73).

In Figure 5B and 5C, rendered views are presented of the reconstructed gutter, combined with a cylinder surface having the exact dimensions of the actual model. The magnified views show that the flat sides of the gutter profile at both of its ends are perfectly aligned with the surface of the cylinder. Apparently, the detected angular rotation is correct and the twist observed in the IVUS images (Figure 5A) is correctly handled.

3.4.3 Patient artery reconstructions

Reconstructions of arteries and stents were successfully obtained in 12 patients (7 RCA, 4 LAD and 1 LCX). In all of these patients, angular rotation was determined on the basis of the stent contours. In 4 patients (2 LAD, 2 RCA) inadequate X-ray image quality and choice of projection or 3-D calibration error precluded 3-D reconstruction. Figure 6 shows an example of a reconstructed right coronary artery in lateral projection at optimal angular rotation.

Length of the 12 reconstructed corelines ranged from 36 to 76 mm. Comparing these lengths (L_{core}) with the applied number of pull back steps (n) delivered: $L_{core} = 0.48\ n + 4.1$ mm (r = 0.99).

The projections of the reconstructed 3-D coreline fitted accurately with the drawn corelines. The residual root mean square distances varied from 0.1 to 1.6 mm, averaged for the 12 patients this was 0.65 ± 0.46 mm. In addition to the stent-based angular rotation determination, the lumen angiogram could be used for this purpose in 7 of the 12 patients.

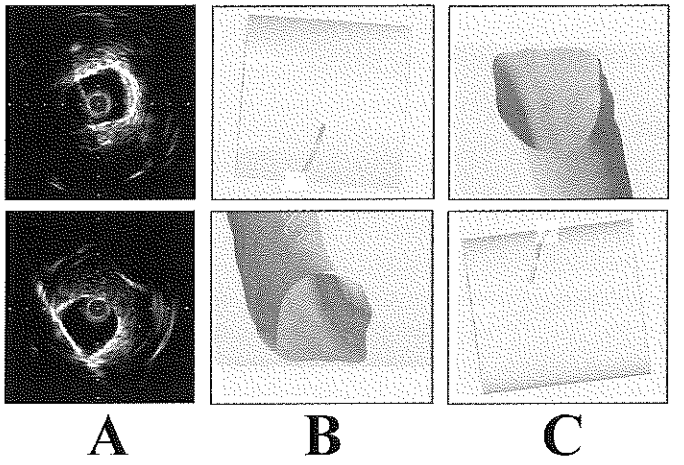

Figure 5: A Between the distal (top) and proximal (bottom) IVUS images of the helical gutter model a twisting like motion is observed during pull back. **B and C**: Rendered views of the cylinder, in which the gutter lumen was machined, combined with the actual ANGUS reconstruction of the gutter. The enlarged distal (B) and proximal (C) lumen ends show how the reconstructed flat side of the lumen is accurately aligned with the cylinder surface. This illustrates that the observed rotation in the IVUS images is correctly handled.

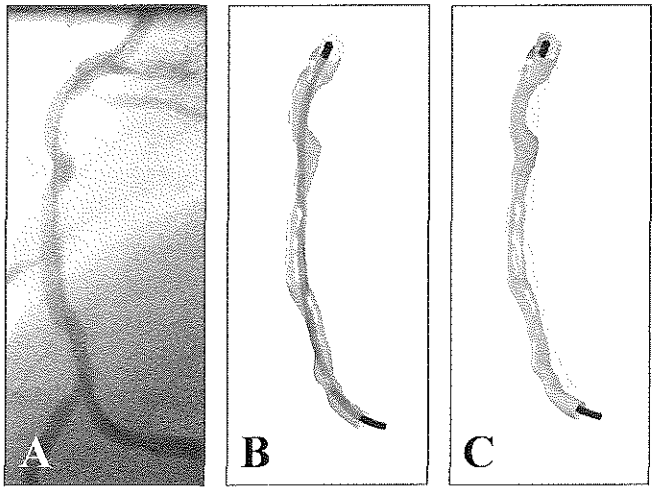

Figure 6: Lateral angiographic view of a right coronary artery (**A**) and the corresponding 3-D lumen reconstruction shown in panel **B**. There is close similarity between the lumen diameters and the position of the catheter coreline relative to the lumen. In panel **C**, the vessel wall is added to the reconstruction.

The absolute difference between stent and angiographically determined rotations was only 17 ± 12°; the mean of the signed differences was 6°.

At optimal *stent-determined* rotation, the 12 distance relations, comparing the stent angiogram with the 3-D silhouette showed correlation coefficients that ranged from 0.84 to 0.97 (average 0.91 ± 0.04). At optimal *lumen-determined* rotation the average correlation of the distance relations was 0.84 ± 0.12, (n=7).

Combining all *in-stent distance* measurements for the 12 patients in a single orthogonal linear regression analysis yielded: $d_{silh} = 0.90\ d_{angio} + 0.19$ mm (n = 2344, r = 0.92) with d_{silh} the distance in the 3-D reconstruction silhouette and d_{angio} the corresponding distance in the stent angiogram (Figure 7). A similar comparison between all *stent diameters* (D) in the 12 patients yielded: $D_{silh} = 1.02\ D_{angio} - 0.06$ mm (n = 1106, r = 0.92) (Figure 7).

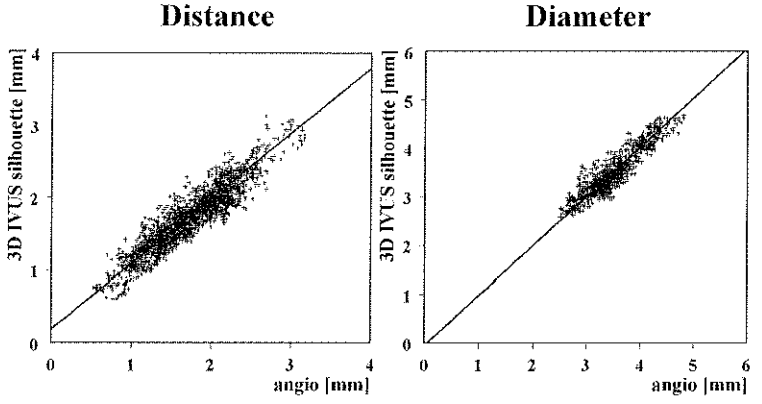

Figure 7: These scatter plots show all distance and diameter data derived from the silhouettes of the 12 patient 3-D stent reconstructions, compared to data from the actual angiographic images. The line fitted through the data is obtained with orthogonal linear regression analysis. For details see text.

3.5.1 Coronary 3-D reconstruction

Several investigators (Muhlestein *et al.*, 1997; Parker *et al.*, 1987; Wahle *et al.*, 1995) utilized coronary biplane angiograms of patients for 3-D reconstruction of the coronary skeleton and/or lumen. However, such lumen reconstructions require assumptions about the shape of the lumen cross sections and therefore have limited applicability. In principle, imaging modalities like MRI and EBT are better designed to perform such a 3-D task. Unfortunately, the relatively low resolution of these techniques limits their use for many coronary applications. Therefore, the combined use of high-resolution intravascular ultrasound imaging and biplane angiography offers an attractive alternative for 3-D coronary artery reconstruction. In particular, the possibility added by IVUS to reconstruct the arterial wall is of great value for many applications.

The first presented 3-D reconstruction methods fusing IVUS and angiography did only partly solve the principal reconstruction problems. For instance, the pull back trajectory was derived from the vessel midline (Klein Hans-Martin *et al.*, 1992), from monoplane (Koch *et al.*, 1993) or from multiple transducer positions (Evans *et al.*, 1996) and angular rotation was not determined. In the present paper, we report on improvements on our first reported solutions (Laban *et al.*, 1995; Slager *et al.*, 1995) for these problems and on the addition of a quantitative approach for the determination of angular rotation. Furthermore, we now have developed a number of tools for contour drawing, image enhancement and automated data collection to allow analysis of images obtained in clinical routine. In this present study we demonstrate that the ANGUS method is able to 3-D reconstruct stent and coronary arteries in clinical practice in the majority of investigated patients with a high accuracy. The applied protocol fitted well in the clinical setting as it barely differs from standard imaging protocols. There was an excellent agreement between details of the reconstruction silhouette and angiographic findings. Very good agreement was also obtained with other 3-D derived data like pull back length of the IVUS catheter and known geometric measures of the investigated phantoms.

3.5.2 Coreline reconstruction

In our initial studies, we used data on the X-ray geometry provided by the biplane system itself. This is most attractive as it may allow 3-D reconstruction on line. However, in our experience, the data provided was too inaccurate. Therefore, we adapted to the use of a calibration cube and the use of transformation matrices (McKay *et al.*, 1982).

Reconstructing the 3-D coreline from its two coreline drawings using the parameter fitting approach (Appendix) produced good results. Probably a reason

for this is that the catheter sheath by its nature straightens as much as possible and thereby prevents the need for reconstructing complex curves. An advantage of the parameter fitting approach is that it automatically guides the 3-D coreline through spatial locations (blind planes (Laban *et al.*, 1995)), which otherwise may pose problems because of ambiguous solutions (Wahle *et al.*, 1995). The accuracy of the reconstructed corelines as determined from its projections was quite satisfactory. The largest deviations were observed in the patients and probably originated from cardiac and/or respiratory motion because the different biplane views differ in time by 20 ms and therefore do not represent the same 3-D catheter position.

The helical wire model with attached markers enabled comparison of points on a *coreline* reconstruction with multiple 3-D "single-point" reconstructed *markers*. The resulting *spatial* error was very small and indicates that for this model good matching in the 2-D projection images is paralleled by an accurate spatial coreline description.

The length of the coreline reconstruction was most accurate in the wire model. The reconstructed length in the gutter model and in the patients slightly exceeded the length derived from the number of pull back steps. As the pull back device was accurately calibrated, the remaining difference may originate from estimating the proximal intersection of the coreline with the guiding catheter in the angiogram. This is complicated by a diminished radio-opacity of the soft tip of the guiding catheter. The distal tip position could be accurately indicated and showed better visibility than the IVUS transducer.

3.5.3 Stent and angiographic matching

In this study, we opted primarily for the reconstruction of stents in patients. This meant that for determining the angular rotation, only stent X-ray images would be needed. Yet, we made a contrast angiogram, because we wished to investigate simultaneously whether the angular rotation could be derived on base of matching with the lumen as well. To enable a comparison between the angular rotations obtained with both matching procedures it was necessary to use the same end diastolic X-ray images. This choice may have contributed to a somewhat lower success rate of both reconstruction procedures. At the one hand, the contrast agent impaired recognition of the stents and on the other hand, the remaining sections to be used for angiographic matching were rather short. Therefore, we expect that when focusing on a single matching procedure the success rate will be higher.

The use of diluted contrast enabled visualization of the catheter and the lumen silhouette in a single image. Another advantage of diluted contrast was its much lower viscosity, which allowed rapid manual injection through the guiding catheter.

The angular rotations determined from both matching procedures agreed closely. This is an important result as the matching structures of the stent and the

angiographic borders were at different positions in the investigated arteries. Therefore, it is unlikely that unpredictable sources of catheter twist remain along the coreline. As is also indicated by the gutter reconstruction, the applied algorithms, which handle geometrical twist (Laban *et al.*, 1995; Prause *et al.*, 1997), lead to excellent matching with known geometrical details. Therefore, we expect that when avoiding reconstruction of tight stenoses, where additional catheter torsion may occur by increased friction, angular rotation can be accurately determined.

In this study, we generally used the distance parameter, i.e. the catheter position relative to the lumen or stent border, to determine angular rotation. Indeed, for a catheter positioned in the center of the stent for both projections, no information can be obtained. Obviously, this situation will rarely happen. The stent diameters are less well suited for matching, as their silhouette will not change much when varying angular rotation. For angiographic matching, the diameters of the lumen silhouette may serve well because they generally show a wide variation for different angular rotations. This is confirmed by the good results for diameter matching obtained in the gutter model.

Our experience with the angiographic matching procedure further taught us that there was a lack of contrast between the catheter and the arterial wall for gaps getting smaller than 0.5 mm. We therefore excluded those areas from our analysis. Interestingly, because of observing a local mismatch between the angio and 3-D reconstruction silhouette, sometimes we detected lumen areas of eddying or stagnant blood flow in the IVUS images just behind focal stenoses. Otherwise, these areas would have been indicated as soft plaque.

3.5.4 Comparing IVUS and Angio dimensions

At optimal angular rotation, the excellent result of the *distance* comparison (Figure 7) proves that the catheter sheath position at begin of pullback can be used to predict the pull back trajectory. The residual differences, derived from the regression equation are only 0.12 mm for the smallest (0.6 mm) and – 0.12 mm for the largest (3 mm) distances; at the intermediate distance (1.8 mm) no difference is observed. We used orthogonal regression analysis for this combined distance comparison, as this method is independent of the choice for IVUS or angio as the independent variable. We did not use the angiographic data to test the predictive value of the catheter position for the pullback trajectory. Then, other complicating factors play a role like a possible change of state in vasomotion during pull back and less well defined lumen borders for both imaging modalities. One of the mechanical reasons for the observed stability of the sheath position during pull back, is that the sheath strives to a condition of minimal bending energy. This condition is not much influenced by the insertion depth of the imaging core, which has a much higher flexibility than the sheath.

The stent *diameter* comparison (Figure 7) between the IVUS 3-D reconstruction silhouettes and the actual angiograms shows that no important calibration errors seem to exist in the IVUS nor in the angio imaging system. The orthogonal regression equation shows an almost exact 1 to 1 slope and an almost zero intercept. Part of the remaining error may have been introduced by indicating the stent in the IVUS images at the inner border, while in the angiogram the midline of the stent wires is indicated. This difference could explain a negative intercept of approximately 0.1 mm, i.e. one stent wire diameter.

The random error in the distance and diameter comparisons can be estimated from the standard error of the estimate, which is 0.17 mm and 0.19 mm respectively. Sources of this error are first the uncertainties in both the angiographic and IVUS border determination. Secondly, differences in determining corresponding distance measurement locations will exist. Thirdly, particularly in the borders drawn in the angiogram, digitization noise cannot be neglected.

3.5.5 Limitations

One of the most obvious restrictions of the current arterial reconstruction method is its inability to include side branches. Although not being a limitation of the ANGUS method, in this study we only reconstructed the end diastolic vessel geometry.

3.5.6 Applications

True 3-D reconstructions of arterial lumen and wall have the possibility to study in vivo spatial characteristics of lesions, which previously was not possible. Particularly, a comparison between these characteristics with hemodynamic parameters like shear stress, derived from numerical computational flow simulations applied to the reconstructed lumens, opens new ways for many interesting studies (Krams *et al.*, 1997). Application of true 3-D reconstruction methods will also help to enhance accuracy in plaque volume estimation and in calculating the spatial distribution of radiation dose in the field of radiation therapy.

3.5.7 Conclusion

3-D reconstruction of coronary arteries by ANGUS can be applied in clinical practice with a high rate of success and with high accuracy as the path followed by a sheath based IVUS catheter can be predicted with high accuracy from a single set of biplane angiographic images. Both location and angular orientation of IVUS images can be accurately derived from a quantitative comparison of the 3-D reconstruction silhouette with the angiogram. IVUS derived Wallstent diameters as measured in the 3-D reconstruction silhouette equal those derived from the angiogram.

Chapter 3, quantitative validation

The contribution of the catheterization laboratory technicians and nurses in improving and implementing the protocol is greatly acknowledged. The authors also thank Andrew Tjon and Harry Achterberg for their contribution in implementing and improving the analysis procedures.

The searched 3-D coreline is described as a series of points in 3-D space along a spatial curve using parameter n. The present description slightly differs from that in the earlier paper (Laban *et al.*, 1995). For n = 0, 1/127, 2/127, ..., 1 a total of 128 vector points **P** (n) are defined according to:

$$\mathbf{P}(n) = \mathbf{A} + n\mathbf{B} + \mathbf{C}\sin n\phi_s + \mathbf{D}\cos n\phi_s + \mathbf{E}\sin 2n\phi_s + \mathbf{F}\cos 2n\phi_s + \mathbf{G}\sin 3n\phi_s + \mathbf{H}\cos 3n\phi_s$$

Angle ϕ_s and vectors **A**, **B**, **C**, ... **H** have to be determined. The terms **C** sin $n\phi_s$ and **D** cos $n\phi_s$ describe a segment of an elliptical curve in 3-D. Angle ϕ_s determines this segment, for $\phi_s = 360^0$ a full ellipse is described. Vector **A** is a displacement vector. The incremental vector n**B** adds pitch to enable description of helical curves. The terms preceded by **E**, **F**, **G** and **H** allow description of higher order details.

As a first approximation of **A**, **C**, **D** and ϕ_s (other coefficients are set to zero) it is assumed that the curve is a circular segment passing through the 3-D reconstructed distal and proximal end-points of the coreline and a third intermediate 3-D point. The latter point is reconstructed from two points indicated at the middle of the coreline drawings. The biplane projections of the 128 curve points are calculated and compared with the actual drawn 2-D corelines. For this purpose, the drawn corelines are also sampled at 128 points that are spaced at *similar relative distances* as the projected curve points. The root mean square of distances between corresponding points provides a cost function, which is minimized by adjusting the unknowns with a Gauss-Newton iterative solver (MATLAB®, The MathWorks, Inc., Natick, MA, USA). After first adjusting **A**, **C**, **D** and ϕ_s, other unknowns are stepwise added and optimized.

Bruining, N., von Birgelen, C., di Mario, C., Prati, F., Li, W., den Hoed, W., Patijn, M., de Feijter, P., Serruys, P. and Roelandt, J. (1995) Dynamic three dimensional reconstruction of ICUS images based on an ECG-gated pull back device. *IEEE Computers in cardiology* **95CH35874**, 633-636.

Di Mario, C., Gil, R., Camenzind, E., Ozaki, Y., von Birgelen, C., Umans, V., de Jaegere, P., de Feyter, P., Roelandt, J. and Serruys, P. (1995) Quantitative assessment with intracoronary ultrasound of the mechanisms of restenosis after percutaneous transluminal coronary angioplasty and directional coronary atherectomy. *Am J Cardiol* **75**, 772-777.

Evans, J., Kok-Hwee, N., Wiet, S., Vonesh, M., Burns, W., Radvany, M., Kane, B., Davidson, C., Roth, S., Kramer, B., Meyers, S. and McPherson, D. (1996) Accurate Three-dimensional reconstruction of intravascular ultrasound data. Spatially correct three-dimensional reconstructions. *Circulation* **93**, 567-576.

Guggenheim, N., Dorsaz, P., Doriot, P., Suilen, C., Chappuis, F. and Rutishauser, W. (1992) 3-D determination of the intravascular volume and flow of coronary arteries. *In: KC Lum et al (editors). MEDINFO 92, Elsevier Science Publ. BV, North-Holland*, 801-807.

Hodgson, J., Reddy, K., Suneja, R., Nair, R., Lesnefsky, E. and Sheehan, H. (1993) Therefore, the aim of our study was to investigate the influence of MMP-inhibition on both the shear stress and wall stress regulation after balloon angioplasty. *J Am Coll Cardiol* **21**, 35-44.

Kitney, R. I., Moura, L. and Straughan, K. (1989) 3-D visualization of arterial structures using ultrasound and voxel modeling. *Int J Card Imaging* **4**, 135-43.

Klein Hans-Martin, Günther, R. W., Verlande, M., Schneider, W., Vorwerk, D., Kelch, J., and Hamm, K. (1992) 3-D-surface reconstruction of intravascular ultrasound images using personal computer hardware and a motorized catheter control. *Cardiovascular and Interventional Radiology* **15**, 97-101.

Koch, L., Kearney, P., Erbel, R., Roth, T., Ge, J., Brenneke, R. and Meyer, J. (1993) Three dimensional reconstruction of intracoronary ultrasound images: roadmapping with simultaneously digitised coronary angiograms. *IEEE Computers in Cardiology*, 89-91.

Krams, R., Wentzel, J. J., Oomen, J. A. F., Vinke, R., Schuurbiers, J. C. H., de Feyter, P. W., Serruys, P. W. and Slager, C. J. (1997) Evaluation of endothelial shear stress and 3D geometry as factors determining the development of atherosclerosis and remodeling in human coronary arteries in vivo. Combining 3D reconstruction from angiography and IVUS

(ANGUS) with computational fluid dynamics. *Arterioscler Thromb Vasc Biol* **17**, 2061-5.

Laban, M., Oomen, J., Slager, C., Wentzel, J. J, Krams, R., Schuurbiers, J., den Boer, A., von Birgelen, C., Serruys, P. and de Feijter, P. (1995) ANGUS: A new Approach to Three-Dimensional Reconstruction of Coronary Vessels by Combined Use of Angiography and Intravascular Ultrasound. *IEEE, Computers in Cardiology* **95CH35874**, 325-328.

Li, W., Bosch, J., Zhong, Y., van Urk, H., Gussenhoven, E., Mastik, F., van Egmond, F., Rijsterborgh, H., Reiber, J. and Bom, N. (1993) Image segmentation and 3-D reconstruction of intravascular ultrasound images. *In: Acoustical Imaging, ed. Y. Wei and B. Gu. Plenum Press, New York*, 489-496.

McKay, S., Potel, M. and Rubin, J. (1982) Graphics methods for tracking three-dimensional heart wall motion. *Comp Biomed Res.* **15**, 455-473.

Muhlestein, J., Zhang, Q., Parker, D., Horn, S., Parker, D. and Anderson, J. (1997) A comparison of the accuracy and reproducibility of digital three-dimensional coronary artery reconstructions using edge detection or videodensitometry. *Comput Biomed Res* **30**, 415 -26.

Nissen, S., Gurley, J., Grines, C., Booth, D., McClure, R., Berk, M., Fischer, C. and DeMaria, A. (1991) Intravascular ultrasound assessment of lumen size and wall morphology in normal subjects and patients with coronary artery disease. *Circulation* **84**, 1087-1099.

Parker, D., Pope, D., Van Bree, R. and Marshall, H. (1987) Three-dimensional reconstruction of moving arterial beds from digital subtraction angiography. *Comput Biomed Res* **20**, 166-85.

Pasterkamp, G., Wensing, P., Post, M., Hillen, B., Mali, W. and Borst, C. (1995) Paradoxical arterial wall shrinkage may contribute to luminal narrowing of human atherosclerotic femoral arteries. *Circulation* **91**, 1444-9.

Prause, G., DeJong, S., McKay, C. and Sonka, M. (1997) Towards a geometrically correct 3-D reconstruction of tortuous coronary arteries based on biplane angiography and intravascular ultrasound. *Int J Card Imaging* **13**, 451-62.

Roelandt, J., Di Mario, C., Pandian, N., Wenguang, L., Keane, D., Slager, C., De Feyter, P. and Serruys, P. (1994) Three-dimensional reconstruction of intracoronary ultrasound images - Rationale, approaches, problems, and directions. *Circulation* **90**, 1044-1055.

Rosenfield, K., Losordo, W., Ramaswamy, K., Pastore, J., Langevin, E., Razvi, S., Kosowsky, B. and Isner, J. (1991) Three-Dimensional reconstruction of human coronary and peripheral arteries from images recorded during two-dimensional intravascular ultrasound examination. *Circulation* **84**, 1938-1956.

Slager, C. J., Laban, M., von Birgelen, C., Krams, R., Oomen, J. A. F., den Boer, A., Li, W., de Feyter, P., Serruys, P. W. and Roelandt, J. (1995) ANGUS: A new approach to three-dimensional reconstruction of geometry and orientation of coronary lumen and plaque by combined use of coronary angiography and IVUS. *JACC* **144A**, 734-6 (Abstr.).

Slager, C., Wentzel, J., Oomen, J., Schuurbiers, J., Krams, R., von Birgelen, C., Tjon, A., Serruys, P. and de Feyter, P. (1997) True reconstruction of vessel geometry from combined X-ray angiographic and intracoronary ultrasound data. *Semin Intervent Cardiol* **2**, 43-47.

von Birgelen, C., de Vrey, E., Mintz, G., Nicosia, A., Bruining, N., Li, W., Slager, C., Roelandt, J., Serruys, P. and de Feyter, P. (1997) ECG-gated three-dimensional intravascular ultrasound: feasibility and reproducibility of the automated analysis of coronary lumen and atherosclerotic plaque dimensions in humans. *Circulation* **96**, 2944-52.

Wahle, A., Wellnhofer, E., Mugaragu, I., Sauer, H., Oswald, H. and Fleck, E. (1995) Assessment of diffuse coronary artery disease by quantitative analysis of coronary morphology based upon 3-D reconstruction from biplane angiograms. *IEEE Transactions on medical imaging* **14**, 230-241.

Wiet, S., Vonesh, M., Waligora, M., Kane, B. and McPherson, D. (1996) The effect of vascular curvature on three-dimensional reconstruction of intravascular ultrasound images. *Ann Biomed Eng* **24**, 695-701.

Yock, P. and Linker, D. (1990) Intravascular ultrasound. Looking below the surface of vascular disease. *Circulation* **81**, 1715-1718.

Evaluation of Endothelial Shear Stress and 3-D Geometry as Factors Determining the Development of Atherosclerosis and Remodeling in Human Coronary Arteries in Vivo

4

Combining 3-D Reconstruction from Angiography and IVUS (ANGUS) with Computational Fluid Dynamics

R Krams, JJ Wentzel, J Oomen, R Vinke, J Schuurbiers, P de Feyter, P Serruys and CJ Slager

Arterioscler Thromb Vasc Biol **17**, *2061-5,1997*

Chapter 4, shear stress and atherosclerosis

The predilection sites of atherosclerotic plaques implicate rheologic factors like shear stress underlying the genesis of atherosclerosis. Presently no technique is available that enables one to provide 3-D shear stress data in human coronary arteries in vivo. In this study, we describe a novel technique that uses a recently developed 3-D reconstruction technique to calculate shear stress on the endothelium with computational fluid dynamics. In addition we calculated local wall thickness, the principal plane of curvature, and the location of plaque with reference to this plane, relating these results to shear stress in a human right coronary artery in vivo. Wall thickness and shear stress values for the entire vessel for three inflow-velocity values (10 cm/s, 20 cm/s, and 30 cm/s equivalents with the Reynolds numbers 114, 229, and 457) were as follows: 0.65±0.37 mm (n=1600) and 19.6±1.7 dyne/cm², 46.1±8.1 dyne/cm² and 80.1±16.8 dyne/cm² (n=1600). Curvature was 25±9 (m^{-1}), resulting in Dean numbers 20±8; 46±16, and 93±33. Selection of data at the inner curvature of the right coronary artery provided wall thickness values of 0.90±0.41 mm (n=100), and shear stress was 17±17, 38±44 and 77±54 dyne/cm² (n=100), whereas wall thickness values at the outer curve were 0.37±0.17 mm and shear stress values were 22±17, 60±44 and 107±79 dyne/cm² (n=100). These findings could be reconciled by an inverse relationship between wall thickness and shear stress for each velocity level under study. For the first time for human vessels in vivo, evidence is presented that low shear stress promotes atherosclerosis. As the method is nondestructive, it allows repeated measurement in the same patient and will provide new insights in the progress of atherosclerosis.

Atherosclerotic plaques are located more frequently near bifurcations, near trifurcations, and in curvatures of vessels compared with other sites of the arterial tree (Fox and Seed, 1981; Sakata and Takebayashi, 1988; Smedby *et al.*, 1995; Tjotta, 1963; Willis, 1954) implying that local factors are necessary to explain this condition fully. In search of these factors, several animal and human post mortem studies have provided evidence for a relationship between local shear stress, imposed by the velocity of the blood on the endothelium, and the localization of these predilection sites of atherosclerosis (Friedman *et al.*, 1987; Friedman *et al.*, 1992; Friedman *et al.*, 1986; Gibson *et al.*, 1993; Sabbah *et al.*, 1984; Sabbah *et al.*, 1986). On a cellular level, other studies have revealed a relationship between shear stress and the production of nitric oxide (NO or endothelium-derived relaxing factor), endotheline-1 and multiple growth factors (Davies and Tripathi, 1993; McIntire, 1992; Zhao *et al.*, 1995).

Despite the abundance of evidence relating shear stress to the normal adaptation of blood vessels and the pathophysiology of atherosclerosis, no 3-D techniques are presently available that enable one to evaluate echographic-derived parameters as plaque size and location in conjunction with shear stress in human coronary arteries in vivo. In an earlier study, we (R.K., J.J.W., J.A.F.O., J.C.H.S., P.J.F., P.W.S., C.J.S.) reported on the possibility of reconstructing human coronary arteries in three dimensions applying a combination of ANGiography and intra vascular UltraSound (ANGUS abstracts:(Laban *et al.*, 1995; Slager *et al.*, 1995a; Slager *et al.*, 1995b)). The present study focuses on the possibility of calculating regional vessel wall thickness and curve in combination with shear stress. Because these data are obtained in human vessels in vivo, this new method enables to evaluate rheologic factors and their relationship to the progression and regression of atherosclerosis and vessel remodeling after interventions.

4.2.1 ANGUS

A detailed description of ANGUS, the 3-D geometric reconstruction method, has been presented elsewhere (Laban *et al.*, 1995; Slager *et al.*, 1995a; Slager *et al.*, 1995b). Briefly, the IVUS catheter (CVIS 2.9F, Sunnyvale, Calif) was visualized with a biplane angiographic system (Siemens, Bicor, Erlangen, Germany). The two views obtained from the X-ray system were digitized, and a custom written algorithm, developed in MATLAB (The Mathworks, Natick, Mass), was used to

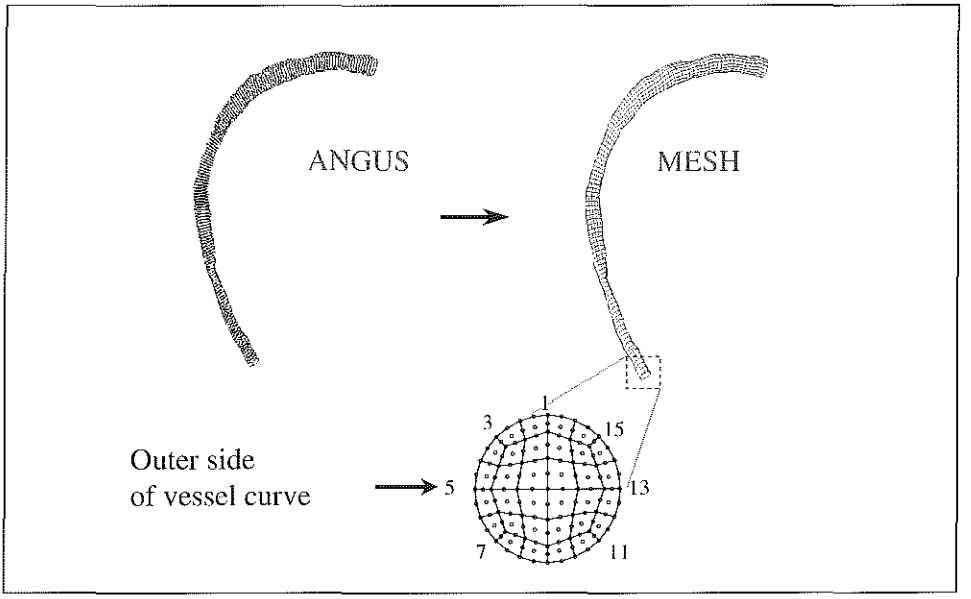

Figure 1: 3-D reconstruction of a right coronary artery from a combination of ANGiography and IVUS (ANGUS) (right panel). Applied luminal mesh for application of computational fluid dynamics (left panel).

reconstruct the catheter path in 3-D space. The echocardiographic vessel cross-sections, obtained from a motorized IVUS pullback at a speed of 0.75 mm/s, were selected offline at end diastole to avoid motion artifacts. These selected frames were digitized and analyzed with a semiautomatic contour-detecting algorithm as described before (Li *et al.*, 1995). Output of the program consisted of lumen contours, signifying the blood-vessel interface, and the media contours, representing the media-adventitia interface (Laban *et al.*, 1995; Li *et al.*, 1995; Slager *et al.*, 1995a; Slager *et al.*, 1995b). These contours were filtered and subsequently positioned perpendicularly onto the 3-D catheter path while the rotational position of the ultrasound transducer was selected on the basis of a comparison of the reconstruction with the coronary angiogram (Laban *et al.*, 1995; Slager *et al.*, 1995a; Slager *et al.*, 1995b).

4.2.2 Mesh definition

The 3-D lumen geometry of the vessel obtained with ANGUS was applied to define a mesh that was subsequently used for the computational fluid dynamics (Figure 1). Generation of the mesh occurred in two steps. First, a straight cylindrical unit tube was created, i.e., a straight tube with a circular cross-section with diameter and length equal to 1 m. In this tube, a mesh was defined consisting of 3-D cells ("bricks"). A single cross-section of the tube consisted of 32 cells; and in the axial direction, the total tube included 100 cross-sections (Figure 1).

Second, based on the 3-D vessel geometry obtained with ANGUS (Laban *et al.*, 1995; Slager *et al.*, 1995a; Slager *et al.*, 1995b) a transformation matrix was generated that was applied to each point of the unit tube to modify the lumen mesh until it resembled the 3-D lumen geometry of the original coronary artery (Figure 1). The resolution for each cell in the mesh was 0.136 mm^2 in the cross-sectional plane (range, 0.216 mm^2 to 0.051 mm^2) and 0.75 mm in the axial direction.

4.2.3 Wall thickness algorithm

The lumen and media contours for each cross-section were used to determine local vessel wall thickness at locations corresponding to the lumen mesh points. With a mesh cross-section consisting of 32 cells, we had 16 cells on the lumen wall interface. With two nodes per cell, this resulted in 32 points on the border of each lumen cross-section of which 16 were used for the present analysis. Hence, with 100 cross-sections, the present analysis resulted in 1600 wall thickness values. Local vessel wall thickness was defined in the cross-sectional plane as the vector, directed from lumen to media, whose intersection with the local lumen and media cross-section was the most perpendicular as possible. In other words, the summed cosine of the intersection angles should be minimal.

4.2.4 Curve

We derived from the 3-D spatially reconstructed vessel geometry a 3-D idealized vessel centerline that passed through the center of the area of each cross-section. Polynomial curve fitting along the vessel centerline was applied to each of the coordinates separately. In general, a fifth order polynomial was necessary to describe the centerline accurately. At the point of intersection of the centerline with each cross sectional mesh plane, the local curvature of the centerline was determined. The radius vector of a circle fitting through three subsequent center line points and pointing from the origin of the circle to the midst of these points was selected for this purpose (Figure 2).

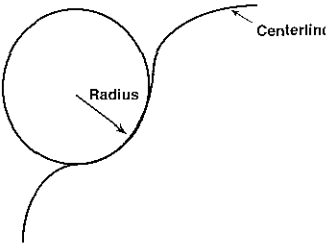

Figure 2: Explanation of the calculation of the curvature of a coronary artery. Displayed are the vessel centerline and the fitted circle for estimation of the local curvature and its direction.

The so-defined local 3-D radius vector was used 1) to calculate curvature (κ=radius^{-1}) and 2) to select wall thickness at the location of the inner and the outer curvature of the vessel. Wall thickness located in the inner curvature was defined as the wall thickness values located closest to the radius vector (Figure 2). The wall thickness located in the outer curvature was located at 180 degrees from the location of the wall thickness of the inner curvature.

A local right-handed coordinate system was set up on the 3-D vessel centerline according to Frenet (Davies and Snider, 1988). The three-unit vectors of this right-handed system are the tangent, the normal, and the binormal vectors (Davies and Snider, 1988). It can be shown that if the direction of the binormal vector (Davies and Snider, 1988) remains unchanged, this 3-D space curve remains in plane. Hence, changes in the direction of this unit vector imply out of plane curvatures ('twist') of the coronary artery.

4.2.5 Computational Fluid Dynamics

Shear stress on the endothelium of a human vessel was calculated using the 3-D mesh described above and consisting of 3-D cells ('bricks'). In each cell, 27 nodes are positioned; and in each node a differential equation describing the full incompressible Navier-Stokes equations are implemented. The non-linear convective term in the Navier-Stokes equations is linearized with a Newton-Raphson approach. To obtain the pressure unknowns from the discrete Navier-Stokes equations, a penalty function approach is used. We have defined the following boundary conditions: uniform stationary inflow velocity of 10 cm/s, 20 cm/s and 30 cm/s at the entrance of the vessel, constant zero stress at the outlet; and no-slip conditions at the vessel wall. The values of 10 cm/s, 20 cm/s and 30 cm/sec were chosen to represent data from patients under baseline conditions. We further assumed that blood was a Newtonian fluid with a density of 1050 kg/m^3 and a viscosity of 3 cP (Krijger *et al.*, 1992; Rindt *et al.*, 1990; Van de Vosse *et al*, 1989). Elimination of the pressure unknowns with the penalty method and linearization of the convective term results in a set of linear equations with velocity unknowns. These equations were solved by a numerical solver, applying a direct profile method of a well-validated (Krijger *et al.*, 1992; Rindt *et al.*, 1990; Van de Vosse *et al*, 1989), commercially available finite element package (Sepran, Sepra , Leiden, The Netherlands), which was implemented on a workstation (HP 715/80, 256 Mbyte RAM). Details and elaborate validation of the solver have been presented before by different laboratories under different conditions (Krijger *et al.*, 1992; Rindt and Steenhoven, 1996; Rindt *et al.*, 1990; Van de Vosse *et al*, 1989).

The present approach resulted in the calculation of the full 3-D velocity, pressure and velocity gradient fields. Because a quadratic interpolation scheme was used, the calculations resulted in approximately 25 000 nodal points in which the full 3-D solution of the vector fields were evaluated. From these points, we selected for each cross-section the 16-velocity gradient values located near the vessel wall. These numbers were subsequently multiplied with viscosity to obtain

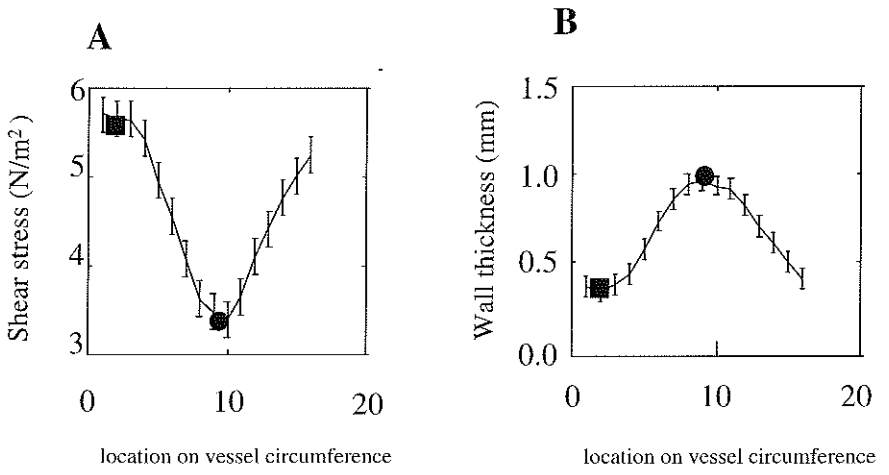

Figure 3: Shear stress values for a velocity of 20 cm/s (panel A) and vessel wall thickness (panel B) versus the location on the circumference after axial averaging. Each point is the average of 100 data points. Error bars represent standard deviations. The additional points in the figures signify the location of the inner curve (•) and the outer curve (■).

shear stress at 16 points for each cross-section. For the entire vessel, with 100 cross-sections, this resulted in 1600 values of shear stress.

At corresponding locations on the vessel wall, we calculated shear stress, wall thickness and curvature with the algorithms described above. The spatial resolution of the shear stress values was approximately 0.3 mm in the circumferential direction and 0.75 mm in the axial direction.

The data are presented as mean ± standard deviation. Differences in mean values are tested by a Student's t-test, significance levels are set to $p<0.05$. To relate wall thickness quantitatively to shear stress we applied simple linear regression analysis, applying a standard software package (SPSS, Maryland, USA). Quality of the fit was evaluated with ANOVA and r^2 values.

The 3-D reconstruction of the lumen contours of a human right coronary artery by the ANGUS method is shown in the left panel of Figure 1, while the right panel displays the surface of the mesh necessary for the 3-D-velocity calculations. The gradient of the velocity profiles i.e. the shear rate was used for calculations of shear stress.

Average diameter and wall (intima+media) thickness for the entire vessel was: 2.3±0.4 mm and 0.65±0.37 mm (n=1600). The average maximal and minimal wall thickness per cross section were 1.2 ± 0.36 mm (n=100) and 0.26± 0.08 mm (n=100,p<0.05), respectively. The radius (R) of curvature of the reconstructed vessel was 40±21 mm, resulting in a curvature (1/R) of 25.09±8.96 (m^{-1}) and a curvature ratio of approximately 1 to 17. Local twist of the catheter path was calculated from the rotation of the binormal, as defined by Frenet (Davies and Snider, 1988). The rotation per step of 0.75 mm along the vessel centerline was 0.1734±0.147°. Cumulative rotation was approximately 13°.

Based on the curve calculations, we calculated average vessel wall thickness located at the inner and outer location of the curve as 0.90±0.41 mm (n=100) and 0.37±0.17 mm (n=100, p<0.05), respectively. The location of the largest wall thickness value was close to the location of the inner curve and the smallest wall thickness was close to the outer curve (Figure 3A).

Shear stress values were calculated for three inflow velocities (10 cm/s, 20 cm/s and 30 cm/s), which are reported in this order. Averaged values of Reynolds number, per cross-section, for these inflow velocities were 114±22, 229±44 and

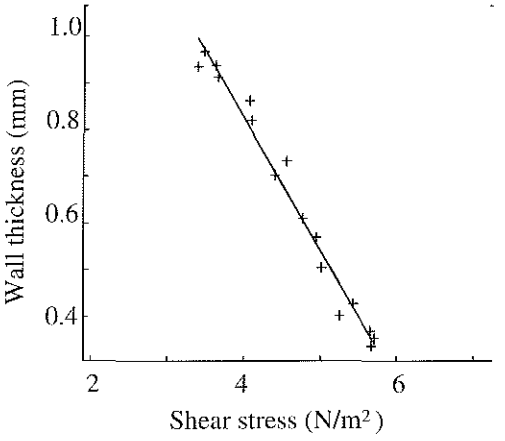

Figure 4: Relationship between shear stress and echographic-derived vessel wall thickness after averaging in the axial direction of a human right coronary artery. Inflow velocity : 20 cm/s.

Table 1: Slope (α) and intercept (β) of the regression equation relating wall thickness to shear stress for a human right coronary artery.

	α mm/N/m^2	β mm	R^2	P
V_{10}	-1.28	3.18	0.88	<0.05
V_{20}	-0.30	2.00	0.98	<0.05
V_{30}	-0.10	2.00	0.96	<0.05

Applied regression equation: Wth=α.SS+β, with Wall Thickness (Wth) in mm and shear stress (SS) in N/m^2. V_{10}, V_{20} and V_{30} refer to conditions in which coronary inflow velocity equaled 10 cm/s, 20 cm/s and 30 cm/s.

457±87 (n=100); the values of Dean number were 20±8, 46±16 and 93±33 (n=100). Average shear stress for the entire right coronary artery were 20±2, 46±8 and 80±17 dyne/cm^2 (n=1600). When the shear stress values were selected on basis of the location of the inner and outer curvature, these values were: 17±17, 38±44 and 77±54 dyne/cm^2 (n=100) and 22±17, 60±44 and 107±79 dyne/cm^2, respectively (n=100, p<0.05). The location of maximal shear stress was closer to the outer wall, the minimal shear stress was closer to the inner curve (Figure 3B).

To evaluate the contribution of shear stress to the asymmetrical distribution of plaque in this right coronary artery, we averaged the wall thickness and shear stress values over the axial direction of the vessel (n=100). Shear stress and wall thickness appeared out of phase when plotted against the location of the circumference, i.e., a low shear stress corresponded to a high wall thickness at the same location (Figure 4). The resulting relationship between shear stress and wall thickness was inverse and could be described as linear for all three relationships (Table 1 and Figure 4).

Atherosclerosis is located nonuniformly over the arterial vascular system (Fox and Seed, 1981; Sakata and Takebayashi, 1988; Smedby *et al.*, 1995; Tjotta, 1963; Willis, 1954). These predilection sites of atherosclerosis as well as the eccentric localization of most advanced forms of atherosclerosis may be explained on the basis of hemodynamic factors (Fox and Seed, 1981; Friedman *et al.*, 1987; Friedman *et al.*, 1992; Friedman *et al.*, 1986; Gibson *et al.*, 1993; McIntire, 1992; Sabbah *et al.*, 1984; Sabbah *et al.*, 1986; Sakata and Takebayashi, 1988; Smedby *et al.*, 1995; Tjotta, 1963; Willis, 1954). The most elaborate, studied factor associated with atherosclerosis is the shear stress, imposed by streaming of the blood along the endothelium (Friedman *et al.*, 1987; Friedman *et al.*, 1992; Friedman *et al.*, 1986; Gibson *et al.*, 1993; McIntire, 1992; Sabbah *et al.*, 1984; Sabbah *et al.*, 1986). The exact implications of changes in shear stress are not yet known as different disturbances of the laminar velocity pattern have

been associated with the degree and localization of atherosclerosis: low shear stress (Friedman *et al.*, 1987; Friedman *et al.*, 1992; Gibson *et al.*, 1993); low and oscillating shear stress (Moore *et al.*, 1992) and high shear stress (Krijger *et al.*, 1992).

The discrepancies between shear stress and degree and/or localization of atherosclerosis might be related to collection of the data (Friedman *et al.*, 1987; Friedman *et al.*, 1992; Gibson *et al.*, 1993). For instance, some studies related an average geometric model of the carotid artery to average histological parameters of the vessel wall (Moore *et al.*, 1992; Sakata and Takebayashi, 1988). This averaging process might underestimate related phenomena as has been pointed out recently (Friedman *et al.*, 1987; Friedman *et al.*, 1992; Gibson *et al.*, 1993). To overcome this problem Friedman *et al.* and Gibson *et al.* devised flow through casts in which the related locally derived shear rates with locally derived vessel wall thickness from postmortem material of humans (Friedman *et al.*, 1987; Friedman *et al.*, 1992; Gibson *et al.*, 1993). Although this approach improved the relationship between shear stress and intimal thickness of each specimen, this method is very time consuming, allows the collection of only a relative small amount of data per specimen, and applies to post mortem material only. The latter constraint is especially important as it does not allow one to evaluate the effect of shear stress on different time points in a single human vessel. With the present technique, it is possible to evaluate the hemodynamic effect induced by interventions on restenosis and atherosclerosis without the complicating factor of a measurement device located inside the vessel disturbing the flow pattern.

Despite the fact that numerical techniques do not include the disadvantages of the hydraulic methods, so far only 2-D geometries and recently idealized 3-D-geometries of vessels have been studied with this technique (Krijger *et al.*, 1992; Van de Vosse *et al*, 1989). As we studied these idealized geometries, it became clear that for local shear stress calculations, the local geometry is very important. This parameter becomes even more important when local irregularities of a sick vessel induces local vertices, stagnation points, and separation of stream lines ('secondary velocity fields'). Furthermore, since the coronary vessel anatomy and geometry are not confined to a single 2D-plane, it is necessary for the secondary velocity fields to be analyzed with 3-D techniques as symmetry conditions are no longer applicable under these conditions (Krijger *et al.*, 1992; Van de Vosse *et al*, 1989). In addition, although idealized geometries are useful in our understanding the relation of hemodynamics to atherosclerosis, coupling of the numerical techniques to realistic 3-D vessel geometries appears to be a necessary condition for understanding induction, progression and regression of atherosclerosis in humans in vivo.

Method limitations

In this study, a numerical approach has been introduced to calculate shear stress on the vessel wall. Such methods do not have the constraints of the hydraulic in-vitro set ups described above; however they rely on the grid spacing and accuracy of the vessel geometry obtained. Accuracy of the reproduction of the 3-D geometry has been reported on recently (Laban *et al.*, 1995; Slager *et al.*, 1995a; Slager *et al.*, 1995b) and is in the order of 0.1 mm, which is accurate enough for the present approach (Krijger *et al.*, 1992; Rindt and Steenhoven, 1996; Rindt *et al.*, 1990; Van de Vosse *et al*, 1989). Accuracy of the numerical technique, related to the interpolation scheme, iterative solver used, and dimensions of the individual cells, have been compared with laser Doppler techniques; and it was shown that the method produced accurate results in 90° curved tubes' carotid bifurcations and models of the basilar artery (Krijger *et al.*, 1992; Rindt and Steenhoven, 1996; Rindt *et al.*, 1990; Van de Vosse *et al*, 1989).

We analyzed only stationary 3-D velocity fields in the present study. It has been shown that oscillating, low shear stress also may contribute to the development of atherosclerosis (Moore *et al.*, 1992). With the present analysis, we cannot exclude that shear stress oscillation could also be involved.

We assumed that the coronary vessel wall is rigid. However, the coronary vessel wall is elastic and its radius changes by 5% to 10% over the cardiac cycle. When the effect of elasticity was included in a numerical analysis of the human carotid artery, it appeared that the effect of elasticity on shear stress is mainly periodic and does not affect the time-averaged shear stress (Kuban and Friedman, 1995; Moore *et al.*, 1992; Perktold and Rappitsch, 1995). Hence, if this situation is applicable for the coronary artery, it could imply that time-averaged shear stress values are less affected by movement of the vessel wall. This may explain why a high correlation between spatially averaged shear stress and atherosclerosis was still found in the present study, despite the simplifications used.

We used uniform inflow velocity as one of the boundary conditions. As a result, the first few values of shear stress might be artificially high. However, a reanalysis of the relationship between shear stress and wall thickness omitting the first 10 points revealed a similar relationship, making this effect of minor importance.

As a first application we studied a human right coronary artery with known atherosclerosis. This patient was send to our hospital for anginal complaints and consequently, a percutaneous transluminal coronary angioplasty (PTCA) was performed to relieve these symptoms. The 3-D-reconstruction presented in this study was performed after the PTCA. To evaluate the effect of PTCA on our findings, we also evaluated the relationship between wall thickness and shear stress for the segment of vessel upstream of the known location of the PTCA. The results still revealed a significant inverse relationship between wall thickness and shear stress.

Because of its nondestructive nature, the present method allows multiple measurements in the same patient. However, because coronary arteries are difficult to image noninvasively, we still need an invasive method when atherosclerosis and shear stress are evaluated in coronary arteries in humans in vivo.

This is the first study presenting a technique, that makes it possible to evaluate the relationship of 3-D coronary vessel geometry to shear stress in humans in vivo. With this technique, we were able to show that: 1) wall thickness is thicker on the inner curve than on the outer wall in a right coronary artery in vivo, 2) the shear stress is low on the inner wall and high on the outer wall and 3) wall thickness is inversely related to shear stress. The present method enables one to evaluate the role of shear stress during the development of restenosis after coronary interventions or plaque progression/regression, as it allows multiple measurements in the same patient.

We gratefully acknowledge funding (to J.J.W.) by the Inter University cardiology Institute of the Netherlands (project ICIN18) and the gift of the transformation matrix by Dr. F. van de Vosse.

Davies, H. F. and Snider, A. D. (1988) Introduction to vector analysis. C. Brown, Dubuque, Iowa.

Davies, P. F. and Tripathi, S. C. (1993) Mechanical stress mechanisms and the cell. An endothelial paradigm. *Circ Res* **72**, 239-45.

Fox, B. and Seed, W. A. (1981) Location of early atheroma in the human coronary arteries. *J Biomech Eng* **103**, 208-12.

Friedman, M. H., Bargeron, C. B., Deters, O. J., Hutchins, G. M. and Mark, F. F. (1987) Correlation between wall shear and intimal thickness at a coronary artery branch. *Atherosclerosis* **68**, 27-33.

Friedman, M. H., Bargeron, C. B., Duncan, D. D., Hutchins, G. M. and Mark, F. F. (1992) Effects of arterial compliance and non-Newtonian rheology on correlations between intimal thickness and wall shear. *J Biomech Eng* **114**, 317-20.

Friedman, M. H., Deters, O. J., Bargeron, C. B., Hutchins, G. M. and Mark, F. F. (1986) Shear-dependent thickening of the human arterial intima. *Atherosclerosis* **60**, 161-71.

Gibson, C. M., Diaz, L., Kandarpa, K., Sacks, F. M., Pasternak, R. C., Sandor, T., Feldman, C. and Stone, P. H. (1993) Relation of vessel wall shear stress to atherosclerosis progression in human coronary arteries. *Arterioscler Thromb* **13**, 310-5.

Krijger, J. K., Heethaar, R. M., Hillen, B., Hoogstraten, H. W. and Ravensbergen, J. (1992) Computation of steady three-dimensional flow in a model of the basilar artery. *J Biomech* **25**, 1451-65.

Kuban, B. D. and Friedman, M. H. (1995) The effect of pulsatile frequency on wall shear in a compliant cast of a human bifurcation. *J. Biomech. Eng.* **117**, 219-225.

Laban, M., Oomen, J. A. F., Slager, C. J., Wentzel, J. J., Krams, R., Schuurbiers, J. C. H., Den Boer, A., Von Birgelen, C., Serruys, P. W. and De Feyter, P. J. (1995) Angus: A new approach to three-dimensional reconstruction of coronary vessels by combined use of angiography and intravascular ultrasound and IVUS. In *Computers in Cardiology*, 325-328, Piscataway.

Li, W., Bom, N. and Van Egmond, F. C. (1995) Three-dimensional quantification of intravascular ultrasound images. *J Vasc Invest* **1**, 57-61.

McIntire, L. V. (1992) Bioengeneering and vascular biology; Alza distinguished lecture. *Ann Biomed Eng* **22**, 2-13.

Moore, J. E., Jr., Ku, D. N., Zarins, C. K. and Glagov, S. (1992) Pulsatile flow visualization in the abdominal aorta under differing physiologic conditions: implications for increased susceptibility to atherosclerosis [published erratum appears in J Biomech Eng 1993 Feb;115(1):12]. *J Biomech Eng* **114**, 391-7.

Perktold, K. and Rappitsch, G. (1995) Computer simulation of local blood flow and vessel mechanics in a compliant carotid artery bifurcation. *J. Biomechanics* **28**, 845-856.

Rindt, C. C. M. and Steenhoven, A. A. (1996) Unsteady flow in a rigid 3-D model of the carotid artery bifurcation. *Transaction of the ASME* **118**, 90-96.

Rindt, C. C. M., Steenhoven, A. A., Janssen, J. D., Reneman, R. S. and Segal, A. (1990) A numerical analysis of steady flow in a three dimensional model of the carotid artery bifurcation. *J. Biomechanics* **23**, 461-473.

Sabbah, H. N., Khaja, F., Brymer, J. F., Hawkins, E. T. and Stein, P. D. (1984) Blood velocity in the right coronary artery: relation to the distribution of atherosclerotic lesions. *Am J Cardiol* **53**, 1008-12.

Sabbah, H. N., Khaja, F., Hawkins, E. T., Brymer, J. F., McFarland, T. M., van der Bel-Kahn, J., Doerger, P. T. and Stein, P. D. (1986) Relation of atherosclerosis to arterial wall shear in the left anterior descending coronary artery of man. *Am Heart J* **112**, 453-8.

Sakata, N. and Takebayashi, S. (1988) Localization of atherosclerotic lesions in the curving sites of human internal carotid arteries. *Biorheology* **25**,567-78.

Slager, C. J., Laban, M., Oomen, J. A. F., Von Birgelen, C., Li, W., Krams, R., Schuurbiers, J. C. H., Den Boer, A., Serruys, P. W., Roelandt, J. R. T. C. and De Feyter, P. J. (1995a) Three-dimensional geometry and orientation of coronary lumen and plaque. Reconstruction from angiography and ICUS (ANGUS). *Thoraxcenter J* **7/3**, 36-37.

Slager, C. J., Laban, M., Von Birgelen, C., Krams, R., Oomen, J. A. F., Den Boer, A., Li, W., De Feyter, P. J., Serruys, P. W. and Roelandt, J. R. T. C. (1995b) Angus: A new approach to three-dimensional reconstruction of geometry and orientation of coronary lumen and plaque by combined use of coronary angiography and IVUS. *J Am Coll Cardiol* **25**, 144a.

Smedby, O., Johansson, J., Molgaard, J., Olsson, A. G., Walldius, G. and Erikson, U. (1995) Predilection of atherosclerosis for the inner curvature in the femoral artery. A digitized angiography study. *Arterioscler Thromb Vasc Biol* **15**, 912-7.

Tjotta, E. (1963) The distribution of atheromatosis in the coronary arteries. *J Atheroscler Res* **3**, 253-261.

Van de Vosse, F. N., van Steenhoven, A. A., Segal, A, Janssen, J. D. (1989) A finite element analysis of the steady laminar entrance flow in a 90 curved tube. *Int . J. Num. Methods in Fluids* **9**, 275-287.

Willis, C. G. (1954) Localizing factors in atherosclerosis.*Can Med Assoc J* **70**,1-9.

Zhao, S., Suciu, A., Ziegler, T., Moore, J. E., Jr., Burki, E., Meister, J. J. and Brunner, H. R. (1995) Synergistic effects of fluid shear stress and cyclic circumferential stretch on vascular endothelial cell morphology and cytoskeleton. *Arterioscler Thromb Vasc Biol* **15**, 1781-6.

Changes of 3-D Arterial Geometry and 3-D Shear Stress Distribution induced by Coronary Stent Implantation

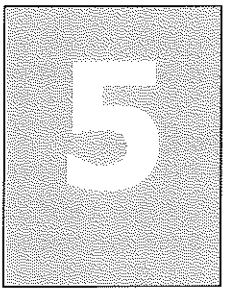

JJ Wentzel, DM Whelan, WJ van der Giessen, HMM van Beusekom, I Andhyiswara, PW Serruys, CJ Slager and R Krams

Journal of Biomechanics, in press

Chapter 5, stent and 3-D geometry

Mechanisms of in-stent restenosis are not fully understood. Shear stress is known to play a role in plaque and thrombus formation and is sensitive to changes in regional vessel geometry. Hence, we evaluated the regional changes in 3-D geometry and shear stress induced by stent placement in coronary arteries of pigs.

Methods

3-D reconstruction was performed, applying a combined angiographic and IVUS technique (ANGUS), from 7 Wallstents (diameter 3.5 (n=3) and 5 mm (n=4)), which were implanted in 7 coronary arteries of 5 pigs. This 3-D geometry was used to calculate locally the curvature, while the shear stress distribution was obtained by computational fluid dynamics. Local changes in shear stress were obtained at the entrance and exit of the stent for baseline (0.65 ±0.22 ml/s) and hyperemic flow (2.60±0.86 ml/s) conditions.

Results

After stent implantation, the curvature increased by 121% at the entrance and by 100% at the exit of the stent, resulting in local changes in shear stress. In general, at the entrance of the stent local maxima in shear stress were generated, while at the exit both local maxima and minima in shear stress were observed ($p<0.05$). Additionally, the shear stress at the entrance and exit of the stent were correlated with the local curvature (r: 0.30 to 0.84).

Conclusion

Stent implantation changes 3-D vessel geometry in such a way that regions with decreased and increased shear stress occur at the stent edges. These changes might be related to the asymmetric patterns of in-stent restenosis.

Interventional techniques, like balloon angioplasty, have shown to relieve hemodynamic relevant arterial stenosis caused by atherosclerosis. However, in 30-50% of the treated cases restenosis develops, which is for 60-70% caused by arterial shrinkage ('arterial remodeling') and for 30-40% by neointimal hyperplasia (Mintz *et al.*, 1996). While stent implantation prevents arterial remodeling the rate of restenosis is still 20-35%, largely due to neointimal formation (Fischman *et al.*, 1994; Serruys *et al.*, 1994).

Despite the importance of the problem, an appropriate therapy is still lacking (Leon *et al.*, 1996). A reason might be that shear stress has not been recognized as factor in explaining in-stent restenosis yet. Arguments in favor of shear stress is that it is known to be involved in a variety of processes related to cellular growth and thrombosis, probably through the activation of several genes. (Malek and Izumo, 1995; Nikol *et al.*, 1996; Strony *et al.*, 1993). In addition, shear stress has been shown to be changed regionally after stent placement and might therefore explain the fact that in-stent restenosis is not distributed homogeneously in stents (Fontaine *et al.*, 1994; Peacock *et al.*, 1995).

The aim of the present study is to evaluate regional changes in 3-D geometry and shear stress distribution after stent placement in curved coronary arteries, applying a new technique that enabled us to reconstruct coronary arteries in three dimensions (3-D) ('ANGUS',(Slager *et al.*, 1997)) and to calculate regional shear stress in vivo.

5.2.1 Animal preparation and instrumentation

All the experiments were performed under the regulations of the animal care committee of the Erasmus University Rotterdam and in accordance with the "Guide for the Care and Use of Laboratory Animals" (NIH publication 85-23, revised 1985). After an overnight fast, 5 Yorkshire pigs (weight 29.5-34 kg) were sedated with 20 $mg.kg^{-1}$ ketamine hydrochloride. Instrumentation of the animals was performed as described before (van der Giessen *et al.*, 1991). Anesthesia was induced by thiopental 11 mg/kg (and maintained with 1-4 vol% isoflurane). Ventilation was performed by a mixture of oxygen and nitrous oxide (1:2 vol/vol). A 9F sheath was introduced in the left carotid artery for catheter placement. All animals received intra arterial administration of 10,000 IU heparin and 250 mg acetylsalicylic acid. Biplane coronary angiography (Siemens Bicor, Erlangen, Germany) was performed using Omnipaque (Nycomed Ireland Ltd., Cork, Ireland) as a contrast agent.

5.2.2 Protocol

After intra-coronary administration of 1 mg isosorbide dinitrate, quantitative angiography (CAAS; Pie Medical, Maastricht, The Netherlands) was performed to select a curved coronary arterial segment with a diameter between 3 to 5 mm for stent implantation. In 5 animals a total of 7 locations were selected, distributed over the right coronary artery (RCA, n=4) the left anterior descending artery (LAD, n=2) and the left circumflex (LCX, n=1).

Subsequently, a sheathed IVUS catheter (2.9F MicroView, CVIS, Sunnyvale CA, USA) was introduced crossing the selected segment and an ECG triggered stepwise (0.5 mm) IVUS pullback was performed (Bruining *et al.*, 1995). In order to enable a 3-D reconstruction of the coronary artery, biplane angiograms with the IVUS catheter in place were made just after the start of the pullback (Slager *et al.*, 1997).

Thereafter, Wallstents (diameter 3.5 (n=3) and 5 mm (n=4), Schneider, Europe AG, Switzerland) were implanted at the selected position. After stent placement, IVUS imaging procedure plus biplane coronary angiography was repeated. 3-D calibration of the biplane X-ray system was performed by isocentric placement of a calibration cube having 5 cm long edges.

5.2.3 3-D reconstruction of coronary arteries

3-D reconstruction of the coronary arteries was performed applying a combination of ANGiography and intravascular UltraSound (ANGUS) (Slager *et al.*, 1995), described in detail elsewhere (Laban *et al.*, 1995; Chapter 3). Briefly, the IVUS catheter position was recorded in biplane. Using the calibration cube images, mathematical transformation matrices were generated, that allowed 3-D reconstruction of the catheter path from the 2-D catheter projections (Laban *et al.*, 1995; McKay *et al.*, 1982). The IVUS images obtained at the R-top of the ECG were selected for further analysis. Lumen contours were traced semi-automatically by a validated software package (Li, 1997). These contours were positioned perpendicularly to the reconstructed catheter path and the correct angular rotation of the IVUS contours was determined as described before (Slager *et al.*, 1997). In some arteries additional filtering was applied to remove small respiration artifacts.

5.2.4 Computational fluid dynamics

Mesh definition

The lumen of the reconstructed arteries was filled with a 3-D mesh consisting of 32 elements in each cross-section, each element containing 27 nodes. The axial resolution was chosen such that before and after stent implantation the resolution was the same. As a maximum of 100 cross sections could be applied and the

Table 1: Flow and mean entrance velocities applied for the computational fluid dynamics

	Vessel	flow I *(ml/s)*	flow II *(ml/s)*	Mean velocity I *(m/s)*		Mean velocity II *(m/s)*	
				pre	post	pre	post
Pig 181	RCA	0.52	2.08	0.045	0.017	0.178	0.067
Pig 186	RCA	0.48	1.92	0.061	0.046	0.245	0.182
Pig 187	RCA	0.46	1.84	0.055	0.055	0.207	0.220
Pig 189	LAD	0.88	3.52	0.039	0.028	0.158	0.112
Pig 188 a	RCA	0.51	2.04	0.065	0.042	0.260	0.168
Pig 188 b	LAD	1.00	4.00	0.071	0.070	0.284	0.278
Pig 188 c	LCX	0.71	2.83	0.096	0.030	0.384	0.121

pre: before stent implantation; post : after stent implantation; RCA: right coronary artery; LAD: left anterior descending artery; LCX: left circumflex.

stented segments were of variable length, a axial mesh resolution ranging from 0.43 mm to 0.74 mm was utilized.

Boundary conditions and Assumptions

The incompressible 3-D Navier Stokes equations were implemented in each node of the mesh. We assumed that blood behaves as a Newtonian fluid with a viscosity of $3*10^{-3}$ Pa.s and with a density of 1050 kg/m^3. The basal flow through the coronaries was derived from the flow per 100 gr heart weight (133 ml/min/100gr) (Sassen *et al.*, 1989), thereby assuming that the ventricular weight is a constant fraction of the total body weight (White and Bloor, 1981) and using the reported flow distribution over the LAD (45%), the RCA (24%) and the LCX (32%) (White and Bloor, 1981). A parabolic inflow profile was implemented. As the entrance diameter of each artery was different, mean entrance velocity varied (Table 1). In addition to baseline, hyperemic flow conditions (4 times baseline) were applied (Table 1).

The other boundary conditions were: zero stress in the normal and tangential direction at the exit of the blood vessel and no slip at the vessel wall. The resulting matrices were solved with a validated finite element package (Sepran, Sepra, Leiden, the Netherlands) (van de Vosse *et al.*, 1989).

5.2.5 Analysis

Matching coronary arteries in three-dimensional space before and after stent implantation

Side branches and veins were selected as landmarks to match the overlapping regions of 3-D reconstructions before and after stent implantation. The location of the stent was projected on the artery before stent placement to calculate parameters with reference to the stent location. Description of the geometrical and shear stress findings was focused onto the stent entrance and stent exit, as defined

Table 2: Specification of regions near the entrance and exit of the stent

	entrance		*exit*	
	S_{max} *region (mm)*	S_{min} *region (mm)*	S_{min} *region (mm)*	S_{max} *region (mm)*
Inner curve	-5 to 2	0 to 5	0 to 5	-5 to 2
Outer curve	0 to 5	-5 to 2	-5 to 2	0 to 5

Distances (mm) with respect to the stent edges (0 mm) in which a minimum or maximum in shear stress in the inner or outer curve is determined. Positive direction is from proximal to distal ; S_{min} ,S_{max}: regional minimum or maximum of shear stress.

in Table 2. For this purpose, data of the individual animals were averaged using these locations as a landmark.

Definition of geometrical and hemodynamic parameters

The following parameters based on either the 3-D vessel geometry or 3-D velocity calculations were defined to describe the factors as presented below . All parameters were calculated with self-developed software (Matlab®, Mathworks Inc.,Mass, USA).

Geometrical parameters

The average diameter (D) of each lumen cross section was calculated from the area (A_l) according to: $D=2*\sqrt{(A_l/\pi)}$. The local curvature (C), was obtained from the centerline passing through the center of mass of successive IVUS cross sections, after filtering by a cubic smoothing spline. The maximal curvature (C_{max}) and its location in the region near the entrance and exit of the stent were determined. The location of the inner and outer curve was derived from a plane fitted through all points of the 3-D centerline. The vector through the center of mass and parallel to the fitted plane indicates the inner and outer curve.

Hemodynamic parameters

Local Reynolds numbers (Re), were derived from the cross sectional diameter (D), the mean velocity (v) at that cross section, the density (ρ) and the viscosity (η). ($Re=\rho$ .v. D/η).

Local dean numbers (De), were calculated from the product of the local Reynolds number and the square root of the local radius to curvature ratio: $De=Re*\sqrt{(D/2*C)}$.

Shear stress at the vessel wall was calculated from the product of the local velocity gradient and viscosity. After filtering, minimum (S_{min}) and maximum (S_{max}) shear stress values at the inner and outer curve were determined in the region (Table 2) near the entrance and exit of the stent. Subsequently, at similar locations shear stress values before stent placement were determined. The shear

stress values were normalized for variations in local vessel diameter by dividing the regional shear stress (S_{reg}) by the regional Poisseuille derived shear stress (S_{pois}) ($S_n = S_{reg}/S_{pois}$). As a consequence, this normalized shear stress S_n will have a value 1 for straight sections of the vessel, irrespective of the local diameter. The extreme values of S_n were correlated to the curvature at C_{max}.

All values are expressed as mean ± SD. SPSS 7.5 (SPSS Inc. Chicago, Illinois, USA) was used for all statistical calculations. Data before and after stent implantation were compared by paired Student's t-test. The normalized shear stress values were related to curvature applying regression analysis. Both first order and second order polynomial equations were applied, but only if both the F-test and the coefficient of the second order term were significant, the second order polynomial equation was reported. For all statistical analysis, $p<0.05$ was considered significant.

5.4.1 Geometrical parameters

Diameter and curvature

The 3-D geometry of a coronary artery before and after stent implantation is exemplified in Figure 1. The average (IVUS) diameter derived from the 3-D geometry of the stented vessel segment decreased by 9±5% from 3.2±0.6 mm to 2.9±0.6 mm ($p<0.05$) after stent placement. In addition, Wallstent implantation increased the average curvature derived from the 3-D geometry near the entrance by 121% (from 50.0±26.0 to 110.4±39.6, $p<0.05$, Figure 2) and near the exit of the stent by 100% (from 53.2±27.2 to 106.2±46.8, $p<0.05$, Figure 2). (Note: values C_{max} in the text are derived from local extremes and differ slightly from Figure 2).

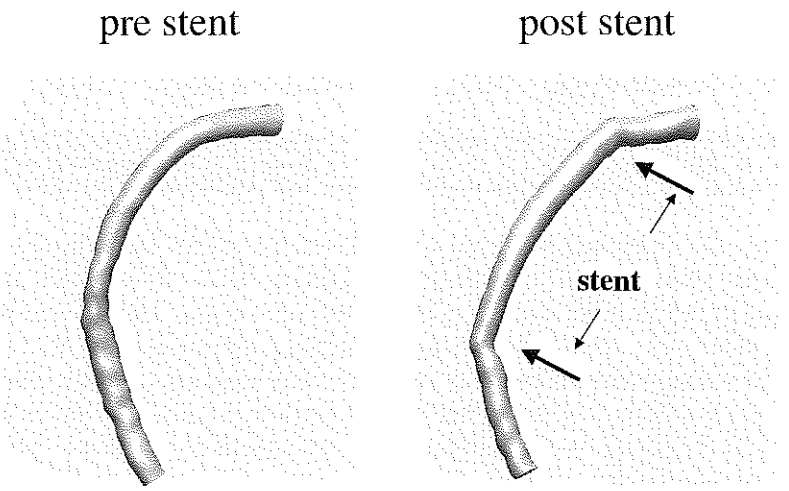

Figure 1: 3-D reconstruction of a right coronary artery of a pig before (pre) and after (post) stent implantation.

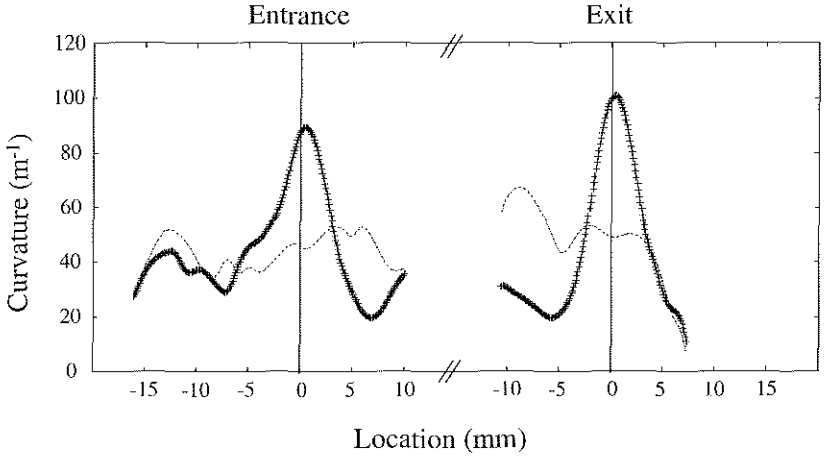

Figure 2: Average curvature of the arteries relative to the location of the entrance (0 mm) and exit of the stent (0 mm) before (-.-) and after after (+) stent implantation.

5.4.2 Hemodynamic parameters

Reynolds number and Dean number

The local Reynolds number, determined at the location of C_{max}, before stent implantation was 91±33 and 365±131 for low and high flow conditions, respectively. After stent placement the local Reynolds numbers remained constant (93±30 and 374±119). In contrast, the Dean numbers increased after stent implantation from 25.1±9.1 to 35.6±7.3 ($p<0.05$). Similar changes in Dean numbers were observed for the hyperemic flow conditions, but at a 4 time higher level ($p<0.05$).

Shear stress at the inner curve

At the entrance of the stent, the maximal shear stress (S_{max}) increased after stent placement by 74% and 113% for low and high flow conditions respectively (Table 3). At the exit of the stent S_{max} increased by 30% ($p<0.05$) for low flow conditions, while S_{min} tended to decrease by 54% ($0.05<p<0.065$) for high flow conditions.

Similarly, changes in normalized shear stress at the entrance and exit of the stent were observed (Figure 3). The maximal shear stress increased significantly at both the entrance and exit of the stent, while minimum shear stress decreased only at the exit of the stent (Table 3 and Figure 4).

Shear stress at the outer curve

At the entrance of the stent for high flow conditions, stent implantation increased S_{max} by 79% (Table 3). Normalized maximal shear stress increased both at the entrance and exit of the stent, while minimal shear stress remained unchanged (Table 3 and Figure 3b, Figure 4).

(Note: values Sn_{max} and Sn_{min} in Table 3 are derived from local extremes and differ slightly from Figure 3).

Relation normalized shear stress and curvature

Inner curve The normalized shear stress was not related to the curvature except for the Sn_{max} at the entrance (high flow condition) and at the exit of the stent (low flow condition) (entrance: $Sn_{max}=0.93+0.0088*C_{max}$, $r^2=0.33$ $p<0.05$; exit: Sn_{max} :$1.20-0.005*C_{max}+3.5*10^{-5}*C_{max}^2$, $p<0.05$, $r^2=0.53$).

Outer curve For low flow conditions only the Sn_{min} and the Sn_{max} at the exit of the stent were related to the curvature ($Sn_{min}=0.71+0.0134*C_{max}-9*10^{-5}*C_{max}^2$, $r^2=0.54$, $p<0.05$; $Sn_{max}=1.07+0.0055*C_{max}$ $r^2=0.62$, $p<0.05$).

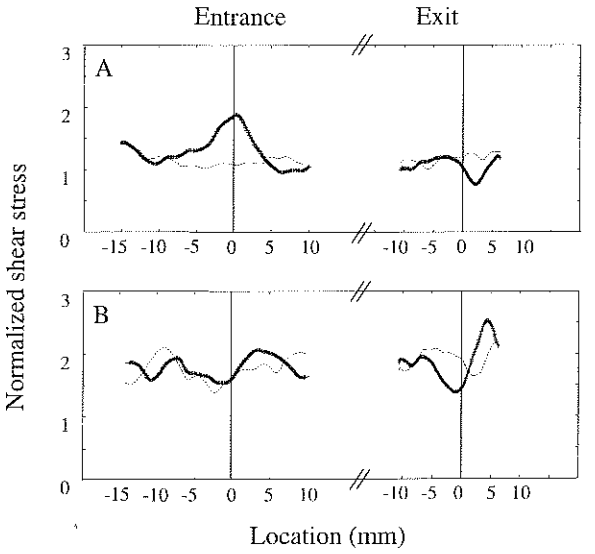

Figure 3: Average normalized shear stress relative to the location of the entrance (0 mm) and exit of the stent (0 mm) before (-.-) and after (+) stent implantation at hyperemic flow conditions a) in the inner curve b) in the outer curve. Location sign: distal is positive.

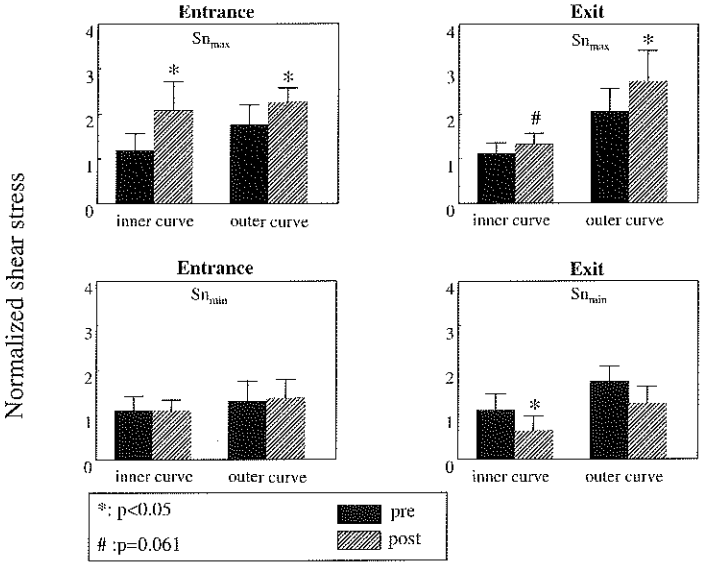

Figure 4: Average normalized maximal (minimal) shear stress (Sn_{max}, Sn_{min}) in the inner and outer curve at the entrance and exit of the stent for high flow conditions.

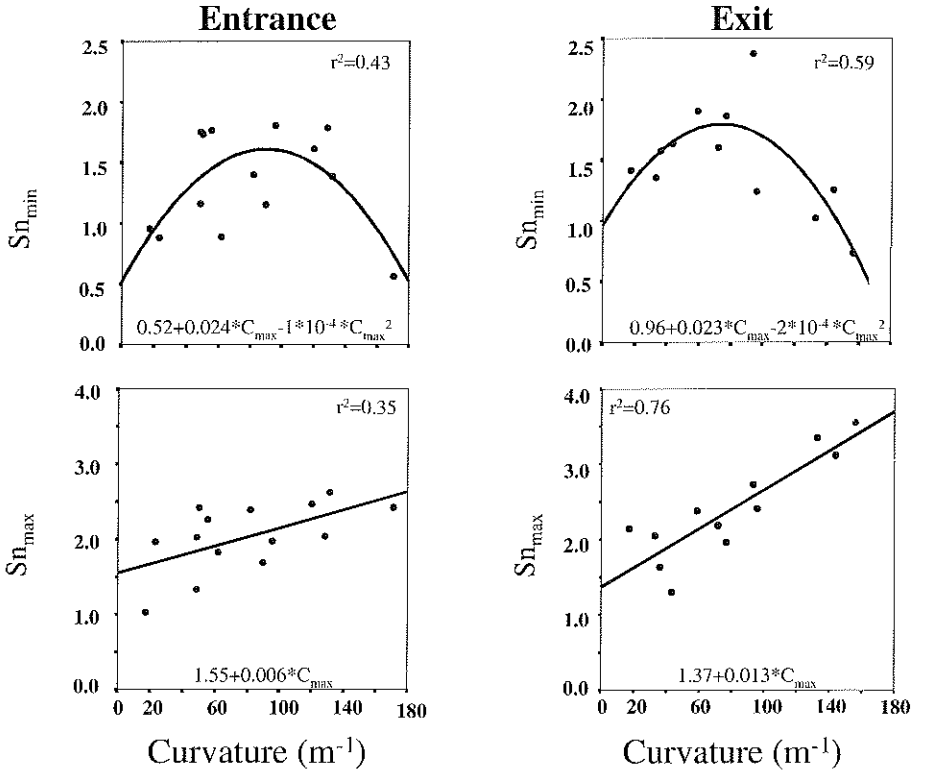

Figure 5: The minimal (Sn_{min}) and maximal (Sn_{max}) normalized shear stress in the outer curve related to the curvature at the entrance and exit of the stent.

Whereas for high flow conditions at each location the normalized shear stress was related to the curvature (Figure 5). The Sn_{max} at both the entrance and exit of the stent increases with increasing curvatures, while Sn_{min} increases for low curvatures, followed by a decrease with increasing curvatures.

Stent implantation after PTCA, prevents the artery from recoil and remodeling but in 20%-35% of the patients restenosis is still observed, now mainly caused by neointimal formation. As a variety of mechanism, related to neointimal formation are related to shear stress, it is desired to have a method enabling to study shear stress alterations in vivo over time.

Table 3: Shear stress before and after stent implantation in the inner and outer curve of the coronary arteries

Shear stress	S_{min} *entrance* (N/m^2)				S_{max} *entrance* (N/m^2)			
	low		*high*		*low*		*high*	
	pre	*post*	*pre*	*post*	*pre*	*post*	*pre*	*post*
Inner curve	**0.64**	**0.78**	**2.62**	**3.59**	**0.61**	**1.06***	**2.58**	**5.50***
SD	0.31	0.47	1.17	2.36	0.28	0.48	1.03	2.24
Outer curve	**0.74**	**0.64**	**4.10**	**3.57**	**0.86**	**1.30**	**4.61**	**8.26***
SD	0.67	0.49	3.06	2.92	0.58	0.92	3.18	5.99
Normalized shear stress	Sn_{min} *entrance*				Sn_{max} *entrance*			
Inner curve	**1.03**	**0.99**	**1.11**	**1.10**	**1.09**	**1.51***	**1.19**	**2.09***
SD	0.17	0.12	0.31	0.24	0.22	0.31	0.38	0.64
Outer curve	**1.04**	**1.00**	**1.31**	**1.38**	**1.19**	**1.44***	**1.77**	**2.29***
SD	0.11	0.18	0.44	0.42	0.18	0.12	0.44	0.32

Shear stress	S_{min} *exit* (N/m^2)				S_{max} *exit* (N/m^2)			
	low		*high*		*low*		*high*	
	pre	*post*	*pre*	*post*	*pre*	*post*	*pre*	*post*
Inner curve	**0.82**	**0.48**	**3.75**	**1.74#**	**0.82**	**1.07***	**3.74**	**4.88**
SD	0.49	0.14	2.53	0.91	0.57	0.54	3.16	2.76
Outer curve	**0.87**	**0.74**	**4.93**	**4.21**	**1.13**	**1.39**	**6.86**	**9.00#**
SD	0.42	0.42	2.25	2.48	0.72	0.58	4.01	3.31
Normalized shear stress	Sn_{min} *exit*				Sn_{max} *exit*			
Inner curve	**1.08**	**0.72***	**1.10**	**0.64***	**1.04**	**1.18***	**1.13**	**1.33#**
SD	0.28	0.21	0.37	0.33	0.10	0.10	0.23	0.24
Outer curve	**1.20**	**0.89**	**1.75**	**1.24**	**1.39**	**1.64#**	**2.06**	**2.74***
SD	0.22	0.20	0.34	0.38	0.25	0.36	0.52	0.67

S_{max} (Sn_{max}): maximal (normalized) shear stress and S_{min} (Sn_{min}): minimal (normalized) shear stress at a certain location in the inner and outer curve near the entrance and exit of the stent before (pre) and after (post) stent implantation for low and high flow conditions *:$p<0.05$; #:$0.05 < p < 0.065$, pre vs. post

In this study we describe a first application of a recently developed 3-D reconstruction technique that enabled us to study alterations in 3-D geometry by stent implantation in vivo. By combining this technique with computational fluid dynamics the changes in shear stress distribution could be evaluated.

Our results demonstrate that implantation of stents in curved coronary arteries increased the local curvature and the local Dean numbers near the stent edges. The geometrical changes resulted in alterations in shear stress distribution at the vessel wall again concentrated around the stent edges. The present findings will be discussed in relation to changes in 3-D geometry and to changes in 3-D shear stress distribution separately.

5.5.1 3-D Vessel geometry

Although the stent diameter was selected to be much larger than the measured native vessel diameter, the IVUS determined diameter immediately after stenting was still slightly decreased. The observed decrease approximately corresponds to the total thickness of the stent wires. Because we did not apply balloon dilatation this suggests that the vessel wall could generate sufficient force to withstand, at least temporarily, the Wallstent self-expanding force, to maintain its original diameter.

The most prominent increments in curvature after Wallstent placement were seen near the stent edges, although a slight non-significant straightening of the vessel was noted in the remainder of the stented segment (data not shown). These prominent edge effects were probably due to the much higher axial stiffness of the stent with respect to the blood vessel wall. Because of these edge effects we focussed our detailed shear stress analysis on these regions.

5.5.2 Shear stress distribution

Regional shear stress, in the present analysis is mainly dependent on local diameter and local curvature. Hence, to discriminate between diameter and curvature effects we normalized shear stress to its value obtained from the Poisseuille law. Therefore, in our analysis to study the influence of curvature only the normalized shear stress was used. From the similarity between normalized and non-normalized shear stress values and the significant relationships between normalized shear stress and curvature, we conclude that curvature changes near the stent edges is a more important factor explaining changes in shear stress distribution after stent placement than local diameter.

Consequently, the maximal shear stress in the outer curve increased with increasing curvature, which might be explained by the centrifugal forces induced by the curvature. In contrast, the minimal shear stress decreased in the high curvature range. This can not be explained by the curvature, but might be related to the gradients in curvature. These high gradients in curvature probably induce separation zones, resulting in low shear stress regions at the stent edge. As

evidence exists that low shear stress may stimulate cellular growth one should be aware of such low shear stress regions when studying neointimal formation (Bauters *et al.*, 1996; Salam *et al.*, 1996).

5.5.3 Assumptions and Limitations

The calculations were performed under the assumption of rigid coronary arteries, Newtonian fluid and steady flow. It has been shown, that the pulsatile velocity field in elastic arteries is similar to the steady velocity field in rigid arteries (Reuderink, 1991)

However, low shear regions may be slightly different from locations, derived from pulsatile inflow conditions. This may have implications when studying relationships with neointimal formation.

Measurements were performed acutely. Whether changes in shear stress occur over time by changes in Wallstent geometry warrants further study. Furthermore, measurements were performed in normal coronary arteries. Hence, asymmetries caused by eccentric lesions in atherosclerotic arteries and also varying stiffness of lesions may cause additional variations.

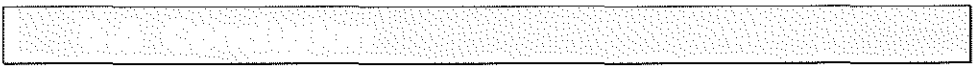

This is the first study in pigs that quantifies *in vivo* changes in 3-D coronary geometry and 3-D shear stress distribution caused by Wallstent implantation. Implantation of stents, without previous balloon dilatation, locally increased the curvature of the artery near the stent edges, which resulted in a high and low shear stress regions near the stent edges. These regions may have implications for neointimal formation.

The technical assistance of Jurgen Ligthart and Stefan Krabbendam is greatly acknowledged. This study was supported by a grant of the ICIN (Project 18).

Bauters, C., Meurice, T., Hamon, M., McFadden, E., Lablanche, J. M. and Bertrand, M. E. (1996) Mechanisms and prevention of restenosis: from experimental models to clinical practice. *Cardiovasc Res* **31**, 835-46.

Bruining, N., von Birgelen, C., di Mario, C., Prati, F., Li, W., den Hoed, W., Patijn, M., de Feijter, P., Serruys, P. and Roelandt, J. (1995) Dynamic three dimensional reconstruction of ICUS images based on an ECG-gated pull back device. *IEEE Computers in cardiology* **95CH35874**, 633-636.

Fischman, D., Leon, M., Baim, D., Schatz, R., Savage, M., Penn, I., Detre, K., Veltri, K., Ricci, D., Nobuyoshi, M. and Investigators, e. a. f. t. S. R. S. (1994) A randomized comparison of coronary stent placement and balloon angioplasty in the treatment of coronary artery disease. *N Engl J Med* **331**, 539-541.

Fontaine, A. B., Spigos, D. G., Eaton, G., Das Passos, S., Christoforidis, G., Khabiri, H. and Jung, S. (1994) Stent-induced intimal hyperplasia: are there fundamental differences between flexible and rigid stent designs? *J Vasc Interv Radiol* **5**, 739-44.

Laban, M., Oomen, J. A., Slager, C. J., Wentzel, J. J., Krams, R., Schuurbiers, J. C. H., den Boer, A., von Birgelen, C., Serruys, P. W. and de Feijter, P. J. (1995) " ANGUS: A new approach to three-dimensional reconstruction of coronary vessels by combined use of angiography and intravascular ultrasound". *Computers in Cardiology* **95CH35874**, 325-328.

Leon, M. B., Popma, J. J., Mintz, G. S., Pichard, A. D., Satler, L. F. and Kent, K. M. (1996) An overview of US coronary stent trials. *Semin Interv Cardiol* **1**, 247-54.

Li, W. (1997) Image and signal processing in intravascular ultrasound. *dissertation.*

Malek, A. and Izumo, S. (1995) Control of endothelial cell gene expression by flow. *J. Biomech.* **28**, 1515-1528.

McKay, S., Potel, M. and Rubin, J. (1982) Graphics methods for tracking three-dimensional heart wall motion. *Comp Biomed Res.* **15**, 455-473.

Mintz, G. S., Popma, J. J., Pichard, A. D., Kent, K. M., Satler, L. F., Wong, C., Hong, M. K., Kovach, J. A. and Leon, M. B. (1996) Arterial remodeling after coronary angioplasty: a serial intravascular ultrasound study. *Circulation* **94**, 35-43.

Nikol, S., Huehns, T. and Hofling, B. (1996) Molecular biology and post-angioplasty restenosis. *atherosclerosis* **123**, 17-31.

Peacock, J., Hankins, S., Jones, T. and Lutz, R. (1995) Flow instabilities induced by coronary artery stents: assessment with an in vitro pulse duplicator. *J Biomech* **28**, 17-26.

Reuderink, P. (1991) Analysis of the flow in a 3D distensible model of the carotid artery bifurcation. *Thesis Eindhoven* wibro dissertatiedrukkerij, Helmond, ISBN 90-9004413-2.

Salam, T., Lumsden, A., Suggs, W. and Ku, D. (1996) low shear stress promotes intimal hyperplasia thickening. *Journal of vascular investigation* **2**, 12-22.

Sassen, L. M., Soei, L. K., Heere, T. J., van Woerkens, L. J., Saxena, P. R. and Verdouw, P. D. (1989) Nicorandil and cardiovascular performance in anaesthetized pigs with a concentric coronary artery stenosis. *Naunyn Schmiedebergs Arch Pharmacol* **340**, 733-9.

Serruys, P., de Jaegere, P., Kiemeneij, F., Macaya, C., Rutsch, W., Heyndrickx, G., Emanuelsson, H., Marco, J., Legrand, V., Materne, P., Belardi, J., Sigwart, U., Colombo, A., Goy, J., van den Heuvel, P., Delcan, J. and Morel, M. (1994) A comparison of balloon-expandable-stent implantation with balloon angioplasty in patients with coronary artery disease. *N Engl J Med* **331**, 489-495.

Slager, C., Wentzel, J., Oomen, J., Schuurbiers, J., Krams, R., von Birgelen, C., Tjon, A., Serruys, P. and de Feyter, P. (1997) True reconstruction of vessel geometry from combined X-ray angiographic and intracoronary ultrasound data. *Semin Intervent Cardiol* **2**, 43-47.

Slager, C. J., Laban, M., von Birgelen, C., Krams, R., Oomen, J. A. F., den Boer, A., Wenguang, L., de Feyter, P. J., Serruys, P. W. and Roelandt, J. R. T. C. (1995) "ANGUS: A new approach to three-dimensional reconstruction of geometry and orientation of coronary lumen and plaque by combined use of coronary angiography and IVUS". *J Am Coll Cardiol* **25**, 144A.

Strony, J., Beaudoin, A., Brands, D. and Adelman, B. (1993) Analysis of shear stress and hemodynamic factors in a model of coronary artery stenosis and thrombosis. *Am J Physiol* **265**, H1787-96.

van de Vosse, F. N., van Steenhoven, A. A., Segal, A. and Janssen, J. D. (1989) A finite element analysis of the steady laminar entrance flow in a 90° curved tube. *Int. J. Num. Methods in Fluids* **9**, 275-287.

van der Giessen, W. J., Serruys, P. W., van Beusekom, H. M., van Woerkens, L. J., van Loon, H., Soei, L. K., Strauss, B. H., Beatt, K. J. and Verdouw, P. D. (1991) Coronary stenting with a new, radiopaque, balloon-expandable endoprosthesis in pigs. *Circulation* **83**, 1788-98.

White, F. and Bloor, C. (1981) Coronary collateral circulation in the pig: correlation of collateral flow with coronary bed size. *Basic Res. Cardiol.* **76**, 189-196.

The Relationship between Neointimal Thickness and Shear Stress after Wallstent Implantation in Human Coronary Arteries

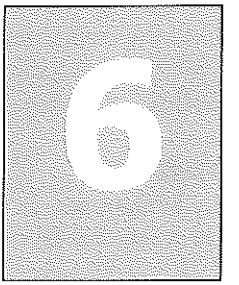

JJ Wentzel, R Krams, J Kloet, WJ van der Giessen, PW Serruys, CJ Slager

Background

In-stent restenosis by excessive intimal hyperplasia is a major limiting problem in the long term clinical efficacy of coronary stents. As shear stress plays a role in a variety of processes related to plaque growth in atherosclerosis, we investigated whether variations in shear stress cause variations in neointimal formation.

Methods

In 14 patients, at 6 months follow up after coronary Wallstent implantation, 3-D stent and vessel reconstruction was performed with a combined angiographic and IVUS technique (ANGUS). The bare stent reconstruction was used as input to calculate in-stent shear stress (SS) at implantation applying computational fluid dynamics. The flow was selected to deliver an average shear stress of 1.5 N/m^2 (15 $dynes/cm^2$). Shear stress and neointimal thickness values were obtained with a resolution of 90^o in the vessel circumferential direction and 2.5 mm in the longitudinal direction. For each vessel, the relationship between neointimal thickness and shear stress was obtained by linear regression analysis. Averaging the individual slopes and intercepts of the regression lines summarized the relationship between neointimal thickness and shear stress.

Results

The average neointimal thickness was 0.44±0.20 mm. Neointimal thickness was inversely related to shear stress: Th=(0.59±0.24)-(0.08±0.10)*SS, $p<0.05$). In addition, the presence of hypercholesteremia at intake appeared discriminative for the observed findings as for these patients (n=5) neointimal thickness was not related to shear stress: Th=(0.40±0.23)-(0.007±0.06)*SS, p=NS. For the non-hypercholesteremic patients (n=9) the averaged relationship was: Th=(0.69±0.19)-(0.12±0.10)*SS, $p<0.05$.

Conclusion

These data show for the first time *in patients,* that neointimal thickness in Wallstents at 6 months follow up is inversely related to shear stress, except for patients with hypercholesteremia. These findings support a hemodynamic mechanism underlying in-stent neointimal hyperplasia formation.

Stents have been shown to reduce restenosis by preventing the artery from arterial shrinkage ('negative remodeling'). However, considerable neointimal formation may still be observed causing renarrowing of the treated arteries (Fischman *et al.*, 1994; Serruys *et al.*, 1994).

Neointimal formation is often observed at specific locations in the stented segment (Fontaine *et al.*, 1994). A number of risk factors, like thrombus formation (Rogers and Edelman, 1995) and endothelial dysfunction (van Beusekom *et al.*, 1998) are related to restenosis but their relationship with its specific distribution is unknown. Localizing factors studied are plaque burden (de Smet *et al.*, 1997; Prati *et al.*, 1999) and wall stress (Vorwerk *et al.*, 1994). In this study we focus on the role of shear stress. Shear stress plays an important role in several growth-related processes (Brownlee and Langille, 1991; Cho *et al.*, 1997). For instance low shear stress regions in vascular bypass grafts show increased neointimal growth (Salam *et al.*, 1996).

To study localization patterns in shear stress and neointimal thickness we applied a recently developed technique, which combines a 3-D reconstruction technique (ANGUS) (Slager *et al.*, 1997)) with computational fluid dynamics.

Our aim was to investigate the relationship between local variations in shear stress and local variations in neointimal thickness after stent placement to evaluate the hypothesis that the locations with low shear stress show more neointimal growth than locations with high shear stress.

6.2.1 Patients

Fourteen patients were studied 6 months after successful implantation of a coronary Wallstent™ (Schneider AG, Bülach, Switzerland) in a population of coronary artery disease. Only patients with no more than two major side branches in the stented segment were included in this study. Table 1 reports the demographic parameters of the patient population. Written informed consent was obtained from every patient to participate in this study.

6.2.2 3-D reconstruction of coronary arteries

3-D reconstruction of the coronary arteries was performed applying a combination of ANGiography and intravascular UltraSound (ANGUS) (Slager *et al.*, 1997). A detailed description of the 3-D reconstruction method has been presented elsewhere (Laban *et al.*, 1995; Slager *et al.*, 1997). Briefly, a sheath based intravascular ultrasound catheter (CVIS 2.9F, Sunnyvale CA, USA) was positioned distally from the stented vessel segment and was filmed with a biplane

angiographic system (Siemens, Bicor, Erlangen, Germany) just after the start of pull back. To eliminate respiratory motion and cardiac motion artifacts on the 3-D path reconstruction, a single biplane view at end diastole of the catheter position was selected and digitized. From the biplane views, a customly written algorithm, developed in MATLAB (The Mathworks, Natick, Mass, USA), was used to reconstruct the transducer path in 3-D space (Laban *et al.*, 1995). In addition, to avoid cardiac motion artifacts, the intravascular ultrasound (IVUS) vessel cross sectional images were collected at end-diastole using an ECG triggered, motorized IVUS pull back operating with a stepsize of 0.5 mm (Bruining *et al.*, 1995) (TomTec, Munich, Germany). Subsequently, the frames were digitized and analyzed with a semi-automatic contour detection program (Li, 1997). Output of the program consisted of lumen contours, signifying the blood-vessel interface and stent contours, representing the stent-neointima interface. Figure 1A displays the respective borders obtained inside and outside the stented segment.

Table 1 : Demographic parameters

Number of vessels	14
Age	63±11 years
Sex (M,F)	8M, 6F
Hypercholesteremia *	5
Smoking #	8
Hypertension	4
Hematocrit	0.38±0.04 units
RCA	5
LAD	7
LCX	2
Diabetes Mellitus	2

M: man, F: female, RCA: right coronary artery, LAD: left anterior descending artery, LCX: left circumflex artery, *: (>6.5 mmol/l),#: (previous and current smoking)

Subsequently, the lumen contours were filtered and positioned perpendicular onto the reconstructed 3-D catheter path, which served as a backbone for the reconstruction. The same procedure was performed for the stent contours only. The angular position of the ultrasound transducer, and thus of the ultrasound images, was determined on basis of a comparison between simulated silhouette images derived from the 3-D stent reconstruction with the actual coronary stent angiogram (Slager *et al.*, 1998). Finally, two 3-D reconstructions were obtained from a) the coronary vessel lumen allowing calculation of a 3-D lumen velocity profile b) the stent contours only. The 3-D reconstructions of the stent were used as the approximated lumen after stenting to calculate shear stress at the stent surface.

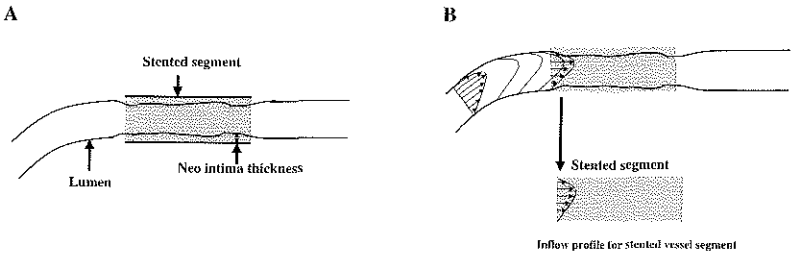

Figure 1: A) Longitudinal overview of the vessel indicating the border information obtained from IVUS B) Determination of the inflow profile for computational fluid dynamics in the 3-D reconstruction of the stent, as derived from the local lumen inflow profile.

6.2.3 Computational fluid dynamics

For shear stress calculations, the non-linear incompressible 3-D Navier Stokes equations, describing the movement of fluid elements in 3-D space, need to be solved. For this purpose a well-validated finite element software package (Sepran, Sepra, Leiden, The Netherlands) was used, which was implemented on a workstation (HP 715/80). For application of such a finite element method, it is necessary to subdivide the 3-D space into bricks ('mesh generation') and to define appropriate boundary conditions.

Mesh generation

The 3-D lumen geometry of the vessel was used to generate the luminal mesh. Therefore, the vessel was axially divided into approximately 100 cross sections, resulting in an axial resolution ranging from 0.2 to 0.9 mm. Each cross section was filled by 32 brick like elements with 16 elements at the lumen surface thereby increasing the resolution towards the stent surface. Each element contained 27 nodes. The cross sectional resolution purposely ranged from: 0.05-0.83 mm^2. The same procedure was applied to the 3-D reconstruction of the stent. The axial resolution of the mesh in the 3-D reconstruction of the stent was set equal to the resolution of the mesh of the lumen.

Boundary conditions and numerical solution

The Navier Stokes equations were implemented in each node of the mesh. The non-linear convective terms in these equations were linearized by a Newton-Raphson method. To obtain the pressure unknowns a penalty function approach was used. In combination with the boundary conditions the differential equations were solved with a numerical accuracy of 0.1 mm/s applying a direct profile

method (Cuvelier *et al.*, 1986). We used the following assumptions and boundary conditions.

We assumed that blood behaves as a Newtonian fluid with a viscosity of $3*10^{-3}$ Pa.s and a density of 1050 kg/m^3. At the wall no slip and at the outflow zero stress conditions were applied. For each vessel, the flow was determined to reach an average shear stress of 1.5 N/m^2 (15 dynes/cm^2) as derived from applying the Poisseuille formula on the average stent cross sectional diameter. As a first step this flow was applied, with a parabolic inflow profile, to the entrance of the lumen reconstruction and the velocity profiles in the lumen were calculated. Secondly, from these results, the 3-D velocity profile at the entrance of the stent was selected and adapted to be used as inflow profile for the fluid dynamic calculations to be applied to the stent reconstruction (Figure 1B). For this purpose, the profile was magnified in area and shape to fit the stent reconstruction while maintaining the previously determined flow. Only the latter calculation was used to obtain shear stress at the surface of the stent.

6.2.4 Analysis of neointimal thickness and shear stress

Only the stented vessel segments were analyzed. The locations of side branches were selected with the help of the IVUS data. Since side branches influence the local velocity profile and thereby may affect the distribution of neointimal thickness, cross sections containing the side branch as well as adjacent segments with a length equal to the diameter of the side branch were removed from our data set. Furthermore, part of the entrance and exit of the stent, covering a length of one stent diameter, were separated from the data set. These parts were analyzed separately.

The following parameters, based on either the 3-D vessel geometry or 3-D velocity calculations, were calculated with in house developed software implemented in Matlab® (Mathworks Inc.,Mass, USA).

The location of the inner curve and outer curve of the 3-D reconstructions was calculated using a plane fitted through all points of the geometric center of the lumen. The vector in each cross sectional IVUS plane, passing through the center of mass and parallel to the fitted plane points to the inner and outer vessel wall.

For each cross section, the distance between lumen and stent contours was used to determine *neointimal thickness* (Th) at 16 locations over the vessel circumference. The neointimal thickness was filtered by a 5*5 point moving average filter and the average neointimal thickness (Th_a) of the whole stented vessel segment was calculated. For each cross-section the minimal and maximal neointimal thickness were determined and their location was compared to respectively the location of the outer and inner curve. Subsequently for each vessel the average minimal and maximal thickness were calculated.

For the cross-sections near the stent edges, the neointimal thickness was calculated and filtered as described before. The average neointimal thickness was calculated for the entrance and exit of the stent separately. These data were compared to the thickness in the remaining part of the stent.

Shear stress at the stent surface was locally calculated from the product of the velocity gradient at the wall and viscosity. The shear stress (SS) values were also filtered applying a 5*5 point moving average filter and the average shear stress of the whole stented vessel segment was calculated. For each cross-section the minimal and maximal shear stresses were determined and their location was compared to the location of the inner and outer curve. For each vessel the average minimal and maximal shear stress was calculated.

The ratio of the maximal to the minimal value of the *neointimal thickness and shear stress* at each cross section was used as an *asymmetry index.* For each artery, the average of the local asymmetry indexes was calculated.

To identify differences between the average neointimal thickness in the regions at the stent edges and the thickness of the central part of the stent (Th_a) a paired t-test was used. The influence of demographic parameters on the average neointimal thickness and the asymmetry index for neointimal thickness was tested applying Student's t-test or univariate regression analysis.

The relationship between shear stress (SS) and neointimal thickness (Th), for each vessel separately, was studied by linear regression analysis, thereby obtaining a slope and an intercept of this relationship. Subsequently, the influence of the demographic parameters on the slopes was tested by Student's t-test or univariate regression analysis. Averaging the individual slopes and intercepts summarized the relationship between neointimal thickness and shear stress for the entire group of patients or a subgroup of patients.

A p-value of <0.05 was considered significant. All values were expressed as mean ± SD. SPSS 8.0 (SPSS Inc. Chicago, Illinois, USA) was used for all statistical calculations.

For all the patients 3-D reconstruction of the coronary arteries was performed successfully. Figure 2 shows a 3-D reconstruction of a human right coronary artery 6 months after Wallstent implantation showing vessel lumen, vessel wall and neointimal thickness. Table 2 reports on the angiographic data of the patients before and after stent implantation and at follow up. In the follow up period the stent length decreased by 2.7% (paired t-test $p<0.05$).

Table 2: Angiographic parameters

Mean diameter post	3.23±0.33 mm
MLD pre	0.93±0.34 mm
MLD post	2.92±0.31 mm
MLD fup	1.83±0.51 mm
stent length post	19.78±7.41 mm
stent length follow up	19.24±7.28 mm

MLD: minimal luminal diameter, pre: before stent implantation, post: after stent implantation, fup: follow up

6.4.1 Neointimal thickness

The neointimal thickness for the entire group of patients was: 0.44±0.13 mm. Figure 3 shows an example of a 2-D map of neointimal thickness from which the asymmetrical pattern can be clearly observed. The average minimal and maximal neointimal thickness for the entire group of vessels was 0.30±0.10 mm and 0.58±0.16 mm ($p<0.05$) respectively. These values resulted in an asymmetry index of 2.04±0.36 and was statistically different from 1 ($p<0.05$). The neointimal thickness at the entrance of the stent (0.43±0.20 mm) was not different from the neointimal thickness at the midpart (0.44±0.12 mm) and the exit of the stent (0.45±0.13 mm) (paired t-test, p=NS).

Studying the influence of demographic parameters on the neointimal thickness and the asymmetry index for neointimal thickness showed that only the average neointimal thickness was related to the sex and the age of the patients, while for the asymmetry index no relationship was found (p=NS). Male patients tended to have more neointimal thickness (0.50 ±0.12 mm) than female patients (0.37±0.11 mm, p=0.055), whereas the neointimal thickness was inversely related to the age of the patient (Th_a= (0.84±0.19)-(6.4*10^{-3} ± 2.9*10^{-3})* age mm p=0.049).

6.4.2 Shear stress

The average shear stress for the entire group of vessels was: 1.99 ± 0.24 N/m^2. Figure 4 shows a 2-D map of the shear stress corresponding to the example shown in Figure 3. For the entire group of patients the minimal and maximal shear stress values were respectively 1.39±0.27 N/m^2 and 2.57±0.55 N/m^2 ($p<0.05$).

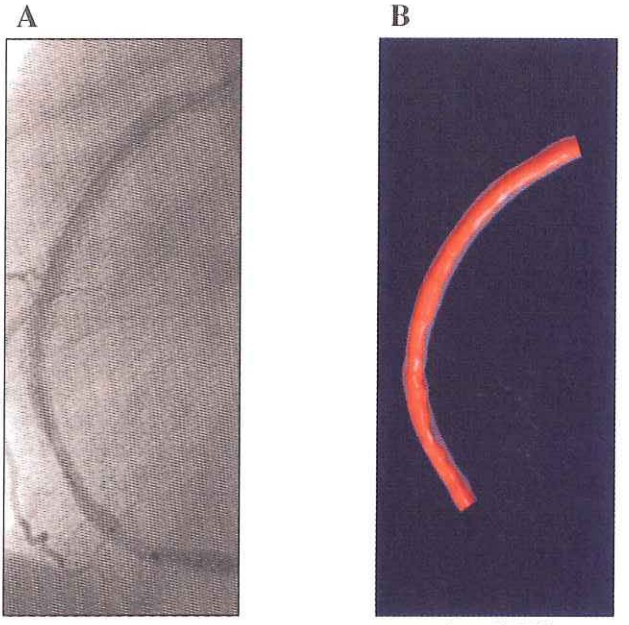

Figure 2: A) Angiogram of stented right coronary artery B) 3-D ANGUS reconstruction of the right coronary artery showing vessel lumen and wall.

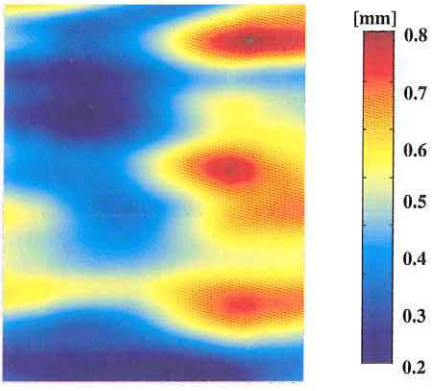

Figure 3: 2-D map of neointimal thickness of human coronary artery shown in Figure 2. Left to right: vessel circumference. Bottom to top: proximal to distal axial vessel location.

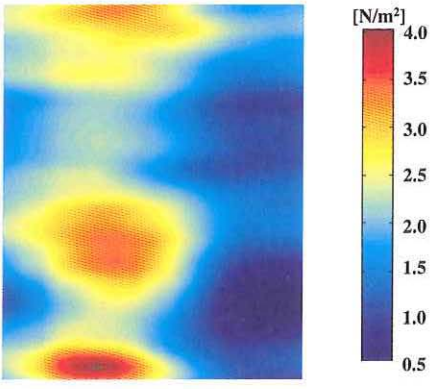

Figure 4: 2-D map of shear stress of a human coronary artery shown in Figures 2 and 3. Left to right: vessel circumference. Bottom to top: proximal to distal axial vessel location.

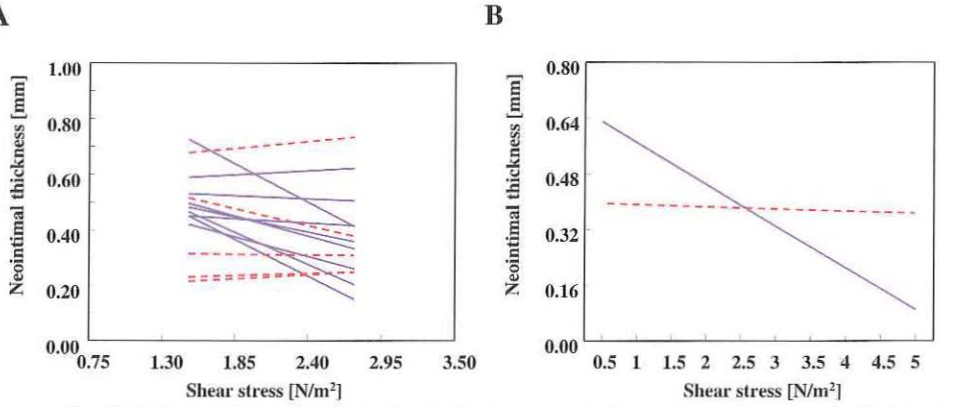

Figure 5: A) Relation between neointimal thickness and shear stress for each individual vessel. The dashed lines indicate the presence of hypercholesteremia. B) The data were pooled according to the presence (--) or absence (-) of hypercholesteremia.

Consequently the asymmetry index was equal to 2.12±0.96, which was statistically different from 1 ($p<0.05$).

6.4.3 Neointimal thickness related to shear stress

For each individual vessel, the relation between neointimal thickness and shear stress was determined. For 9 out of 14 vessels an inverse relation between neointimal thickness and shear stress was observed (Figure 5A), implying that neointimal thickness at the low shear stress locations was higher than at the high shear stress locations ($p<0.05$). The average relationship between neointimal thickness and shear stress could be described by: Th=(0.59±0.24)-(0.08±0.10)*SS, $p<0.05$. Interestingly, the slope of this relationship appeared to be dependent on the presence of hypercholesteremia at intake. For the patients, indicated as hypercholesteremic (n=5), neointimal thickness and shear stress were not related (Th=(0.40±0.23)-(0.007±0.06)*SS, p=NS). For the remaining group (n=9) the average could be described by: Th=(0.69±0.19)-(0.12±0.10)*SS, $p<0.05$. In Figure 5B the average relationship between neointimal thickness and shear stress for patients with and without hypercholesteremia at intake is displayed.

The spatial geometric relationship between neointimal thickness and shear stress can be appreciated from an overview of the geometrical location of the lesions in the total group of patients. In Figure 6A the distribution of the difference in angle in the cross sectional plane between the location of the inner curve (IC) and the maximal neointimal thickness is shown. In Figure 6B a similar graph is displayed for the minimal shear stress location related to the inner curve. A 3-D view of these data (Figure 6E), combining the previous figures, revealed that the maximal

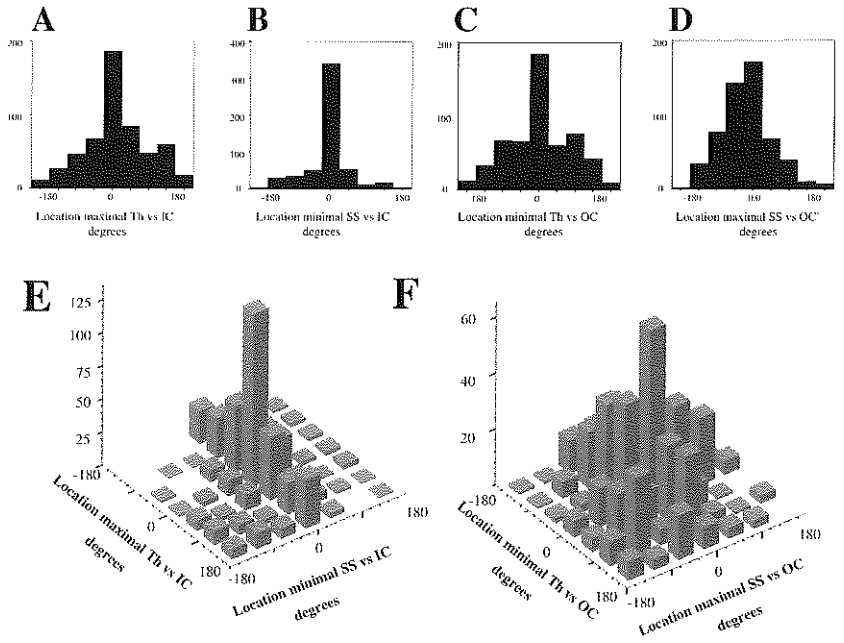

Figure 6: A) Histogram showing the location of the maximal neointimal thickness (Th) relative to the location of the inner curve (IC) expressed in degrees. B) Histogram showing the location of the minimal shear stress (SS) relative to the location of the inner curve expressed in degrees. C) Histogram showing the location of the minimal neointimal thickness relative to the location of the outer curve (OC) expressed in degrees. D) Histogram showing the location of the maximal shear stress relative to the location of the outer curve expressed in degrees. E) 3-D histogram showing the location of the maximal neointimal thickness relative to the location of the inner curve and the location of the minimal shear stress relative to the location of the inner curve as determined for all cross sections expressed in degrees. F) 3-D histogram showing the location of the minimal neointimal thickness relative to the location of the outer curve and the location of the maximal shear stress relative to the location of the outer curve as determined for all cross sections expressed in degrees.

neointimal thickness was preferentially located close to the inner curve of the coronary artery, where also the minimal shear stress was observed. Similarly, the minimal neointimal thickness was more frequently detected in the outer curve (Figure 6C), where also mostly the maximal shear stress was located (Figure 6D). The latter correspondence in location was less pronounced than the former as will be appreciated also from Figure 6F.

Although in the present study the neointimal hyperplasia was moderate, a significant asymmetry in its cross sectional distribution was observed. Neither the average neointimal hyperplasia, nor its asymmetrical distribution could not be explained from well-accepted risk factors. However, neointimal hyperplasia was related to shear stress, such that low shear stress regions were accompanied by maximal intimal thickness and high shear stress regions by minimal neointimal thickness. Even more important, the slope of the relationship between neointimal thickness and shear stress appeared to be dependent on the presence of hypercholesteremia at intake.

6.5.1 Neointimal thickness

The observed average neointimal thickness Th: 0.44±0.13 mm, implies a diameter loss of 0.88 mm, 6 months after Wallstent implantation, and is comparable to the 1.09 mm angiographic change in minimal luminal diameter. Other studies of Wallstent implantation in native human coronaries reported a late loss of 0.78±0.61 mm (Ozaki *et al.*, 1996; Strauss *et al.*, 1992).

The similarity in neointimal thickness of the edges and the midpart of the stent contrasts observations in the Palmaz Schatz stent, where more neointimal formation was observed at the edges and in the midst near the articulation (Hoffmann *et al.*, 1996). The differences in pattern in neointima in both stents might be caused by the differences in stent design, such as the existence of an articulation in the Palmaz Schatz stent (Hoffmann *et al.*, 1996).

6.5.2 Shear stress

The average shear stress in the bare stents derived from the fluid dynamic finite element calculations was 1.99 N/m^2. This is above the aimed average shear stress of 1.5 N/m^2, which by applying Poisseuille to the average cross sectional diameter delivered the input flow for the 3-D calculations. Variations in the actual diameters in relation with the third order power relation of shear stress with diameter, explain the above finding.

6.5.3 Relation between shear stress and neointimal thickness

Mechanisms, thought to be responsible for neointimal formation, are mostly systemic in nature and are not likely to be responsible for the observed asymmetrical pattern in neointimal formation. Indeed, in this study no relationship between the demographic factors and the asymmetry index was observed, so local factors must be involved in this process. In this study shear stress is proposed as such a local factor.

From a global geometrical observation of our cross sectional data (Figure 6) it already became apparent that shear stress and neointimal asymmetry were interrelated. However, in contrast to an earlier study (Krams *et al.*, 1997), in this study we also wanted to incorporate shear stress and intimal thickness variations in the axial vessel direction. Indeed, this extension appeared to be crucial to reach statistically significant results and therefore studying only the cross sectional location of neointima and shear stress extremes related to geometric features will underestimate the importance of shear stress in relation to neointimal thickness.

The observed relation between shear stress and neointimal thickness show close similarity with observations of neointimal formation formed in vascular by pass grafts measured in animal studies (Kohler *et al.*, 1991; Salam *et al.*, 1996). Although in these studies the shear stress was measured more globally, they also observed that the low shear stress was related to neointimal growth (Salam *et al.*, 1996) and high shear stress prevented the graft from neointimal formation (Kohler *et al.*, 1991; Salam *et al.*, 1996).

Other local factors may influence the distribution of neointimal formation. Wall stress is such a local factor sensed somehow by the arterial wall and in normal arteries the wall thickness adapts to local radius in order to control wall stress (Girerd *et al.*, 1994). Whether variations in wall stress exerted by the stent can influence wall asymmetric thickening is not clear. Vorwerk showed that differences in radial force of a Wallstent did not influence the neointimal hyperplasia formation (Vorwerk *et al.*, 1994). We reasoned that for stability, average force exerted by a stent on the wall of the inner curve must equal average force exerted on the outer wall. The outer surface wall area slightly exceeds the inner wall area, therefore we expect the wall stress difference between outer and inner wall to differ by the ratio of these areas. In our range of curvatures and vessel diameters we estimate this difference less than 10%, which is far less than the observed difference in shear stress between inner and outer curve by a factor of 2. In addition, as the observed relation between vessel wall thickness and wall stress (Bevan *et al.*, 1975) is linear, we do not expect that a 10% wall stress variation will produce a 100% variation in neointimal hyperplasia. At a microscopic scale, for example at the location of a stent wire, it might be suggested that local wall stress variations may exist far exceeding 10%. Whether the cancellation by local tissue adaptation of such microscopic unbalances propagates into the observed macroscopic asymmetries is unknown.

Another often-described local risk factor for promoting neointimal hyperplasia is the persistent plaque burden covered by the stent (de Smet *et al.*, 1997; Prati *et al.*, 1999). However, these papers only report on the cross sectional relationship between the area of the plaque burden and the area of the neointimal formation (de Smet *et al.*, 1997; Prati *et al.*, 1999), no data exist whether the observed asymmetries may be explained from the persistent plaque burden. Nevertheless, this subject warrants further study as in eccentric lesions, a

confounding factor like progression of atherosclerosis at the low shear stress side (Krams *et al.*, 1997) may be present. At the other hand, the balloon induced damage and so healing response may be located opposite of the plaque at the remaining free wall.

In respect to the above, the observation that hypercholesteremia influenced the relationship between shear stress and neointimal thickness is most important and emphasizes the likely important role of shear stress in the process of neointimal formation. From several animal and patient studies it is known that shear stress dependent endothelial functions involved in neointimal formation, such as the NO production and the endothelin production (Best *et al.*, 1999; Inoue *et al.*, 1998; Laight *et al.*, 1996), are influenced by hypercholesteremia. Therefore, the finding that the observed shear stress dependent neointimal formation is lost associated with hypercholesteremia strongly suggests the unique role of shear stress in neointimal formation. At the other hand, this finding also stresses the independent role of endothelial function itself in the process of neointimal formation. Further studies are warranted on this interrelationship between shear stress, endothelial function and neointimal hyperplasia.

6.5.4 Limitations of the study

In this study only patients with intermediate neointimal formation could be studied, since only for those patients the stepped IVUS-pull back device could be applied. Because these patients did not show restenosis, our results could be biased and only applicable for mildly neointimal hyperplasia.

In this study no flow measurements were performed. The current analysis assumes the same average shear stress in all patients. Therefore differences in absolute shear stress levels between patients could not be evaluated.

For the 3-D reconstruction of the stents and subsequent computational fluid dynamics only vessel geometries at 6 months were available. Therefore, changes in geometry over the follow up period may have influenced our results. However, the 3% change in stent length observed in this study is relatively small in comparison with the changes found by von Birgelen (13%), as linearly extrapolated from the changes in stent diameter (von Birgelen *et al.*, 1998). However, it is not likely that these minor changes were responsible for the observed asymmetrical pattern in neointimal thickness.

The asymmetry in neointimal hyperplasia thickness in Wallstents as evaluated at 6 months follow up after implantation is predicted by shear stress distribution and not by demographic parameters. Hypercholesteremia at intake abolished this relation. These findings support a hemodynamic theory contributing to the process of in-stent neointimal hyperplasia formation.

Best, P. J., McKenna, C. J., Hasdai, D., Holmes, D. R., Jr. and Lerman, A. (1999) Chronic endothelin receptor antagonism preserves coronary endothelial function in experimental hypercholesterolemia. *Circulation* 99, 1747-52.

Bevan, J. A., Bevan, R. D., Chang, P. C., Pegram, B. L., Purdy, R. E. and Su, C. (1975) Analysis of changes in reactivity of rabbit arteries and veins two weeks after induction of hypertension by coarctation of the abdominal aorta. *Circ Res* **37**, 183-90.

Brownlee, R. D. and Langille, B. L. (1991) Arterial adaptations to altered blood flow. *Can J Physiol Pharmacol* **69**, 978-83.

Bruining, N., von Birgelen, C., di Mario, C., Prati, F., Li, W., den Hoed, W., Patijn, M., de Feijter, P., Serruys, P. and Roelandt, J. (1995) Dynamic three dimensional reconstruction of ICUS images based on an ECG-gated pull back device. *IEEE Computers in cardiology* **95CH35874**, 633-636.

Cho, A., Mitchell, L., Koopmans, D. and Langille, B. L. (1997) Effects of changes in blood flow rate on cell death and cell proliferation in carotid arteries of immature rabbits. *Circ Res* **81**, 328-37.

Cuvelier, C., Segal, A. and van Steenhoven, A. (1986) Finite Element Methods and Navier-Stokes equations. Reidel, 1986, Dordrecht.

de Smet, B. J., Kuntz, R. E., van der Helm, Y. J., Pasterkamp, G., Borst, C. and Post, M. J. (1997) Relationship between plaque mass and neointimal hyperplasia after stent placement in Yucatan micropigs. *Radiology* **203**, 484-8.

Fischman, D., Leon, M., Baim, D., Schatz, R., Savage, M., Penn, I., Detre, K., Veltri, K., Ricci, D., Nobuyoshi, M. and Investigators, e. a. f. t. S. R. S. (1994) A randomized comparison of coronary stent placement and balloon angioplasty in the treatment of coronary artery disease. *N Engl J Med* **331**, 539-541.

Fontaine, A. B., Spigos, D. G., Eaton, G., Das Passos, S., Christoforidis, G., Khabiri, H. and Jung, S. (1994) Stent-induced intimal hyperplasia: are there fundamental differences between flexible and rigid stent designs? *J Vasc Interv Radiol* **5**, 739-44.

Girerd, X., Mourad, J. J., Copie, X., Moulin, C., Acar, C., Safar, M. and Laurent, S. (1994) Noninvasive detection of an increased vascular mass in untreated hypertensive patients. *Am J Hypertens* **7**, 1076-84.

Hoffmann, R., Mintz, G. S., Dussaillant, G. R., Popma, J. J., Pichard, A. D., Satler, L. F., Kent, K. M., Griffin, J. and Leon, M. B. (1996) Patterns and mechanisms of in-stent restenosis. A serial intravascular ultrasound study. *Circulation* **94**, 1247-54.

Inoue, T., Saniabadi, A. R., Matsunaga, R., Hoshi, K., Yaguchi, I. and Morooka, S. (1998) Impaired endothelium-dependent acetylcholine-induced coronary artery relaxation in patients with high serum remnant lipoprotein particles. *Atherosclerosis* **139**, 363-7.

Kohler, T. R., Kirkman, T. R., Kraiss, L. W., Zierler, B. K. and Clowes, A. W. (1991) Increased blood flow inhibits neointimal hyperplasia in endothelialized vascular grafts. *Circ Res* **69**, 1557-65.

Krams, R., Wentzel, J. J., Oomen, J. A., Vinke, R., Schuurbiers, J. C. H., de Feyter, P. J., Serruys, P. W. and Slager, C. J. (1997) Evaluation of endothelial shear stress and 3D geometry as factors determining the development of atherosclerosis and remodeling in human coronary arteries in vivo. Combining 3D reconstruction from angiography and IVUS (ANGUS) with computational fluid dynamics. *Arterioscler Thromb Vasc Biol* **17**, 2061-5.

Laban, M., Oomen, J., Slager, C., Wentzel, J., Krams, R., Schuurbiers, J., den Boer, A., von Birgelen, C., Serruys, P. and de Feijter, P. (1995) ANGUS: A new Approach to Three-Dimensional Reconstruction of Coronary Vessels by Combined Use of Angiography and Intravascular Ultrasound. *IEEE, Computers in Cardiology* **95CH35874**, 325-328.

Laight, D., Matz, J., Caser, B., Carrier, M. and Anggard, E. (1996) Investigation of endogeous nitric oxide vascular function in the carotid artery of cholesterol-fed rabbits. *br.J. Pharmacol.* **117**, 1471-1474.

Li, W. (1997) Image and signal processing in intravascular ultrasound. *dissertation* Erasmus University Rotterdam.

Ozaki, Y., Keane, D., Ruygrok, P., van der Giessen, W. J., de Feyter, P. and Serruys, P. W. (1996) Six-month clinical and angiographic outcome of the new, less shortening Wallstent in native coronary arteries. *Circulation* **93**, 2114-20.

Prati, F., Di Mario, C., Moussa, I., Reimers, B., Mallus, M. T., Parma, A., Lioy, E. and Colombo, A. (1999) In-stent neointimal proliferation correlates with the amount of residual plaque burden outside the stent: an intravascular ultrasound study. *Circulation* **99**, 1011-4.

Rogers, C. and Edelman, E. R. (1995) Endovascular stent design dictates experimental restenosis and thrombosis. *Circulation* **91**, 2995-3001.

Salam, T., Lumsden, A., Suggs, W. and Ku, D. (1996) low shear stress promotes intimal hyperplasia thickening. *Journal of vascular investigation* **2**, 12-22.

Serruys, P., de Jaegere, P., Kiemeneij, F., Macaya, C., Rutsch, W., Heyndrickx, G., Emanuelsson, H., Marco, J., Legrand, V., Materne, P., Belardi, J., Sigwart, U., Colombo, A., Goy, J., van den Heuvel, P., Delcan, J. and Morel, M. (1994) A comparison of balloon-expandable-stent implantation with balloon angioplasty in patients with coronary artery disease. *N Engl J Med* **331**, 489-495.

Chapter 6, Wallstent in coronary artery

Slager, C., Wentzel, J. J., Oomen, J. A., Schuurbiers, J. C. H., Krams, R., von Birgelen, C., Tjon, A., Serruys, P. W and de Feyter, P. J. (1997) True reconstruction of vessel geometry from combined X-ray angiographic and intracoronary ultrasound data. *Semin Intervent Cardiol* **2**, 43-47.

Slager, C. J., Wentzel, J. J., Schuurbiers, J. C. H., Oomen, J., Krams, R., Achterberg, H., Kloet, J. and de Feyter, P. J.(1998) True 3-D reconstruction of coronary arteries in patients shows accurate correspondence between X-ray and IVUS derived dimensions. *Circulation*.vol 98, No 17, I 508

Strauss, B. H., Serruys, P. W., Bertrand, M. E., Puel, J., Meier, B., Goy, J. J., Kappenberger, L., Rickards, A. F. and Sigwart, U. (1992) Quantitative angiographic follow-up of the coronary Wallstent in native vessels and bypass grafts (European experience--March 1986 to March 1990). *Am J Cardiol* **69**, 475-81.

van Beusekom, H., Whelan, D., Hofma, S., Krabbendam, S., van Hinsbergh, V., Verdouw, P. and van der Giessen, W. (1998) Long-Term Endothelial Dysfunction Is more Pronounced After Stenting Than After Balloon Angioplasty in Porcine Coronary Arteries. *J Am Coll Cardiol* **32**, 1109-17.

von Birgelen, C., Airiian, S. G., de Feyter, P. J., Foley, D. P., van der Giessen, W. J. and Serruys, P. W. (1998) Coronary wallstents show significant late, postprocedural expansion despite implantation with adjunct high-pressure balloon inflations. *Am J Cardiol* **82**, 129-34.

Vorwerk, D., Redha, F., Neuerburg, J., Clerc, C. and Gunther, R. W. (1994) Neointima formation following arterial placement of self-expanding stents of different radial force: experimental results. *Cardiovasc Intervent Radiol* **17**, 27-32.

The Role of Regional Shear Stress and Regional Wall Stress in Vascular Remodeling After Balloon Angioplasty

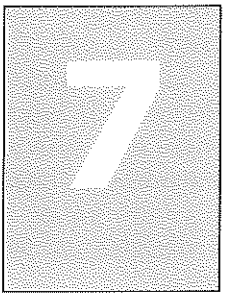

R Krams, JJ Wentzel, J Kloet, I Andhyiswara, JA Oomen, JCH Schuurbiers, D de Kleijn, G Pasterkamp, C Borst, CJ Slager

Chapter 7, PTA in iliac artery

We combined an ultrasound-based 3-D reconstruction technique with computational fluid dynamics to evaluate the role of shear stress and wall stress during vessel shrinkage ('vascular remodeling') induced by balloon angioplasty in atherosclerotic pig arteries. The present study shows that in a model with documented vascular remodeling both regional shear stress and regional wall stress immediately after angioplasty are good predictors of the degree of vascular remodeling. Furthermore, regional shear stress and regional wall stress are within a certain range normalized 6 weeks after balloon angioplasty. The possible underlying mechanisms and their interrelationship are discussed in the present paper.

While balloon angioplasty has been successfully applied for the treatment of obstructive atherosclerotic disease the amount of restenosis (30-50%) remains an important drawback in its applications (Glagov, 1994). Restenosis has long been considered a consequence of excessive neointimal formation (Bauters *et al.*, 1996; Nikol *et al.*, 1996). Recently, animal (Kakuta *et al.*, 1998; Langille, 1993; Pasterkamp *et al.*, 1997; Post *et al.*, 1994) and human studies (Langille, 1993; Pasterkamp *et al.*, 1996) have shown that shrinkage in vessel geometry ('constrictive arterial remodeling') is the major chronic component of restenosis after balloon dilatation. Expansive and constrictive arterial remodeling has been observed in conditions like exercise, embryonic development and experimentally induced high flow conditions, where it is accompanied by normalization of shear stress on the endothelium (Brownlee and Langille, 1991; Kamiya and Togawa, 1980; Langille, 1993). In vitro experiments have shown that shear stress is coupled to the expression of a variety of genes, including those for ecNOS, ET-1, PDGF and MMP-9, which affect smooth muscle cell (SMC) replication, SMC-apoptosis and matrix breakdown and production (Ando *et al.*, 1995; Bassiouny *et al.*, 1998; Friesel and Maciag, 1995; Malek and Izumo, 1992; Sharefkin *et al.*, 1991). All these processes are thought to play a role in vascular remodeling (Langille, 1993).

Vascular remodeling has also been associated with the pressure induced force balance within the vessel wall (Rachev *et al.*, 1998; Thubrikar and Robicsek, 1995). Especially in hypertension, where blood flow and shear stress are hardly changed, the associated medial thickening is presumably adaptive and serves to normalize the increased wall stress (Humphrey, 1995; Rachev *et al.*, 1998; Taylor, 1998). In accordance with these findings is that wall stress activates ion channels, MAP-kinases and stress activated protein kinases (SAPK).

Despite the above findings, the role of shear stress and wall stress in balloon angioplasty related vascular remodeling is presently unknown. Hence, we have extended the 3-D intravascular ultrasound (IVUS) technique to calculate regional shear stress and regional wall stress distributions. With this novel technique we evaluated the role of shear stress and wall stress in remodeling after PTA. For this purpose we performed balloon angioplasty in atherosclerotic Yucatan pigs, which is an well-accepted experimental model for atherosclerosis (Post *et al.*, 1997).

7.2.1 Animal preparation and instrumentation

The investigation conformed with *the Guide for the Care and Use of laboratory Animals* published by the US National Institutes of Health (NIH Publication No. 85-23, revised 1985) and was approved by the ethical committee on Animal Experiments of the Faculty of Medicine, Utrecht University.

A detailed description of the preparation and instrumentation has been reported elsewhere (Post *et al.*, 1997). Briefly, all 6 animals started an atherogenic diet at the age of 7 months, resulting in a sustained 10-fold increase in total cholesterol level to 14.9±4.4 mmol/l and approximately a 3.5-fold increase in HDL level to 2.2±0.3 mmol/l. Two weeks thereafter, a carotid incision was performed and an arterial 8F sheath was placed into the descending aorta under fluoroscopic guidance. Through the sheath an 8F guiding catheter was advanced to the aortic bifurcation to perform contrast angiography (Telebrix, Laboratoire Guerbet, France) and to insert a 4F Fogarty balloon catheter. Denudation of 3-4 cm segments (measured by a radiopaque ruler) in the external iliac arteries was performed by triple withdrawal of the Fogarty catheter that was manually inflated with a 50:50 v/v water contrast mixture. After the procedure, the carotid artery was carefully sutured.

Four months after the denudation, selected sites of the most prominent arterial narrowing were balloon dilated with a standard peripheral (length 5 cm, diameter 6 mm) angioplasty catheter. The balloon was inflated three times for 1 min at a pressure of 10 atmosphere. Before and after balloon intervention, angiography and intravascular ultrasound pullback were performed. After angioplasty the atherogenic diet was replaced by a regular diet.

After a follow up of 42 days, the pigs were anaesthetized again and angiograms and intravascular ultrasound recordings were performed as described above.

During each procedure, heparin was administered (thromboliquine (100 IU/kg), Organon Technika) to the animal. In addition, every 15 min, 25 mg Atropine was given intravenously. One day before intervention, acetyl salicylic acid (125 mg) p.o. was given and continued for 2 weeks after the intervention. During each intervention, a continuous infusion of nitroglycerin (20 µg/ kg/min) was given to prevent arterial spasm. The following sections describe the angiographic and IVUS method in more detail.

7.2.2 Angiography

Angiography was performed before and after each intervention and at follow up. Contrast material was injected selectively into the artery under study through an 8F-guiding catheter. Images were recorded digitally at a cine rate of 12

images/sec using a C-arm fluoroscopic unit (Philips, Eindhoven, The Netherlands) in the frontal position. The images with the highest contrast were selected and stored on DAT tape for further analysis.

The balloon diameter and balloon length were calculated with an in-house developed software package. Briefly, after calibration of the digitized images with a radiopaque ruler, the balloon diameter and balloon lengths were calculated on basis of points manually indicated in the antero-posterior (AP) view of the contrast filled balloon. The position of the balloon was noted as the distance between the side branch distal from the balloon and the distal end of the balloon. This side branch served as a reference point, both for angiography and IVUS pull back.

7.2.3 Intravascular Ultrasound and mesh generation

A continuous IVUS-pull back through the external iliac artery was performed starting at the distal side branch as defined by angiography. Pullback distance was recorded continuously during pull back with an in-house developed measuring device (Li, 1997). From the IVUS recordings cross sections were selected at 0.5 mm intervals, resulting in 100-150 cross sections per blood vessel segment. A well-validated semi-automatic contour-tracking package was used to generate contours between the lumen-intima and media-adventitia borders (Li, 1997).

The stacked IVUS contours served as a template for the generation of the 3-D mesh necessary for the numerical computational fluid dynamics (see below). The axial mesh resolution of the 3-D reconstruction was reduced to 0.5-0.7 mm as the mesh, which consists maximally of 100 cross sections (restricted by computer power) had to be distributed over the 100-150 IVUS cross sections. The mesh completely filled the lumen of the IVUS 3-D reconstruction of the artery. Each cross section of the mesh is composed of 32 elements, and each element contains 27 nodes. This results in a cross sectional resolution of 220 μm to 450 μm for the largest diameter and of 90 to 190 μm for the smallest diameter. This range was a result of a purposely-induced increase in resolution towards the vessel wall. As a consequence the resolution is high when the blood vessel is small, i.e. when velocity gradients are high.

7.2.4 Computational fluid dynamics

At each nodal point of the mesh the 3-D Navier-Stokes equations for incompressible fluids were implemented. The non-linear convective term in the Navier-Stokes equations was linearized with a Newton-Raphson approach and solved with a maximal error of 10^{-4} (m/s). To obtain the pressure unknowns from the discrete Navier-Stokes equations a penalty function approach was used. In combination with boundary conditions this set of linear equations can be solved (Bovendeerd *et al.*, 1987; Vosse *et al.*, 1989). We applied a direct profile method, of a well-validated, finite element package (Sepran, Sepra, Leiden, The

Netherlands), to solve the resulting matrices (Bovendeerd *et al.*, 1987; Vosse *et al.*, 1989).

The following boundary conditions were imposed: parabolic steady inflow at the entrance of the vessel, zero stress at the outlet and no-slip conditions at the vessel wall. The value of mean entrance velocity for each blood vessel at all three time points was set at a flow value of 80 ml/min (Bagshaw *et al.*, 1986). We further assumed that blood behaved as a Newtonian fluid with a density of 1050 kg/m^3 and a viscosity of $3*10^{-3}$ Pa.s.

Alignment of the mesh data, obtained before PTA, after PTA and at follow up was performed with reference to the common distal side branch. The length of each segment was adjusted to the shortest common pull back segment and the resulting differences in resolution were accounted for by linear interpolation procedures (Matlab®, Mathworks Inc., USA). Side branches were removed after selecting them in the IVUS cross sections.

For each cross section, within the balloon dilated vessel segment the parameters as described in Table 1 were calculated. All geometrical parameters (LA, WA and MBA) were obtained by numerical integration, while shear stress (SS) was obtained from the finite element package. The circumferential wall stress distribution (WS) for each cross section was derived assuming a thick walled cylindrical geometry (Gere J.M. and Timoshenko S.P., 1996). Averaging from inner to outer wall resulted in a single average circumferential wall stress value for each cross section. To avoid influence of systemic factors, we divided each parameter by its corresponding value of the average non-dilated or reference segment (Table 1). At corresponding locations and at different time points the acute gain ($\Delta LA_{postpre}$), late loss (ΔLA_{postfu}), normalized change in lumen area ($n\Delta LA_{fupost}$), wall area ($n\Delta WA_{fupost}$) and media bounded area ($n\Delta MBA_{fupost}$), the absolute and normalized changes in shear stress (ΔSS_{fupost} and $n\Delta SS_{fupost}$) and wall stress ($\Delta WS_{fupost}$and $n\Delta WS_{fupost}$) over time were calculated (Table 1).

We automatically determined the location of the minimal lumen area (MLA) for each blood vessel by a computer search and analyzed at that location MLA, MBA, WA, SS, WS, acute gain and late loss before and after angioplasty and at follow up (Table 1).

Table 1: Definition of applied variables

Definitions		Description
LA		Lumen Area (mm^2)
WA		Wall Area (mm^2)
MBA		Media Bounded Area (mm^2)
WS		Wall Stress (kPa)
SS		Shear Stress (N/m^2)
nLA	LA / LA_{ref}	Normalized Lumen Area
nWA	WA / WA_{ref}	Normalized Wall Area
nMBA	MBA / MBA_{ref}	Normalized Media Bounded Area
nWS	WS / WS_{ref}	Normalized Wall Stress
nSS	SS / SS_{ref}	Normalized Shear Stress
$\Delta LA_{postpre}$	$LA_{post}-LA_{pre}$	Acute gain (mm^2)
ΔLA_{postfu}	$LA_{post}-LA_{fu}$	Late loss (mm^2)
$n\Delta LA_{fupost}$	$nLA_{fu} - nLA_{post}$	normalized Lumen Change
$n\Delta WA_{fupost}$	$nWA_{fu}-nWA_{post}$	normalized Wall Growth
$n\Delta MBA_{fupost}$	$nMBA_{fu}-nMBA_{post}$	Normalized media bounded area change *(Vascular remodeling)*
$n\Delta SS_{furef}$	$(nSS_{fu}- 1)*100\%$	Normalization of Shear Stress to reference values at follow up
$n\Delta WS_{furef}$	$(nWS_{fu}- 1)*100\%$	Normalization of Wall Stress to reference values at follow up
$n\Delta SS_{fupre}$	$(nSS_{fu}- nSS_{pre})*100\%$	Normalization of Shear Stress to baseline values
$n\Delta WS_{fupre}$	$(nWS_{fu}- nWS_{pre})*100\%$	Normalization of Wall Stress to baseline values

pre is before angioplasty; post is after angioplasty; fu is at six weeks follow up; ref is reference segment

7.3.1 Data selection and statistics

Before starting statistical analysis the entire data set (791 data points ,1 data point represents 1 cross section) was reduced to include the balloon-dilated segment only (n=500). As a second step, the balloon-dilated segments were stripped 12.5% of length on both ends to exclude matching errors because of uncertainty of balloon lengths at their ends. This reduced the data set to 375 points. In addition, we corrected this reduced data set for spasm by disregarding data points that did not expand after PTA, resulting in a final data set of 222 points.

Minimal lumen area and associated variables were tested for differences in their mean values with a one way ANOVA with repeated measures, followed by a pairwise comparison based on a Student-Newman-Keuls test.

nWS_{post} and nSS_{post} were evaluated as predictors of vascular remodeling and normalized wall change (Table 1) with a multi-regression analysis. Before the analysis each animal was encoded with two dummy variables. One dummy corrected for a difference in offset per animal and one dummy corrected for a difference in slope per animal. An F-test was applied to each set of dummies to

test if addition of the dummies reduced the unexplained variance of the model. The contribution of each significant parameter was determined by its individual sensitivity to the total variation of $n\Delta MBA_{fupost}$. Furthermore, this sensitivity was made dimensionless by normalizing the total variation of $n\Delta MBA_{fupost}$ to unity.

Normalization of shear stress and wall stress was determined by a two step approach. First, the normalized shear stress change over time ($n\Delta SS_{fupre}$) and the normalized wall stress change over time ($n\Delta WS_{fupre}$) were related to acute gain, applying a regression model which included a linear and a quadratic term and the two dummies per animal. Secondly, the individual model predictions per animal were averaged for acute gain at increments of 0.1 mm^2. From these data the prediction interval and the statistical significance of the curve with respect to zero was calculated applying t-tests.

All data are presented as mean±SD. P-values < 0.05 are considered significant. All statistical analysis was performed in SPSS 8.0 (SPSS inc., Chicago, Illinois, USA)

7.4.1 Animals

We studied both the right and left external iliac arteries of 6 atherosclerotic Yucatan pigs, i.e. 12 arteries. One 3-D IVUS acquisition was excluded from the analysis due to technical failure and in one artery no balloon angioplasty was performed. As in the present analysis, three measurements of a single artery were combined, this study therefore includes 10 arteries and 30 3-D reconstructions.

7.4.2 3-D blood vessel reconstruction; geometrical aspects

The 3-D reconstructed lumen of a single blood vessel with shear stress projected onto its surface is displayed in Figure 1. It can be seen that the vascular lumen increased after PTA and returned close to its original geometry during the 6 week follow-up period. For the entire group, MLA and nMLA increased approximately by 44% after PTA (Table 2, $p<0.05$). While MLA returned to its baseline value during follow up, nMLA returned to the value of the reference segment (Table 2). Interestingly, the average lumen area at the reference segment significantly decreased by 30% during follow up period (Table 2, $p<0.05$). MBA and nMBA, at the location of MLA, increased approximately by 32% ($p<0.05$) after PTA. During follow up MBA and nMBA followed a similar pattern as MLA and nMLA, as WA and nWA remained unchanged (Table 2). Furthermore, similar changes in the MBA at the reference segment were observed ($p<0.05$, Table 2). The acute gain and late loss, at the location of MLA, were 5.93±3.25 mm^2 and 6.16±3.80 mm^2, respectively.

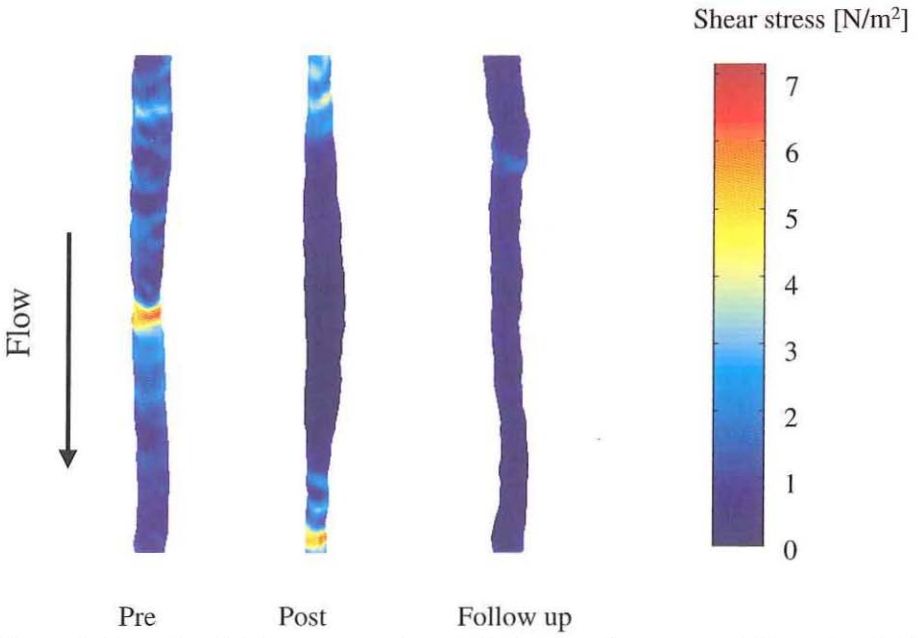

Figure 1: Example of 3-D reconstruction of the lumen of an external iliac artery before, after PTA and at follow-up. Shear stress (N/m^2) is projected on the surface of all three 3-D reconstructions.

7.4.3 3-D blood vessel reconstruction; biophysical aspects

As can be deduced from the color map in Figure 1, shear stress decreases after PTA and returns to baseline values during follow up. For the entire group, shear stress at the location of MLA was 1.9 times the reference value of 0.5 N/m^2 before angioplasty (Table 3). While SS and nSS decreased to almost 30% of baseline values immediately after PTA, SS returned to baseline values and nSS returned to the reference segment value at 6 weeks follow up (Table 3), despite of the change in shear stress at the reference segment ($p<0.05$, Table 3). Both absolute and normalized wall stress increased by 43% after PTA. While absolute wall stress returned to baseline values, normalized wall stress had returned to the reference segment value during follow up (Table 3). The wall stress at the reference was decreased during the follow up period by 27% ($p<0.05$, Table 3).

The relationship of nSS_{pre} , nSS_{post} and nSS_{fu} versus acute gain ($\Delta LA_{postpre}$) are displayed in Figure 2. It can be seen that most of the reduction in shear stress after balloon angioplasty occurs at high acute gains (Figure 2A and 2B). Remarkably, nSS_{fu} was close to unity over the entire range of acute gain values (Figure 2C).

Table 2: Geometrical parameters at the location of minimal area obtained from 3-D IVUS reconstruction of 10 external iliac arteries of 6 atherosclerotic Yucatan pigs.

	Pre	*Post*	*Follow Up*
MLA (mm^2)	12.4±3.2	18.4±3.9^{+}	12.2±2.2^{0}
WA (mm^2)	5.6±1.8	5.4±1.2	5.2±1.2
MBA (mm^2)	18.0±4.5	23.8±3.9^{+}	17.4±2.6^{0}
LA_{ref} (mm^2)	17.3±5.1	n.a.	12.4±4.5*
WA_{ref} (mm^2)	5.4±1.4	n.a.	5.4±1.3
MBA_{ref} (mm^2)	22.7±6.1	n.a.	17.8±5.3*
nMLA	0.77±0.30	1.11±0.39^{+}	1.08±0.28*
nWA	1.09±0.37	1.09±0.42	1.05± 0.29
nMBA	0.84±0.30	1.12±0.32^{+}	1.05±0.22^{0}

MLA: minimal lumen area; WA: wall area; MBA: media bounded area; nMLA: normalized minimal lumen area; normalization to reference segment; nWA: normalized wall area; nMBA: normalized media bounded area, LA_{ref}: lumen area at reference segement, WA_{ref}: wall area at reference segment, MBA_{ref} : media bounded area at reference segment *p<0.05 pre vs. follow up; ^{0} p<0.05 post vs. follow up; $^{+}$ p<0.05 pre vs. post; n.a.: not available

Table 3: Biophysical parameters at the location of minimal area obtained from 3-D IVUS reconstruction of 10 external iliac arteries from 6 atherosclerotic Yucatan pigs.

	Pre	*Post*	*Follow Up*
SS (N/m^2)	0.9±0.4	0.3±0.2^{+}	0.9±0.4^{0}
WS (kPa)	69.1±18.4	99.6±27.1^{+}	70.0±16.6^{0}
SS_{ref} (N/m^2)	0.6±0.3	n.a.	1.0±0.8*
WS_{ref} (kPa)	95±21	n.a.	69±22*
nSS	1.92±0.81	0.62±0.46^{+}	1.01±0.43*
nWS	0.76±0.30	1.11±0.38^{+}	1.06± 0.27*

SS: average cross sectional shear stress; WS: average cross sectional wall stress; nSS: shear stress normalized to reference segment; nWS: wall stress normalized to reference segment; SS_{ref}: shear stress at reference segment;WS_{ref}: Wall stress at reference segement; *p<0.05 pre vs. follow up; ^{0}p<0.05 post vs. follow up; + p< 0.05 pre vs. post; n.a.: not available

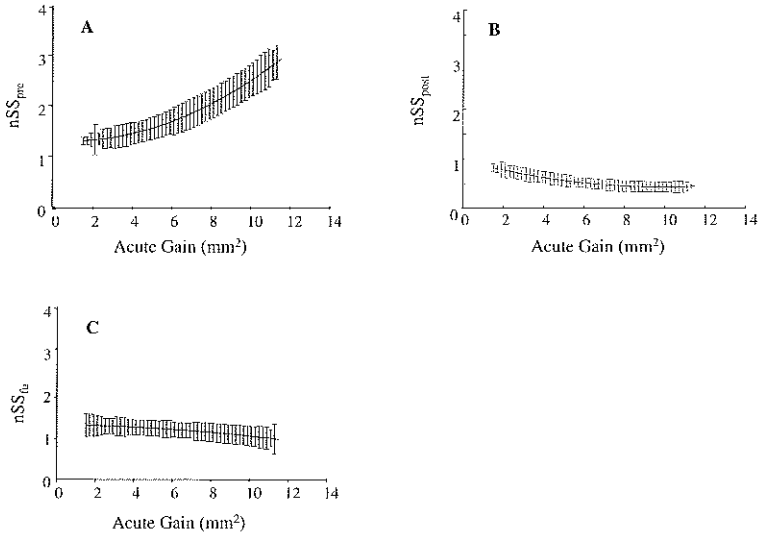

Figure 2: Shear stress before angioplasty (nSS_{pre}; panel A), after angioplasty (nSS_{post}; panel B) and at follow up ($nSS_{fu;}$ panel C) versus acute gain. Indicated is the standard error of the mean for each point on the curve.

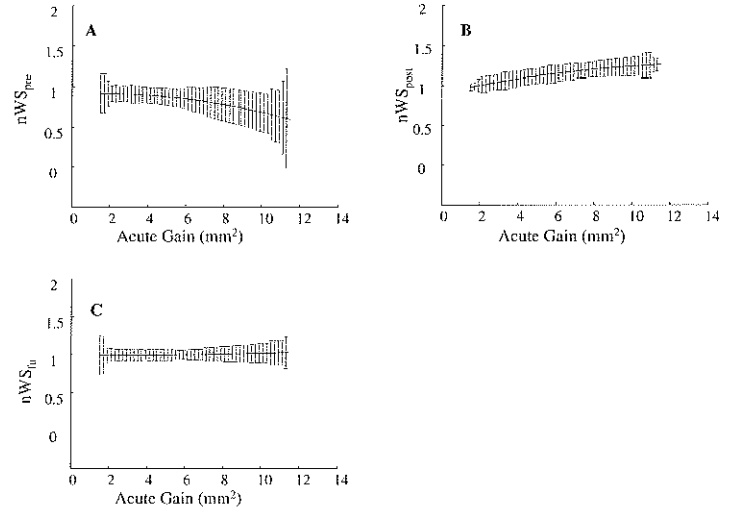

Figure 3: Wall stress before angioplasty (nWS_{pre}; panel A), after angioplasty (nWS_{post}; panel B) and at follow up ($nWS_{fu;}$ panel C) versus acute gain. Indicated is the standard error of the mean for each point on the curve.

As a consequence, $n\Delta SS_{fupre}$ was described by the following relationship: $n\Delta SS_{fupre} = - (1.65\pm0.50) (\Delta LA_{postpre})^2$ ($r=0.74$; $p<0.05$; Figure 4A). The constant and the linear term were not significant. The range over which $n\Delta SS_{fupre}$ was not different from zero was from 0 to 8.6 mm^2. $n\Delta SS_{furef}$, in contrast, was described by the relationship: $n\Delta SS_{furef} = (22.7\pm8.2)$ ($r=0.75$; $p<0.05$; Figure 4C). The linear and quadratic terms were not significantly different from zero.

The relationship of nWS_{pre}, nWS_{post} and nWS_{fu} versus acute gain are displayed in Figure 3. The increase in wall stress after balloon angioplasty was most prominent at high acute gains (Figure 3A and 3B). Of interest is the finding that nWS_{fu}, similar to the findings of nSS_{fu}, was close to unity over the entire range of acute gain values (Figure 3C). The $n\Delta WS_{fupre}$ versus acute gain relationship was non-significant for all the coefficients. Consequently, the $n\Delta WS_{fupre}$ values were equal to zero over the entire range of acute gain values (Figure 4B). The $n\Delta WS_{furef}$ versus acute gain relationship also produced a non-significant relationship versus acute gain (Figure 4D). None of the coefficients were statistically significant. Consequently, the $n\Delta WS_{furef}$ values were equal to zero over the entire range of acute gain values.

7.4.4 Prediction of vascular remodeling and wall growth

Post-angioplasty wall stress and post-angioplasty shear stress were both significant predictors of vascular remodeling as described by the following relationship: $n\Delta MBA_{fupost} = (32.7\pm11.7)*nSS_{post} - (34\pm6.8)*nWS_{post} + (19.6\pm11.4)$ ($r = 0.95$; $p<0.05$). The contribution of nWS_{post}, for three different values of nSS_{post} is displayed in Figure 5A. In addition, the individual contribution of nSS_{post}, is displayed in Figure 5B at three different constant values of nWS_{post}. The relative contribution of nSS_{post} and nWS_{post} to the total variation of $n\Delta MBA_{post}$ is 0.6 and 0.4, respectively. Normalized wall growth is not related to nSS_{post}, or nWS_{post} as derived from the non-significant slopes obtained by univariate analysis (p=NS).

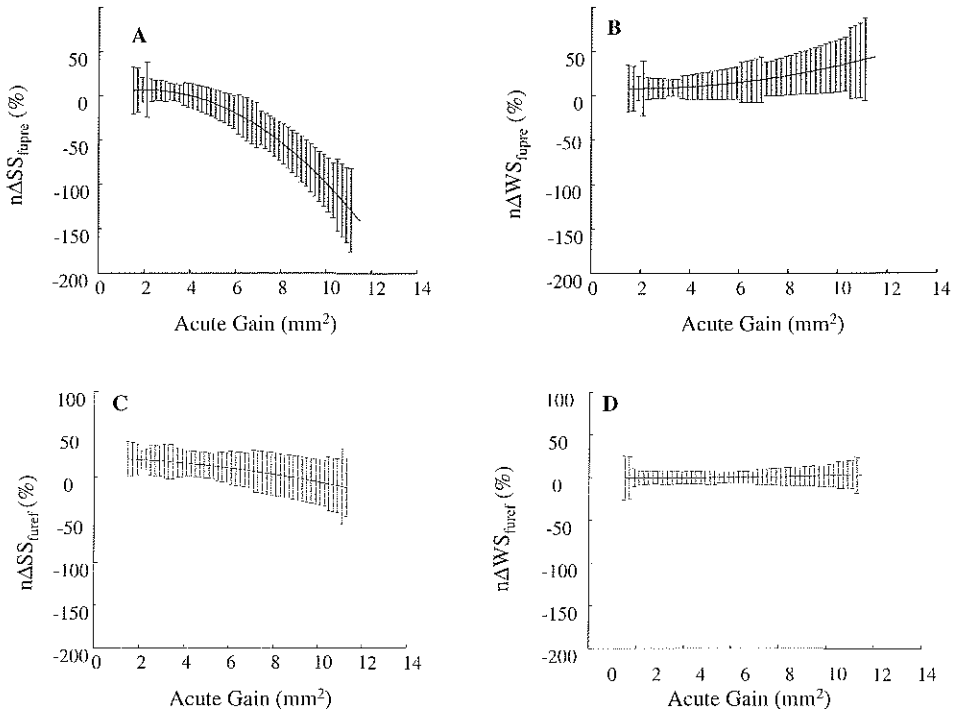

Figure 4: Shear stress ($n\Delta SS_{fupre}$; panel A) and wall stress ($n\Delta WS_{fupre}$; panel B) difference between baseline and follow up versus acute gain. Shear stress ($n\Delta SS_{furef}$; panel C) and wall stress ($n\Delta WS_{furef}$; panel D) differences between the reference value at follow up and actual value inside the balloon-dilated segment at follow up versus acute gain.

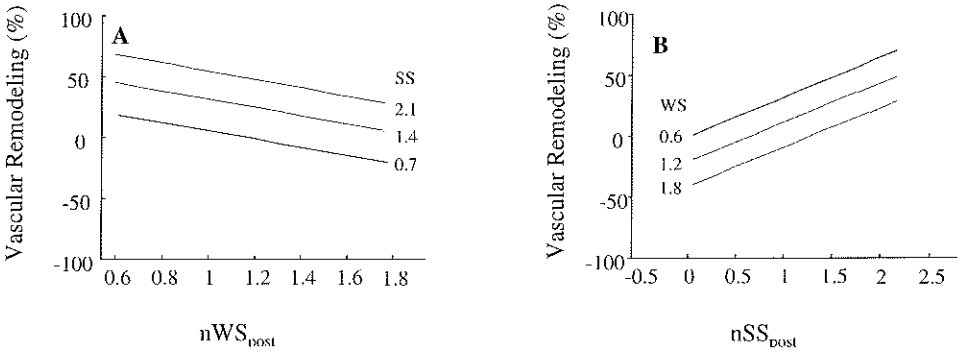

Figure 5: Vascular remodeling: Panel A: model predictions for the individual effect of nWS_{post}, while nSS_{post} was set at 0.7, 1.4 and 2.1 N/m^2; Panel B; model predictions of nSS_{post}, while nWS_{post} was set at 0.6, 1.2 and 2.8 (kPa). These values signify the minimum, average and maximum of the parameter.

Balloon angioplasty has been successfully applied for the treatment of obstructive atherosclerotic disease. However, the amount of restenosis (30-50%) remains an important drawback in its applications (Glagov, 1994). Restenosis has long been considered a consequence of excessive neointimal formation (Bauters *et al.*, 1996; Nikol *et al.*, 1996). Recently, animal (Kakuta *et al.*, 1998; Langille, 1993; Pasterkamp *et al.*, 1997; Post *et al*, 1994) and human studies (Langille, 1993; Pasterkamp *et al.*, 1996) have shown that shrinkage in vessel geometry ('constrictive arterial remodeling') is the major chronic component of restenosis after balloon dilatation. The present study evaluated the role of both shear stress and wall stress in constructive vascular remodeling of atherosclerotic blood vessels in a well-accepted model of vascular remodeling (Post *et al.*, 1994). We will discuss the main findings of the present study separately.

7.5.1 Wall stress control mechanism

Wall stress has been studied extensively in hypertension and heart failure (Rachev *et al.*, 1998; Taylor, 1998; Humphrey, 1995; Williams, 1998). In those conditions, it has been shown that increments in blood pressure induce hypertrophy of the smooth muscle layer to restore wall stress to its baseline value. In atherosclerosis, the role of wall stress is less clear (Thubrikar and Robicsek, 1995) and especially after PTA a paucity of data exists to clarify its role in restenosis. We ordered the regional wall stress values according to the acute gain obtained after PTA, in order to detect relationships related to tissue injury. The ordered regional wall stress values *before* PTA decreased monotonically with lumen gain due to larger plaque accumulation at high acute gain regions. Immediately *after* PTA, wall stress increased up to values of 40% above pre-PTA values at high acute gain. The latter finding seems plausible as at high acute gains regional wall thickness decreases the most and vessel radius increases the most and due to the Laplace law, wall stress then increases the most. Despite these changes in wall stress immediately after PTA, regional wall stress returned to reference values at follow up. This restoration was independent of the acute gain and not related to baseline values. Hence, these findings are compatible with a wall stress control mechanism that is activated after PTA, without a memory for the condition before PTA.

7.5.2 Shear stress control mechanism

Shear stress has been involved in vascular remodeling, in primary atherosclerosis and after experimental conditions of increased flow (Moore *et al.*, 1992; Ku *et al*, 1985; Sabbah *et al.*, 1984), where it was aimed at restoring deviations of a normal value of 1-2 N/m^2. Regional shear stress was approximately 1 N/m^2 at the location of the minimal lumen area before balloon angioplasty, which is in the lower range of normal values reported in literature (1-2 $N*m^{-2}$) (Langille, 1993).

As MLA is the lowest lumen area of each blood vessel, the data indicate that we imposed a slightly low entrance velocity to our blood vessels. Despite this restriction, large spatial variations in regional shear stress with lumen gain before balloon angioplasty were noted. As we could exclude tapering as a source of these findings, these high shear stress regions may therefore signify those areas where the endothelium is dysfunctional or the diffusion distances of vasoactive substances, like NO, are too high. PTA reduces these high shear stress regions by a factor of 3-4. These induced changes in shear stress after PTA are probably large enough to induce changes in gene expression and protein composition of the (regenerated) endothelial layer and smooth muscle cells (Malek and Izumo, 1995).

Shear stress at follow up was close to its own reference value, but differed from regional pre-PTA baseline values. This finding provides strong evidence for a control mechanism for shear stress activation after PTA. As our normalized data, including our wall stress data, are sensitive to the reference segment values, we reanalyzed the diameter of the blood vessel at follow up by angiography performed *before* placement of the IVUS catheter. Diameters from IVUS (3.5 mm) were not different from those obtained with angiography (3.7 mm) excluding IVUS catheter related errors.

7.5.3 Underlying mechanism (Figure 6)

Wall stress, according to the law of Laplace, is influenced both by lumen diameter and by wall thickness. Consequently, normalization of wall stress may occur, in theory, at different vascular diameters. Shear stress, on the other hand, is tightly coupled to lumen dimensions, but not to wall thickness. Hence, normalization of shear stress may lead, in theory, to lumen normalization with excessive increments in wall area. Hence, from a theoretical point of view both normalization of vascular lumen and normalization of wall thickness after balloon angioplasty can only be compatible with a regulation of both shear stress and wall stress (Figure 6).

As the integrity of the endothelial layer is interrupted directly after PTA, we propose that the immediate response of the vessel wall to balloon angioplasty be aimed at reducing the high wall stress by vessel wall growth. As a consequence, an increase of the minimal lumen area (MLA) from 12.4 to 18.4 as found in the present study, compensates wall stress with an additional increase of wall thickness of only 22% (according to Laplace). This increment in wall thickness is too small to compensate for the enlarged lumen area. Hence wall stress normalization will result in a blood vessel with increased wall thickness and an enlarged vessel lumen.

Endothelial regeneration during follow up allows shear stress regulation to become more important over time. The remaining large lumen area after wall stress normalization (see above) is accompanied by low shear stress regions.

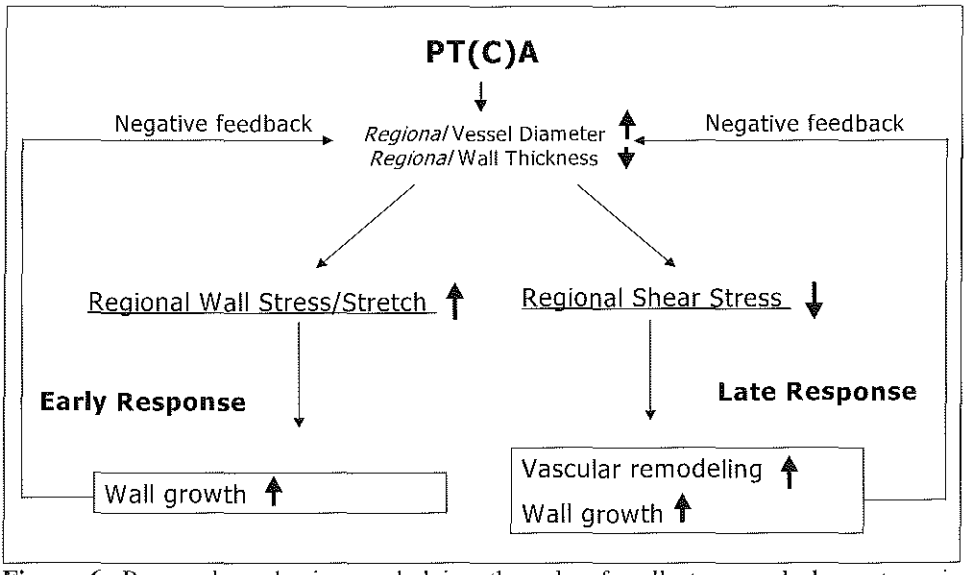

Figure 6: Proposed mechanism underlying the role of wall stress and shear stress in vascular remodeling after balloon angioplasty.

Due to the arrest of the atherogenic diet the newly formed endothelial cells that migrate into the balloon-dilated segment are relatively free of atherosclerosis. As a consequence, these endothelial cells trigger processes to increase shear stress and decrease vascular lumen towards the reference value during follow up.

Now, if due to shear stress regulation the vessel lumen diameter decreases, the wall stress decreases and active regulation of wall stress is induced which reduces wall thickness. The interplay between these processes settles down at a wall thickness and a lumen diameter close to reference segment values. As this process leads to reduction in vessel area it predicts vascular remodeling to be coupled to wall stress and shear stress regulation. Indeed, the present experiments showed that both PTA induced changes in wall stress and in shear stress are predictors of vascular remodeling, supporting the present theory.

The present analysis is closely coupled to two observations made in clinical research. Firstly, several parameters have already been identified that predict vascular remodeling, most of them based on geometrical parameters (Strauss *et al.*, 1991; Serruys *et al.*, 1991). As regional wall stress and regional shear stress incorporate these geometric factors the present findings are not in disagreement with these earlier studies. Secondly, an acute gain late loss relationship has been identified in several studies after PTA (Kuntz *et al.*, 1993). This relationship implies that the more that the geometry is changed after PTA, the larger the response. This finding is in full agreement with the existence of a wall stress and shear stress feedback mechanism.

7.5.4 Limitations of method

A major assumption of our 3-D reconstruction is that we might apply a straight pull back to reconstruct external iliac arteries. To test this assumption we performed a full 3-D reconstruction, applying a modification of the ANGUS-method (Slager *et al.*, 1997; Krams *et al.*, 1998; Krams *et al.*, 1997) on 5 out of the 10 arteries. The 3-D curvature was 7.14 m^{-1}. We have shown in a separate study that this curvature had negligible effect on the shear stress distribution (Chapter 5).

We applied a steady state, Newtonian fluid model in the present numerical analysis, while it is known that blood exerts non-Newtonian properties at low shear rate values and flow is pulsatile. In addition, the walls of the blood vessels are elastic. Several authors have shown that the combined effect of all these factors on average shear stress is relatively small in the shear rate range applied in the present study (Reuderink, 1991; Perktold *et al.*, 1994)

The 3-D reconstruction technique does not include studying side branches. We, therefore, excluded these regions in the present analysis. As these side branches immediately up and down stream of these regions might affect the local velocity field, the estimate of shear stress in those regions might be inaccurate.

We applied a regional 2-D thick walled cylindrical geometry to calculate wall stress in our blood vessels. As the external iliac arteries exhibited only small curvature, the 2-D assumption seems justified. However, tissue anisotropy and local spots of very high wall stress are not accounted for in the present study. This may lead to an underestimation of the role of average wall stress in vascular remodeling.

In conclusion, this is the first study evaluating the role of regional wall stress and regional shear stress in vascular remodeling induced by balloon angioplasty. Both shear stress and wall stress appear regulated with respect to their reference values at follow up. In addition, both wall stress and shear stress immediately after angioplasty are predictors of vascular remodeling. We propose that wall stress initiates the repair processes and remains active during the remodeling process, while shear stress regulation gains in importance with the regeneration of the endothelium. Shear stress normalization finally arrests the process.

Financial funding of ir. J.J. Wentzel by the Inter Cardiological Institute of The Netherlands (ICIN) is greatly acknowledged.

Ando, J., Tsuboi, H., Korenaga, R., Takada, Y., Toyama-Sorimachi, N., Miyasaka, M. and Kamiya, A. (1995) Down-regulation of vascular adhesion molecule-1 by fluid shear stress in cultured mouse endothelial cells. *Ann N Y Acad Sci* **748**, 148-56; discussion 156-7.

Bagshaw, R. J., Cox, R. H., Karreman, G. and Newswanger, J. (1986) Baroreceptor control of pressure-flow relationships during hypoxemia. *J. Appl. Physiol.* **60**, 166-175.

Bassiouny, H. S., Song, R. H., Hong, X. F., Singh, A., Kocharyan, H. and Glagov, S. (1998) Flow regulation of 72-kD collagenase IV (MMP-2) after experimental arterial injury. *Circulation* **98**, 157-63.

Bauters, C., Meurice, T., Hamon, M., McFadden, E., Lablanche, J. M. and Bertrand, M. E. (1996) Mechanisms and prevention of restenosis: from experimental models to clinical practice. *Cardiovasc Res* **31**, 835-46.

Bovendeerd, P., Steenhoven, A., van de Vosse, F. and Vossers, G. (1987) steady entrey flow in a curved pipe. *J. Fluid Mech.* **177**, 233-246.

Brownlee, R. D. and Langille, B. L. (1991) Arterial adaptations to altered blood flow. *Can J Physiol Pharmacol* **69**, 978-83.

Friesel, R. E. and Maciag, T. (1995) Molecular mechanisms of angiogenesis: fibroblast growth factor signal transduction. *Faseb J* **9**, 919-25.

Gere J.M. and Timoshenko S.P. (1996) Mechanics of Materials. pp. 801. Chapman and Hall, London.

Glagov, S. (1994) Intimal hyperplasia, vascular modeling, and the restenosis problem. [Review]. *Circulation* **89**, 2888-91.

Humphrey, J. D. (1995) Mechanics of the arterial wall: review and directions. *Crit Rev Biomed Eng* **23**, 1-162.

Kakuta, T., Usui, M., Coats Jr, W., Currier, J., Numano, F. and Faxon, D. (1998) Arterial remodeling at the reference site after angioplasty in the atherosclerotic rabbit model. *Arterioscler Thromb Vasc Biol* **18**, 47-51.

Kamiya, A. and Togawa, T. (1980) Adaptive regulation of wall shear stress to flow change in the canine carotid artery. *Am J Physiol* **239**, H14-21.

Krams, R., Wentzel, J., Oomen, J., Schuurbiers, J., Andhyswara, I., Kloet, J., Post, M., de Smet, B., Borst, C., Slager, C. and Serruys, P. (1998) Shear stress in atherosclerosis and vascular remodeling. *Semin. Interv. Cardiol.* **3**, 123-129.

Krams, R., Wentzel, J., Oomen, J., Vinke, R., Schuurbiers, J., de Feyter, P., Serruys, P. and Slager, C. (1997) Evaluation of endothelial shear stress and 3D geometry as factors determining the development of atherosclerosis and remodeling in human coronary arteries in vivo. Combining 3D

reconstruction from angiography and IVUS (ANGUS) with computational fluid dynamics. *Arterioscler Thromb Vasc Biol* **17**, 2061-5.

Ku, D. N., Giddens, D. P., Zarins, C. K., Glagov, S (1985) Pulsatile flow and atherosclerosis in the human carotid bifurcation. Positive correlation between plaque location and low oscillating shear stress. *Arteriosclerosis* **5**, 293-302.

Kuntz, R. E., Gibson, C. M., Nobuyoshi, M., Baim, D. S. (1993) Generalized model of restenosis after conventional balloon angioplasty, stenting and directional atherectomy. *J Am Coll Cardiol* **21**, 15-25.

Langille, B. L. (1993) Remodeling of developing and mature arteries: endothelium, smooth muscle, and matrix. [Review]. *J Cardiovasc Pharmacol* **21**, S11-7.

Li, W. (1997) Image and signal processing in intravascular ultrasound. *dissertation* Erasmus University Rotterdam.

Malek, A. and Izumo, S. (1992) physiological fluid shear causes downregulation of endothelin-1 mRNA in bovine aortic endothelium. *Am J Physiol* **263**, c389-c396.

Moore, J. E., Jr., Ku D. N., Zarins, C. K., Glagov, S. (1992) Pulsatile flow visualization in the abdominal aorta under differing physiologic conditions: implications for increased susceptibility to atherosclerosis [published erratum appears in J Biomech Eng 1993 Feb;115(1):12]. *J Biomech Eng.* **114**, 391-7

Nikol, S., Huehns, T. and Hofling, B. (1996) Molecular biology and post-angioplasty restenosis. *Atherosclerosis* **123**, 17-31.

Pasterkamp, G., Borst, C., Post, M. J., Mali, W. P., Wensing, P. J., Gussenhoven, E. J. and Hillen, B. (1996) Atherosclerotic arterial remodeling in the superficial femoral artery. Individual variation in local compensatory enlargement response. *Circulation* **93**, 1818-25.

Pasterkamp, G., Peters, R. J., Kok, W. E., Van Leeuwen, T. G. and Borst, C. (1997) Arterial remodeling after balloon angioplasty of the coronary artery: an intravascular ultrasound study. PICTURE Investigators. PostTreatment IntraCoronary Transluminal Ultrasound Result Evaluation. *Am Heart J* **134**, 680-4.

Pasterkamp, G., Wensing, P. J., Post, M. J., Hillen, B., Mali, W. P. and Borst, C. (1995) Paradoxical arterial wall shrinkage may contribute to luminal narrowing of human atherosclerotic femoral arteries. *Circulation* **91**, 1444-9.

Perktold, K., Thurner, E. and Kenner, T. (1994) Flow and stress characteristics in rigid walled and compliant carotid artery bifurcation models. *Med Biol Eng Comput* **32**, 19-26.

Post, M. J., Borst, C. and Kuntz, R. E. (1994) The relative importance of arterial remodeling compared with intimal hyperplasia in lumen renarrowing after balloon angioplasty. A study in the normal rabbit and the

hypercholesterolemic Yucatan micropig [see comments]. *Circulation* **89**, 2816-21.

Post, M. J., de Smet, B. J. G. L., van der Helm, Y., Borst, C. and Kuntz, R. E. (1997) Arterial remodeling after balloon angioplasty or stenting in an atherosclerotic experimental model. *Circulation* **96**, 996-1003.

Rachev, A., Stergiopulos, N. and Meister, J. J. (1998) A model for geometric and mechanical adaptation of arteries to sustained hypertension. *J Biomech Eng* **120**, 9-17.

Reuderink, P. (1991) Analysis of the flow in a 3D distensible model of the carotid artery bifurcation. *Thesis Eindhoven* wibro dissertatiedrukkerij, Helmond, ISBN 90-9004413-2.

Sabbah, H. N., Khaja, F., Brymer, J. F., Hawkins, E. T., Stein, P. D (1984). Blood velocity in the right coronary artery: relation to the distribution of atherosclerotic lesions. *Am J Cardiol* **53**, 1008-12.

Serruys, P. W., Strauss, B. H., Beatt, K. J., Bertrand, M. E., Puel, J., Rickards, A. F., Meier, B., Goy, J. J., Vogt, P., Kappenberger, L. and et al. (1991) Angiographic follow-up after placement of a self-expanding coronary-artery stent [see comments]. *N Engl J Med* **324**, 13-7.

Sharefkin, J. B., Diamond, S. L., Eskin, S. G., Mcintire, L. V. and Dieffenbach, C. W. (1991) fluid flow decreases preproendothelin mRNA levels and suppresses endothelin-1 peptide relares in cultered human endothelial cells. *J. Vasc. Surg.* **14**, 1-9.

Slager, C., Wentzel, J., Oomen, J., Schuurbiers, J., Krams, R., von Birgelen, C., Tjon, A., Serruys, P. and de Feyter, P. (1997) True reconstruction of vessel geometry from combined X-ray angiographic and intracoronary ultrasound data. *Semin Intervent Cardiol* **2**, 43-47.

Strauss, B. H., Serruys, P. W., de Scheerder, I. K., Tijssen, J. G., Bertrand, M. E., Puel, J., Meier, B., Kaufmann, U., Stauffer, J. C., Rickards, A. F. and et al. (1991) Relative risk analysis of angiographic predictors of restenosis within the coronary Wallstent. *Circulation* **84**, 1636-43.

Taylor, W. R. (1998) Mechanical deformation of the arterial wall in hypertension: a mechanism for vascular pathology. *Am J Med Sci* **316**, 156-61.

Thubrikar, M. J. and Robicsek, F. (1995) Pressure-induced arterial wall stress and atherosclerosis. *Ann Thorac Surg* **59**, 1594-603.

Vosse, v. d. F. N., Steenhoven, v. A. A., Segal, A. and Janssen, J. D. (1989) A finite element analysis of the steady laminar entrance flow in a 90 curved tube. *International Journal for Numerical Methods in Fluids* **9**, 275-287.

Williams, B. (1998) Mechanical influences on vascular smooth muscle cell function. *J Hypertens* **16**, 1921-9.

Reduction in Constrictive Vascular Remodeling after PTA by Batimastat is Accompanied by Hampered Normalization of Wall Stress and Shear Stress

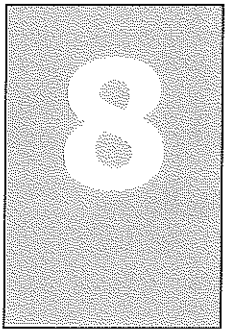

JJ Wentzel, J Kloet, I Andhyiswara, JA Oomen, JCH Schuurbiers, BJGL de Smet, D de Kleijn, G Pasterkamp, C Borst, CJ Slager, R Krams

Chapter 8, PTA in iliac artery

Background
It has been shown that vascular remodeling (VR) after percutaneous transluminal balloon angioplasty (PTA) is regulated by shear stress (SS) and wall stress (WS) and is inhibited by blockade of the metalloproteinases. The aim of the present study is to investigate whether SS and WS regulation is still intact or is inhibited after PTA by administration of a MMP-inhibitor.

Methods
In the iliaca externa of 12 atherosclerotic Yucatan pigs PTA was performed. 6 pigs received Batimastat and 6 pigs served as Control. Before, after intervention and at 6 weeks follow up intravascular ultrasound pullback was performed allowing 3-D reconstruction of these arteries. Subsequently, these 3-D reconstructions were used to calculate SS by computational fluid dynamics (flow: 80 ml/sec) and WS applying a thick wall cylinder model. After smoothing, aligning and resampling of these arteries, VR was related to SS and WS after PTA. Regulation was defined as the condition that SS and WS at the balloon dilated segment were equal to the SS and WS at the vessel segment outside the balloon dilated segment (reference segment) at follow up.

Results
Batimastat reduced the contribution of VR to the change in lumen area during follow up. However, the change in loss index induced by Batimastat versus control was not significant (1.02±0.11 vs. 0.81±0.05, p=0.087). For both groups, VR was predicted by both SS and WS, however the relative contribution of SS and WS was changed by Batimastat. For the Control group, at follow up SS and WS in the balloon segment were closely returned to the reference segment, while for the Batimastat group both the SS and the WS were in general below the reference values ($p<0.05$).

Conclusion
Batimastat reduces the vascular remodeling thereby hampering the shear stress and the wall stress control system 6 weeks after PTA.

Although balloon angioplasty (PTA) is a well accepted method to reduce arterial stenosis, an important disadvantage is that in 30-50% of the cases restenosis develops. Tissue injury related intimal hyperplasia has long been proposed as the main cause of restenosis (Nobuyoshi *et al.*, 1991). Recently, however, it became clear that restenosis after balloon angioplasty is mainly caused by shrinkage of the vessel wall ('constrictive vascular remodeling') and only to a minor extent by neointimal formation (Post *et al.*, 1994).

Constrictive vascular remodeling has been measured as a response to conditions of low shear stress, where it is aimed at restoring the original shear stress (Kamiya and Togawa, 1980). In addition, vascular remodeling has been observed in hypertension studies and the vessel wall presumably adapts to normalize the induced changes in wall stress (Bevan *et al.*, 1975; Rachev *et al.*, 1998; Wolinsky, 1970).

Recently, we showed that constrictive and expansive vascular remodeling induced by balloon angioplasty could be interpreted as a response to control both the shear stress and wall stress such that they became equal to the reference segments (Chapter 7). This study, therefore, implied that two negative feedback loops underly vascular remodeling. Hence, in order to prevent the artery from remodeling after PTA and keep the vascular lumen patent, these negative feedback loops should be studied and if possible inhibited.

In a previous study, de Smet *et al.* showed a reduction in vascular remodeling after PTA by inhibition of Matrix Metalloproteinase (de Smet, 1998) (MMP inhibition). MMP inhibition reduces the break down of extra cellular matrix and thereby the migration of smooth muscle cells (Bendeck *et al.*, 1996). Since the expression of MMP mRNA is coupled to both the shear stress and wall stress changes (Bassiouny *et al.*, 1998; Rohde *et al.*, 1999), we hypothesized that a pharmacological MMP-inhibition is a method to inhibit the negative feedback loops that controls the shear stress and wall stress. Through this intervention negative vascular remodeling after PTA may be inhibited.

To that end we calculated the shear stress and wall stress distributions with a newly developed technique before and after PTA and at 6 weeks follow up in the atherosclerotic Yucatan pig; a well accepted animal model for atherosclerosis (Post *et al.*, 1997). In the present study a detailed analysis is performed on a group of animals receiving a MMP-inhibitor. The Control group (6 Yucatan pigs) has been described in Chapter 7 in detail.

8.2.1 General protocol

In a former study the effect of wall stress and shear stress was evaluated in a group of pigs not receiving Batimastat (Chapter 7). Details of this Control group will be presented in relevance to the present study. 6 Yucatan mini-pigs with a final weight of 25 kg were used for this study. At the age of 7 months the animals started an atherogenic diet. Two weeks thereafter they underwent Fogarty denudation of the external iliac arteries and after an additional 4 months of diet the arteries were treated by balloon angioplasty (PTA). From that moment on the atherogenic diet was replaced by a regular diet and a matrix metalloproteinase inhibitor (Batimastat, supplied by British Biotech Pharmaceutical Limited, Oxford, U.K.) was administered and repeated at a two weeks interval. On the day of termination, six weeks after balloon angioplasty the animals were studied again. All animals were treated according to the Guide for the Care and Use of laboratory Animals published by the US National Institutes of Health (NIH Publication No. 85-23, revised 1985) and treatment was approved by the ethical committee on Animal Experiments of the Faculty of Medicine, Utrecht University.

8.2.2 Atherogenic diet

In addition to essential nutrients, vitamins and salts, 1.5% cholesterol, 17.5% casein, 14% lard, and 6% peanut oil formed the basic atherogenic components of the diet that had a daily nutritional value equivalent to 2400 Kcal. In pilot experiments, it was shown that this regimen results in a sustained 10-fold increase in total cholesterol reaching a level of 14.9±4.4 mmol/l, and approximately a 3.5-fold increase in HDL reaching a level of 2.2±0.3 mmol/l. Water intake was not restricted. The diet during follow up was a regular, non-atherogenic chow with a nutritional value equal to the atherogenic diet.

8.2.3 Catheterization protocol and anesthesia

Before all interventions, the animals were anesthetized with intravenous metomidate (4 mg/kg) and ventilated (Servo, EM 902) with a mixture of O_2:N_2O=1:2 and halothane, 1-2%.

For all interventions, the arterial tree was accessed through an excision of the carotid artery and an 8F sheath was positioned into the aortic bifurcation under fluoroscopic guidance. Through this sheath, contrast (Telebrix, Laboratoire Guerbet, France) was injected and angiography was performed using a fluoroscopic unit (Philips, Eindhoven, The Netherlands). The image with the highest contrast was selected and recorded on DAT tape for further analysis.

Two weeks after the start of the artherogenic diet, a 4F Fogarty catheter was introduced into the right or left external iliac artery and segments of 3-4 cm (measured by a radiopaque ruler) were denuded by triple withdrawal of the manually inflated Fogarty balloon with a 50/50 v/v water contrast mixture. Thereafter, the carotid artery was sutured and the pigs were allowed to recover. After an additional 4 weeks, the most prominent site of arterial narrowing was selected from the angiographic images in both the right and left external iliac arteries as target area for balloon angioplasty (PTA). Before PTA, intravascular ultrasound (IVUS) using 2.9 and 4.3 F catheters (30 MHz; Du-MED, Rotterdam, the Netherlands) was used to investigate the target area (protocol see below). Using the IVUS derived vessel diameter, an angioplasty balloon (standard peripheral balloon: length 4-5 cm, diameter 6-7 mm) was selected to induce a dilatation ratio of 1.2. The balloon was inflated 3 times for 1 min at a pressure of 10 atmosphere, which was documented by fluoroscopy. After PTA, the IVUS catheter was reintroduced and a continuous pull back as described below was performed.

After 6 weeks follow up, the pigs were anesthetized again and angiography and IVUS as described elsewhere documented the treated area. Thereafter, the animals were terminated.

8.2.4 Drugs

One day before PTA, acetyl salicylic acid (125 mg) was given and continued for 2 weeks after the intervention. During PTA and at the day of termination, a continuous infusion of nitroglycerin (20 µg/min) was given to prevent arterial spasm. During each procedure, heparin was administered (thromboliquine (100 IU/kg), Organon Technika) to each animal. Every 15 min, 0.25 mg Atropine was given intravenously.

After PTA 6 animals were given BB-94 (Batimastat British Biotech Pharmaceuticals Limited, Oxford, U.K.), 64 mg/kg i.p. in a concentration of 20 mg/ml. Batimastat, is a nonspecific synthetic MMP-inhibitor directed against MMP-1, MMP-2, MMP-3, MMP-8 and MMP-9 matrilysin. This injection was repeated at two and at four weeks after PTA. The other 6 animals served as Control.

8.2.5 Intravascular Ultrasound protocol

Before, immediately after PTA and after 6 weeks follow up, the IVUS-catheter was placed at a side branch distal from the target area and a continuous pull back was started from the distal side branch to the start of the guiding catheter. In order to allow a 3-D reconstruction of the IVUS-data, a pull back distance measurement device was connected to the IVUS catheter and the IVUS images combined with the distance data were recorded on S-VHS videotape. To relocate the target area at different time points (before and after PTA and at follow up), the position of

the distal side branch was documented with the help of a radiopaque ruler that was placed parallel to the spine in a reproducible manner (de Smet *et al.*, 1997).

8.2.6 3-D reconstruction

3-D reconstruction of the right and left iliac arteries before and after PTA and at follow up was performed as follows. Firstly, the IVUS images were digitized from the videotape with a resolution of 800 x 600 pixels at intervals of 0.5 mm and stored in a computer. Lumen and media were traced semi-automatically by a well validated computer package (Li, 1997). The resulting lumen and media contours were serially positioned perpendicular to the IVUS catheter axis at intervals of 0.5 mm. After resampling and fitting a surface (Matlab®, Mathworks Inc., Mass, USA) through the lumen and media contours, a 3-D reconstruction of the lumen and wall of the iliac arteries was obtained.

8.2.7 Computational fluid dynamics

Mesh generation

The lumen of the reconstructed artery was filled by 3-D finite elements in order to calculate a 3-D flow-velocity field using a finite element software package (Sepran, Sepra, Leiden, the Netherlands). In the axial direction maximally 100 elements could be applied which slightly reduced the axial mesh resolution from 0.5 mm (IVUS method) to 0.75±0.11 mm in the mesh. Each cross section consisted of 32 elements and each element contained 27 nodes. This results in a cross sectional resolution of 220 μm to 450 μm for the largest diameter and of 90 to 190 μm for the smallest diameter. The range was a result of a purposely-induced increase in resolution towards the vessel wall.

Boundary conditions and assumptions

In order to solve the 3-D-Navier-Stokes equations it is necessary to supply, besides the mesh, boundary conditions, properties of the fluid and method of solution. We assumed that blood behaves as a Newtonian fluid with a viscosity of 3 cP and a density of 1050 kg/m^3. At the entrance a parabolic velocity profile was applied with a flow of 80 ml/min (Bagshaw *et al.*, 1986). At the wall no-slip conditions and at the exit zero stress conditions were assumed. The solution method consisted of a linearization of the non-linear convective terms by a Newton-Raphson approach, while the matrix was solved by a direct profile method.

8.2.8 Matching wall and lumen of the iliac arteries before, after PTA and at follow up

The media bounded area obtained from the IVUS contours was processed similar to the lumen to obtain a 1 to 1 matching of lumen and wall with the resolution of the mesh data. In this way a direct coupling between vascular remodeling, wall stress and shear stress is realized.

Furthermore, each set of iliac arteries (before, after PTA and at follow up), was processed to enable comparison of similar locations of each artery at each time point. This processing consisted of selecting the previous selected side branch as the distal common end point. The shortest pull back of all three pull back's determined the length of each reconstruction at the three different time points. Differences in spatial resolution were adjusted for by a linear interpolation routine written in Matlab. The location of the balloon dilated segment was selected from the angiographic data and linearly extrapolated to the mesh data, using the same side branches as a landmark.

8.2.9 Analysis

From the matched contours we derived lumen area (LA), wall area (WA) and media bounded area (MBA) by numerical integration. Multiplying the shear rate with the constant viscosity delivered the shear stress (SS, Table 1). The shear stress was averaged for each cross section, because the rotational orientation of the arteries at each time point could not be determined. Wall stress (WS, Table 1) was derived, based on a thick wall cylindrical model, thereby assuming each cross section as a circle. This approach resulted in an average wall stress per cross section.

Since, systemic factors could affect our data, we defined relative parameters. These normalized parameters were calculated by dividing each above mentioned parameter by its corresponding value in the non-dilated reference segment (nLA, nWA, nMBA, nSS, nWS; Table 1). The reference segments were defined as the average of the cross sections outside the balloon dilated segment. Since, arterial spasm might influence the reference segments after PTA, the reference segment before PTA was used to calculate relative values for the parameters immediately after PTA.

Regulation of the shear stress and wall stress in the follow-up period was defined as the process of restoring the shear stress or wall stress with respect to the non-dilated segment at follow up.

Table 1: Definition of the applied parameters

	Formula	Description
	Geometrical parameters	
MLA		Minimal lumen area pre
LA		Lumen area
MBA		Media bounded area
WA	MBA-LA	Wall area
nLA	LA/LA_{ref}	Lumen area normalized by lumen area at the reference segment
nMBA	MBA/MBA_{ref}	Media bounded area normalized by media bounded area at the reference segment
nWA	WA/WA_{ref}	Wall area normalized by wall area at the reference segment
ΔLA_{fupost}	LA_{fu}- LA_{post}	Change in lumen area in the follow up period
ΔMBA_{fupost}	MBA_{fu}- MBA_{post}	Change in MBA in the follow up period
ΔWA_{fupost}	WA_{fu}- WA_{post}	Change in WA in the follow up period
ΔnLA_{fupost}	$(nLA_{fu}-nLA_{post})*100\%$	Change in normalized lumen area in the follow up period *(lumen change)*
$\Delta nMBA_{fupost}$	$(nMBA_{fu}-nMBA_{post})*100\%$	Change in normalized MBA in the follow up period *(vascular remodeling)*
ΔnWA_{fupost}	$(nWA_{fu}-nWA_{post})*100\%$	Change in normalized wall area in the follow up period *(vessel wall growth)*
Acute lumen gain	$LA_{post}-LA_{pre}$	Change in lumen area due to balloon angioplasty
Late lumen loss	$LA_{post}-LA_{fu}$	Change in lumen area
	Biophysical parameters	
SS		Shear stress
nSS	SS/SS_{ref}	Normalized shear stress
ΔnSS_{furef}	$(nSS_{fu}-1)*100\%$	Shear stress normalization with ref at follow up
WS		Wall stress
nWS	WS/WS_{ref}	Normalized wall stress
ΔnWS_{furef}	$(nWS_{fu}-1)*100\%$	Wall stress normalization with ref at follow up

pre: before balloon angioplasty; post : after balloon angioplasty; fu: at follow up; ref: reference segment

In our analysis only data of the balloon-dilated segments were used. In addition 12.5% at each end was stripped off to reduce the influence of uncertainties in balloon location. If side branches were present within the balloon dilated segment, cross sections at the side branch and adjacent cross sections up to a distance equal to the side branch diameter were excluded from the analysis. This reduction of the data set was introduced to account for undetermined influences of the side branches on the wall stress and shear stress distribution.

To minimize the effect of spasm after balloon angioplasty we included only the cross sections with a positive acute lumen gain.

For comparison of the MLA, MBA, WA, SS, WS and their normalized values and at different time points a repeated measures ANOVA was applied, followed by the Student-Newman-Keuls test for multiple comparisons. The Batimastat group and the Control group were compared by two way ANOVA.

The contribution of vascular remodeling (ΔMBA_{fupost}) to changes in lumen area (ΔLU_{fupost}) and the relationship between acute lumen gain and late lumen loss was studied applying linear regression analysis. The loss index was derived from the slope of the regression line obtained from the relationship between acute lumen gain and late lumen loss (Table 1). In order to detect differences between the Control group and the Batimastat group two sets of dummies were added for detection of differences in offset and slope.

The normalized biophysical parameters predicting vascular remodeling and the vessel wall growth (Table 1) after PTA were determined by multivariate regression analysis in a two step approach. Firstly, a univariate analysis was performed with nSS_{post} and nWS_{post}. If a parameter became significant, it was incorporated into a multi-regression model. For the above mentioned regression analysis the data were pooled, thereby coding the individual pigs with two types of dummies. One dummy corrected for an offset per animal and one dummy corrected for differences in slope per animal. An F-test was applied to each set of dummies to test if addition of the dummies reduced the unexplained variance of the model.

Shear stress and wall stress normalization were studied in relation to acute lumen gain. In order to do so, the data set was divided into three groups based on acute lumen gain. The borders of the groups were determined such that the acute lumen gain obtained for the Control group was equally distributed over the three groups. The average $n\Delta SS_{furef}$ and $n\Delta WS_{furef}$ was calculated, correcting for multiple measurements per pig by applying dummies (Glantz and Slinker, 1990). Normalization of these parameters was defined as the absence of a statistical difference with zero applying t-tests. As side branches in between the balloon dilated segment and the reference segment artificially affected the reference value of shear stress and wall stress, we excluded these conditions from the present analysis. Furthermore, for the remaining vessels the reference segment was chosen such that only the vessel segments adjacent to the balloon segment up to the next side branch were included.

Finally, for the remaining comparisons t-tests were applied where appropriate. All values are expressed as mean ± SD. The statistically package SPSS 9.0 (SPSS Inc. Chicago, Illinois, USA) was used for all calculations.

8.4.1 Animals

We studied the right and left iliac artery of 12 pigs, resulting in 24 arteries. 6 pigs received Batimastat, while the remaining 6 pigs served as the Control group. The Control group contained 10 arteries (30 3-D reconstruction's), since one artery was lost due to technical failure and in one artery no balloon was inflated. For the Batimastat group, one pig died during the follow up period and in 2 arteries no balloon was inflated. One 3-D reconstruction failed due to technical failure and since the analyses combines 3 complete 3-D reconstructions for each artery (before, after balloon angioplasty and at follow up) the Batimastat group includes 7 arteries (21 3-D reconstructions).

Selection of the balloon segment and stripping of 12.5% at each end resulted in 407 and 262 data points for the Control group and the Batimastat group respectively. Subsequently, after selection of the segments with positive acute lumen gain, 222 and 109 data points were included in the data set for the Control group and Batimastat group. Finally, in order to study the normalization of shear stress and wall stress, for which side branches could artificially affect the data, vessel segments containing side branches in between the balloon and the reference segment were excluded, resulting in 218 and 87 data points for the Control group and the Batimastat group, respectively.

8.4.2 Geometrical parameters

No differences in lumen area, media bounded area and wall area between the Control group and the Batimastat group could be observed at the location of MLA. However, statistical significant differences existed between the variables at the different time points (Table 2, and Table 3; two-way ANOVA).

Table 2: Geometrical and biophysical parameters within the balloon dilated segment and located at MLA calculated from 3-D reconstructions of iliac arteries of atherosclerotic Yucatan pigs receiving either placebo (10 vessels) or Batimastat (7 vessels).

	Control			*Batimastat*		
	Pre	Post	Fu	Pre	Post	Fu
MLA (mm^2)	12.4±3.2	18.4±3.9*	12.2±2.2^{+}	11.3±3.7	16.6±5.7*	11.8±3.1^{+}
MBA (mm^2)	18.0±4.5	23.8±3.9*	17.4±2.6^{+}	15.1±3.6	22.3±7.9*	18.1±4.8
Wall area (mm^2)	5.6±1.8	5.4±1.2	5.2±1.2	3.8±1.0	5.8±3.2*	6.3±3.1$^{\#}$
Shear stress (N/m^2)	0.9±0.4	0.3±0.2*	0.9±0.4^{+}	1.1±0.5	0.5±0.4*	0.9±0.5
Wall stress (kN/m^2)	69±18	100±27*	70±17^{+}	91±40	97±48	68±36$^{\#+}$

Pre: before balloon angioplasty, Post: after balloon angioplasty, Fu: follow up, MLA: minimal lumen area, MBA: media bounded area, * $p<0.05$, pre vs post; $^{+}$: $p<0.05$,post vs follow up; $^{\#}$:$p<0.05$, pre vs follow up

Table 3: Geometrical and biophysical parameters within the balloon dilated segment and located at MLA calculated from 3-D reconstructions of iliac arteries of atherosclerotic Yucatan pigs receiving either placebo (10 vessels) or Batimastat (7 vessels).

	Control			*Batimastat*		
	Pre	Post	Fu	Pre	Post	Fu
nMLA	0.8±0.3	1.1±0.4*	1.1±0.3$^{\#}$	0.7±0.2	1.2±0.5*	0.9±0.4
nMBA	0.8±0.3	1.1±0.3*	1.1±0.2	0.8±0.1	1.2±0.5*	1.1±0.4
nWA	1.1±0.4	1.1±0.4	1.1±0.3	0.9±0.2	1.4±0.5*	1.5±0.5$^{\#}$
nSS	1.9±0.8	0.6±0.5*	1.0±0.4$^{\#}$	2.0±1.0	1.1±1.3*	1.4±1.0$^{\#}$
nWS	0.8±0.3	1.1±0.4*	1.1±0.3$^{\#}$	0.8±0.2	0.9±0.3	0.6±0.2$^{\#+}$

Pre: before balloon angioplasty, Post: after balloon angioplasty, Fu: follow up, MLA: minimal lumen area, MBA: media bounded area, *: $p<0.05$, pre vs post; $^{+}$: $p<0.05$,post vs follow up; $^{\#}$:$p<0.05$, pre vs follow up

Nonetheless, Batimastat influenced the change in the lumen area and MBA at the reference segment ($p<0.05$, Table 4). Only for the control group significant shrinkage in LA and MBA was observed ($p<0.05$, Table 4).

In contrast to this single point analysis, regression analysis on all data points revealed that the slope and intercept of the relationships between Lumen Area and Media Bounded Area during follow up were different for the Control group (MBA_{fu}= 1.00*LU_{fu}+5.11; Figure 1B) and for the Batimastat group (MBA_{fu}= 2.10*LU_{fu} –5.6; Figure 1B). Before angioplasty they were not different (Control: MBA_{pre} = 1.5*LU_{pre}-1.5; Batimastat: MBA_{pre}=1.35*LU_{pre}-0.33; Figure 1A). As a consequence, Batimastat reduced the contribution of vascular remodeling to lumen decrement in the follow up period (Control: ΔMBA_{fupost} = 1.27*ΔLU_{fupost}+1.36, Batimastat: ΔMBA_{fupost} =0.56*ΔLU_{fupost} –1.43 ,$p<0.05$, Figure 1C).

The relationships between Wall Area and Lumen Area before angioplasty were not different (Control: WA_{pre} = 1.50*LU_{pre}-1.51; Batimastat: WA_{pre} = 1.35*LU_{pre} –0.33; Figure 2A), while they were different at follow up (Control: WA_{fu} = 0.001*LU_{fu}+5.1; Batimastat: WA_{fu} = 1.1*LU_{fu}-5.6; Figure 2B). As a consequence, the degree of wall growth to lumen change alterated dramatically (Control: ΔWA_{fupost} = 0.28*ΔLU_{fupost} +1.35; Batimastat: ΔWA_{fupost} = -0.44 *ΔLU_{fupost} –1.43; $p<0.05$, Figure 2C). Administration of Batimastat tended to reduce the loss index by 21% (Control: 1.02±0.11, Batimastat: 0.81±0.05, p=0.087).

8.4.3 Biophysical parameters

No differences in shear stress between the Control group and the Batimastat group could be observed at the location of MLA, however statistical significant

Table 4: Geometrical and biophysical parameters at the *reference* of iliac arteries of atherosclerotic Yucatan pigs receiving either placebo (10 vessels) or Batimastat (7 vessels).

	Control			*Batimastat*		
	Pre	Fu	Fu-Pre	Pre	Fu	Fu-Pre
LA (mm^2)	17.3±5.1	12.4±4.5*	-4.9±3.5	15.6±4.2	14.5±5.6	-1.2±1.8#
MBA (mm^2)	22.7±6.1	17.8±5.3*	-4.9±3.9	19.9±5.1	18.5±6.8	-1.4±2.1#
WA (mm^2)	5.4±1.4	5.4±1.3	0±0.9	4.2±1.3	4.0±1.4	-0.2±0.5
SS (N/m^2)	0.6±0.3	1.0±0.8*	0.5±0.6	0.6±0.2	0.9±0.5	0.3±0.3
WS (kN/m^2)	95±21	69±22*	-26±13	108±22	106±20#	-3±12#

Pre: before balloon angioplasty, Fu: follow up, MBA: media bounded area, Fu-pre: change during follow up period # $p<0.05$: Batimastat vs Control; * $p<0.05$: pre vs Fu

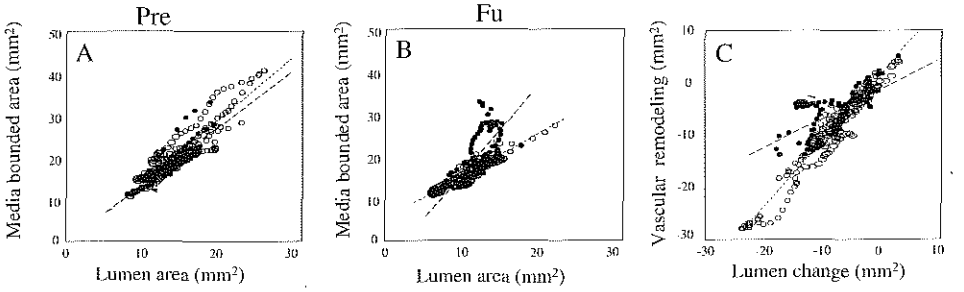

Figure 1: The relationship between media bounded area and lumen area before (Pre) angioplasty and at 6 weeks follow up (Fu) for the Control group (o, ..) and the Batimastat group (•,--). A) Media bounded area vs. Lumen area before angioplasty B) Media bounded area vs. Lumen area at follow up C) Vascular remodeling vs. Lumen change during 6 weeks follow up.

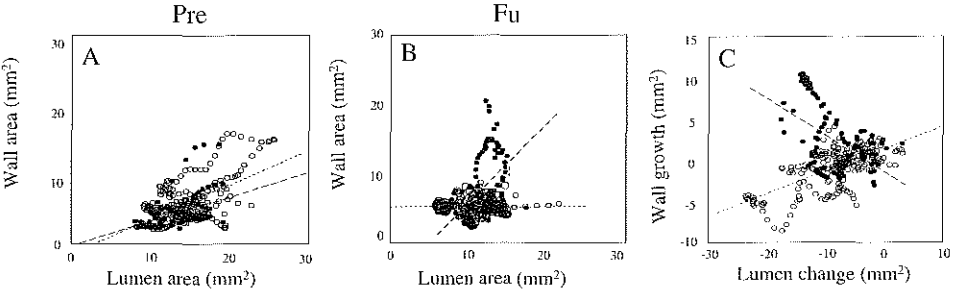

Figure 2: The relationship between wall area and lumen area before (Pre) angioplasty and at 6 weeks follow up (Fu) for the Control group (o,..) and the Batimastat group (•,--). A) Wall area vs. lumen area before angioplasty B) Wall area vs. lumen area at follow up C) Wall area growth vs. lumen change during 6 weeks follow up.

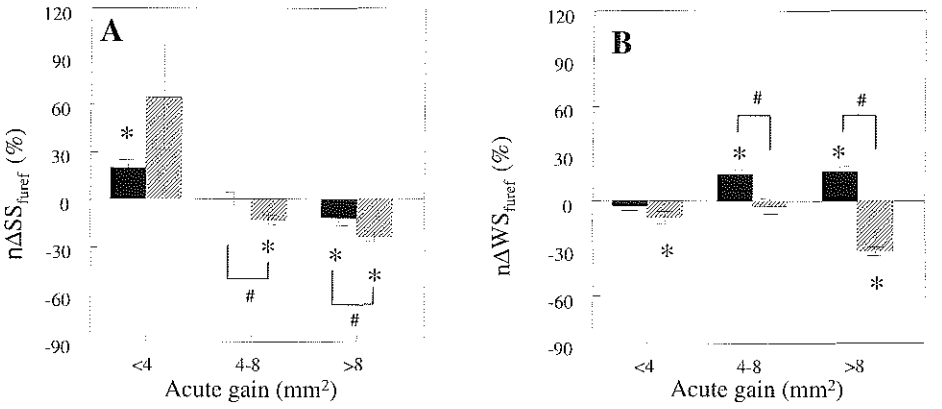

Figure 3: Normalization of shear stress (A) and wall stress (B) for the Batimastat group (dashed) and the Control group. related to the acute gain. *: $p<0.05$, value vs. 0; #: $p<0.05$, Batimastat vs. Control group, Errorbars: SEM

differences existed between the variables at the different time points (Table 2, and Table 3; two-way ANOVA). Thus, balloon angioplasty decreased both the SS and nSS to approximately 50% of baseline values for both groups (Table 2). At follow up, the shear stress returned to baseline values for both the Control and the Batimastat group.

Observing the reference segments, the wall stress at follow up was 52% higher after administration of Batimastat than the control group, caused by a lower change (90%) during the follow up period (Table 4). Consequently only the control group showed significant changes in wall stress during the follow up period ($p<0.05$, Tabel 4). Furthermore, a change in shear stress during the follow up period was observed for the control group, which was not statistically different from the Batimastat group.

Analysis revealed that for both groups the normalization of shear stress was inversely related to the acute lumen gain (Figure 3A). However, for the Batimastat group for acute lumen gain < $4mm^2$ the $n\Delta SS_{furef}$ did not become significantly different from zero ($p=0.07$). Normalization of shear stress was for the Control group observed for intermediate acute lumen gain (4-$8mm^2$) ($p=0.99$). The Batimastat group was statistically different from the Control group for acute lumen gains exceeding 4 mm^2 ($p<0.05$).

No differences in wall stress between the Control group and the Batimastat group could be observed at the location of MLA, however statistical significant differences existed between the variables at the different time points (Table 2, and Table 3; two-way ANOVA). Wall stress for the Control group increased by

balloon angioplasty by 43% and decreased to values equal to the reference segment at follow up. In contrast to the Control group, wall stress in the Batimastat group was not significantly raised by balloon angioplasty (Table 2), but decreased during follow up to 70% of the baseline values ($p<0.05$). Considering all data points, for the Batimastat group the wall stress was generally not normalized (Figure 3B), except for intermediate acute lumen gain value ($p=0.56$) and was lower than the value of the reference segment. In contrast, for the Control group the wall stress was generally higher than the reference values ($p<0.05$). The wall stress for the Control group was statistically different from the Batimastat group for an acute lumen gain exceeding 4 mm^2 ($p<0.05$).

8.4.4 Correlation between geometrical factors and biophysical factors

For both groups, the univariate analysis revealed that vascular remodeling (Table 1) was related to both nWS_{post} and nSS_{post} (Table 5). The multivariate models disclosed that both parameters were significant independent predictors for vascular remodeling for the Control group ($\Delta nMBA_{fupost}$ = (20±11)+ (33± 12)*nSS_{post} – (34±7)*nWS_{post}, $r^2=0.90$, $p<0.05$) and for the Batimastat group ($\Delta nMBA_{fupost}$ = (-72±14)+ (22±6)*nSS_{post} +(43±12)*nWS_{post} $r^2=0.39$, $p<0.05$).

Figure 4A shows the relationship between vascular remodeling and nSS_{post} for both the Control group and the Batimastat group for nWS_{post} being equal to the average value. Batimastat tended to rotate the relationship between shear stress and vascular remodeling as derived from the slopes in the multivariate model, but this change was not significant (Control: slope: 33±12; Batimastat: slope: 22±6; t-test, p=NS; Figure 4A) More important, the inverse relationship between wall stress and vascular remodeling observed for the Control group was reversed after administration of Batimastat (Control: slope: -34±7; Batimastat: slope: 43±12, $p<0.05$; Figure 4B).

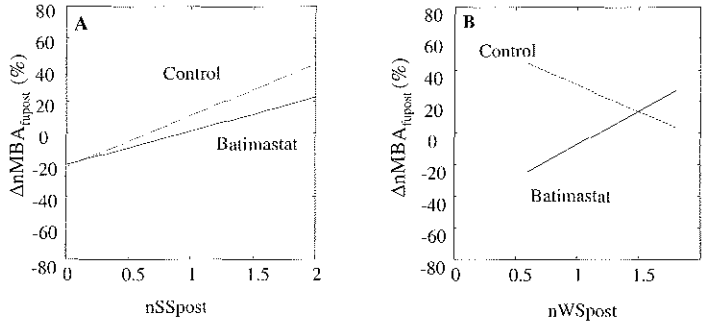

Figure 4: Vascular remodeling related to the normalized shear stress (A) and to the normalized wall stress (B) after balloon angioplasty for the Control group (--) and the Batimastat group (-) derived from the multivariate prediction model.

Table 5: Univariate regression analysis of the relationship between normalized shear stress and normalized wall stress and vascular remodeling and vessel wall growth in the external iliac arteries of atherosclerotic Yucatan Pigs.

Parameter	Vascular remodeling (%)			
	Control group		*Batimastat group*	
	slope	p values	slope	p value
nSSpost	48±12	<0.001	16±6	0.008
nWSpost	-66±7	<0.001	33±12	0.007
	Vessel wall growth (%)			
	slope	p values	slope	p value
nSSpost	20±18	0.271	-53±21	0.012
nWSpost	53±33	0.103	124±49	0.013

nSSpost (nWSpost) shear stress (wall stress) post balloon angioplasty normalized to the reference segment

Consequently, administration of Batimastat changed the relative contribution of shear stress to vascular remodeling (Control:0.6, Batimastat: 0.4) and wall stress (Control: 0.4, Batimastat: 0.6). Vessel wall growth (ΔnWA_{fupost}) for the Batimastat group was related to both nWS_{post} and nSS_{post} (Table 5), however the multivariate model showed that nWS_{post} was the only predictor of vessel wall growth ($\Delta nWA_{fupost} = (133.0\pm50.9)*nWS_{post}$, $r^2=0.53$, $p<0.05$). In contrast, in the Control group no predictor for vessel wall growth was found (Table 4: univariate analysis).

Since restenosis is still an important draw back of the successful application of PTA and since constrictive vascular remodeling has been shown to be a major component of restenosis, the MMP-inhibitor Batimastat was introduced to prevent the artery from constrictive vascular remodeling. In Chapter 7, we have shown that remodeling after balloon angioplasty in the atherosclerotic Yucatan pig is accompanied by shear stress and wall stress normalization. Data of this study served in the current study as a control to evaluate the effect of Batimastat on the shear stress and wall stress control mechanisms. We will first focus on the geometrical factors and finally on the control mechanisms.

8.5.1 Geometrical factors

As became apparent from studying the reference segment during follow up, some systemic change occurred, possibly induced by finishing the atherosclerotic diet, which led to constrictive remodeling of the reference segment. Batimastat clearly abolished this constrictive remodeling effect (Table 4).

As expected from a previous study (de Smet, 1998), Batimastat also reduced the contribution of vascular remodeling to the lumen shrinkage in the balloon dilated segment (Figure 1C). However, at the same time the vessel wall growth was more pronounced counteracting the beneficial effect of Batimastat. This may explain why the loss index only tended to be reduced after administration of Batimastat.

The extra wall area at follow up after administration of an MMP-inhibitor, as derived from the relationship between wall area and lumen area at follow up (Figure 2B), seems an unexpected finding as MMP-inhibition prevents the degradation of the matrix components and thereby the SMC migration (Bendeck *et al.*, 1996). However, Bendeck showed in rats with histology, that after administration of an MMP-inhibitor the neointimal thickness was not decreased (Bendeck *et al.*, 1996). This observation was explained by an increase in proliferation of SMC's in the intima during the second week after balloon angioplasty. Similarly, Zempo found cellular proliferation to increase during the second week follow up period in the rat carotid artery (Zempo *et al.*, 1996). Thus as none of these studies revealed that neointimal growth was ceased, the differences in observations between these experiments in rats and the present study might be explained by the difference in the duration of follow up period. Considering that the observed wall growth was beyond the estimated resolution of the intravascular ultrasound technique (200 μm) and the lumen and media contours were obtained by experienced IVUS analysts using a well-validated, semi-automatic software package (Li, 1997), for which the reproducibility and accuracy are high (von Birgelen *et al.*, 1997), we do not expect that the different results can be due to different measurement techniques.

8.5.2 Shear stress and wall stress control mechanisms

Under physiological conditions and in experimental atherosclerosis the diameter of the arteries are regulated by the local shear stress, so that for changes in shear stress the artery adapts its lumen diameter to keep the shear stress constant (Kamiya and Togawa, 1980; Langille, 1993). In the control group it was shown that shear stress was almost regulated to the reference segments after balloon angioplasty (Chapter 7). In the present study the modulating effect of Batimastat on the shear stress regulation was studied in the balloon segment as well. Similar to the Control group, systemic changes are expressed in the reference segement, while the balloon dilated segment is affected by a combination of local and systemic factors. Interestingly, after Batimastat administration, the reference segment in the follow up period showed less lumen decrement than the control group. In accordance with this findings the shear stress increase in the reference segment during follow up was less pronounced. This points to a beneficial effect of Batimastat in reducing constrictive vessel remodeling. For the Control group the shear stress, returned closely to reference values.

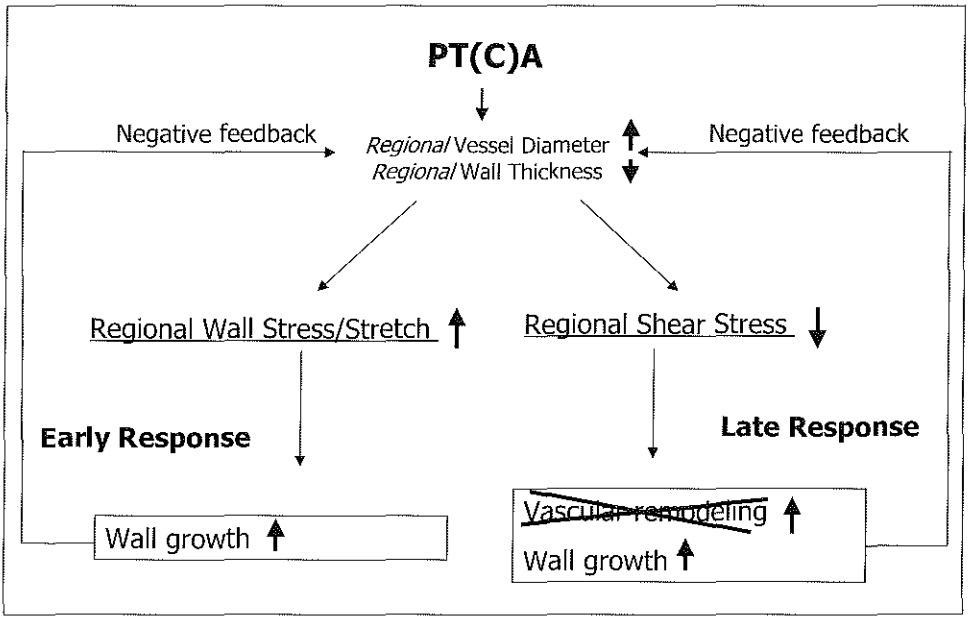

Figure 5: proposed mechanism of the the influence of Batimastat on the changes in geometry and control mechanisms during the follow up period after PTA

In contrast, for the Batimastat group, the shear stress at follow up was low with respect to reference values. As normalized shear stress is presumably not affected by systemic factors, Batimastat additionally inhibits the shear stress control system with in the balloon dilated segment. So, Batimastat seems to influence the control system itself. Figure 5 shows the proposed mechanisms of the involvement of shear stress and wall stress regulation in vascular remodeling and wall growth and the influence of Batimastat on these processes. Immediately after PTA , the endothelial layer is disrupted and shear stress is of minor importance. So the increased wall stress could initiate the wall growth (Figure 5; early response), thereby reducing the wall stress to its baseline value. Note that a doubling of the wall thickness from 0.3 to 0.6 mm could compensate the increased wall stress induced by a doubling of the vessel diameter from 3 mm to 6 mm. This implies that for normalized wall stress the lumen diameter is still high and so the shear stress is still low. When after a few weeks the endothelial layer is regenerated, the shear stress control mechanism is activated due to the low shear stress conditions (Doornekamp *et al.*, 1996). We implicitly assume that particularly the endothelial cells are responsible for the processes necessary to regulate the shear stress (Langille, 1993). Theoretically, this mechanism tries to restore the shear stress by either vascular remodeling or wall growth. Both

processes lead to reduction in wall stress. For the control group this reduction may be compensated by reduction in vessel wall thickness.
However, for the Batimastat group the vascular remodeling is hampered, thereby influencing the late response. Now, the shear stress can only be restored by increasing wall thickness. Consequently, shear stress tended to be a less sensitive predictor for vascular remodeling (Figure 4A) and the wall stress became low. The hampered vascular remodeling is expressed by the positive relation between wall stress and wall growth (Table 3). According to this theory it is beneficial to not only to inhibit vascular remodeling by Batimastat but also vessel wall growth.

8.5.3 Limitations

Since the control study showed that the acute lumen gain was an important factor in both the shear stress and wall stress normalization, the shear stress and wall stress in this study were similarly related to acute lumen gain. In the current study, however, the distribution of data over the acute lumen gain was less homogeneous than in the control group. Therefore the data in the group with intermediate acute gain (4-8 mm^2) should be interpreted cautiously. In that group only 7 data points were included.

To minimize the potential influence of arterial spasm after balloon angioplasty on our results, only the vessel segments showing a positive acute gain were included in the data set. As a consequence only a few data points were available for two vessels in the Batimastat group.

We applied a steady state, Newtonian fluid model in the present numerical analysis, while it is known that blood exerts non-Newtonian properties at low shear rate values and flow is pulsatile. In addition, the walls of the blood vessels are elastic. Several authors have shown that the combined effect of all these factors on average shear stress is relatively small in the shear rate range applied in the present study (Perktold *et al.*, 1994; Reuderink, 1991).

The 3-D reconstruction technique does not allow studying side branches. We, therefore, excluded these regions in the present analysis. As these side branches might affect local velocity field immediately up and down stream of these regions, the estimate of shear stress in those regions might be less accurate.

We applied a regional 2-D thick walled cylindrical geometry to calculate wall stress in our blood vessels. As the external iliac arteries exhibited only small curvature, the 2-D assumption seems justified. However, tissue anisotropy and local spots of very high wall stress are not accounted for in the present study. This may lead to an underestimation of the role of average wall stress in vascular remodeling.

In conclusion administration of Batimastat after balloon angioplasty reduced the vascular remodeling, thereby hampering both the shear stress and wall stress control system.

Bagshaw, R. J., Cox, R. H., Karreman, G. and Newswanger, J. (1986) Baroreceptor control of pressure-flow relationships during hypoxemia. *J. Appl. Physiol.* **60**, 166-175.

Bassiouny, H. S., Song, R. H., Hong, X. F., Singh, A., Kocharyan, H. and Glagov, S. (1998) Flow regulation of 72-kD collagenase IV (MMP-2) after experimental arterial injury. *Circulation* **98**, 157-63.

Bendeck, M. P., Irvin, C. and Reidy, M. A. (1996) Inhibition of matrix metalloproteinase activity inhibits smooth muscle cell migration but not neointimal thickening after arterial injury. *Circ Res* **78**, 38-43.

Bevan, J. A., Bevan, R. D., Chang, P. C., Pegram, B. L., Purdy, R. E. and Su, C. (1975) Analysis of changes in reactivity of rabbit arteries and veins two weeks after induction of hypertension by coarctation of the abdominal aorta. *Circ Res* **37**, 183-90.

de Smet, B. J., Kuntz, R. E., van der Helm, Y. J., Pasterkamp, G., Borst, C. and Post, M. J. (1997) Relationship between plaque mass and neointimal hyperplasia after stent placement in Yucatan micropigs. *Radiology* **203**, 484-8.

de Smet, B. J. G. L. (1998) A new Paradigm in Restenosis: Morphometric and Molecular Characteristics. *dissertation*.

Doornekamp, F. N., Borst, C. and Post, M. J. (1996) Endothelial cell recoverage and intimal hyperplasia after endothelium removal with or without smooth muscle cell necrosis in the rabbit carotid artery. *J Vasc Res* **33**, 146-55.

Glantz, S. and Slinker, B. (1990) Primer of applied regression and analysis of variance. . McGraw-Hill, Inc, Health Professions Division.

Kamiya, A. and Togawa, T. (1980) Adaptive regulation of wall shear stress to flow change in the canine carotid artery. *Am J Physiol* **239**, H14-21.

Langille, B. L. (1993) Remodeling of developing and mature arteries: endothelium, smooth muscle, and matrix. [Review]. *J Cardiovasc Pharmacol* **21**, S11-7.

Li, W. (1997) Image and signal processing in intravascular ultrasound. *dissertation* Erasmus University Rotterdam.

Nobuyoshi, M., Kimura, T., Ohishi, H., Horiuchi, H., Nosaka, H., Hamasaki, N., Yokoi, H. and Kim, K. (1991) Restenosis after percutaneous transluminal coronary angioplasty: pathologic observations in 20 patients [see comments]. *J Am Coll Cardiol* **17**, 433-9.

Perktold, K., Thurner, E. and Kenner, T. (1994) Flow and stress characteristics in rigid walled and compliant carotid artery bifurcation models. *Med Biol Eng Comput* **32**, 19-26.

Post, M. J., Borst, C. and Kuntz, R. E. (1994) The relative importance of arterial remodeling compared with intimal hyperplasia in lumen renarrowing after balloon angioplasty. A study in the normal rabbit and the hypercholesterolemic Yucatan micropig [see comments]. *Circulation* **89**, 2816-21.

Post, M. J., de Smet, B. J. G. L., van der Helm, Y., Borst, C. and Kuntz, R. E. (1997) Arterial remodeling after balloon angioplasty or stenting in an atherosclerotic experimental model. *Circulation* **96**, 996-1003.

Rachev, A., Stergiopulos, N. and Meister, J. J. (1998) A model for geometric and mechanical adaptation of arteries to sustained hypertension. *J Biomech Eng* **120**, 9-17.

Reuderink, P. (1991) Analysis of the flow in a 3D distensible model of the carotid artery bifurcation. *Thesis Eindhoven* wibro dissertatiedrukkerij, Helmond, ISBN 90-9004413-2

Rohde, L. E., Aikawa, M., Cheng, G. C., Sukhova, G., Solomon, S. D., Libby, P., Pfeffer, J., Pfeffer, M. A. and Lee, R. T. (1999) Echocardiography-derived left ventricular end-systolic regional wall stress and matrix remodeling after experimental myocardial infarction. *J Am Coll Cardiol* **33**, 835-42.

von Birgelen, C., de Vrey, E. A., Mintz, G. S., Nicosia, A., Bruining, N., Li, W., Slager, C. J., Roelandt, J. R., Serruys, P. W. and de Feyter, P. J. (1997) ECG-gated three-dimensional intravascular ultrasound: feasibility and reproducibility of the automated analysis of coronary lumen and atherosclerotic plaque dimensions in humans. *Circulation* **96**, 2944-52.

Wolinsky, H. (1970) Response of the rat aortic media to hypertension. Morphological and chemical studies. *Circ Res* **26**, 507-22.

Zempo, N., Koyama, N., Kenagy, R. D., Lea, H. J. and Clowes, A. W. (1996) Regulation of vascular smooth muscle cell migration and proliferation in vitro and in injured rat arteries by a synthetic matrix metalloproteinase inhibitor. *Arterioscler Thromb Vasc Biol* **16**, 28-33.

Summary and conclusion

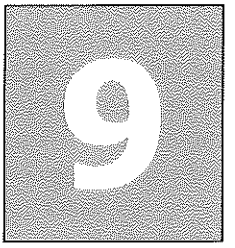

Chapter 9, summary and conclusion

The development of atherosclerotic plaques and thickening of the vessel wall after mechanical intervention occur at specific locations in the arterial system. These observations suggest that, beside the well-known systemic risk factors, like smoking, hypertension, diabetis, hypercholestermia, other more local factors must be involved in the development of atherosclerosis and restenosis. Previous studies showed that low shear stress or high wall stress regions were localizing factors in atherosclerosis and restenosis.

As under normal physiological conditions shear stress and wall stress are regulated, it was hypothesized that changes in shear stress and wall stress induced by balloon angioplasty or stent implantation are local predictors for vascular remodeling and/or neointimal growth.

In order to study the relationship between shear stress and the locations and the thickness of atherosclerotic or restenotic lesions *in vivo*, all those parameters had to be acquired in vivo. However, measurement of shear stress of blood at the vessel wall by intravascular devices is limited. In Chapter 2 the application of a new ultrasound based catheter is described which enables the local measurement of blood velocity profiles. Although this instrument is well suited to measure blood flow, its insertion in an artery implies disturbance of the velocity profile as demonstrated by computational fluid dynamics. Therefore, its application for measuring shear stress is questionable. Based on arguments presented in Chapter 1 and 2, we developed a combination of techniques involving 3-D reconstruction of the arteries and computational fluid dynamics, to obtain shear stress at the vessel wall.

3-D reconstruction of (coronary) arteries was based on a combination of angiography and intravascular ultrasound (IVUS). Intravascular ultrasound is a technique that provides cross sectional images in vivo of the vessel wall and lumen. Straight stacking of those images enables to 3-D reconstruct parts of an artery, when the IVUS catheter traveles along a straight line. Coronary arteries, however, are curved and since intravascular ultrasound in itself is a tomographic technique it does not provide any information about the spatial trajectory of the IVUS transducer. Therefore, the curved trajectory of the transducer was 3-D reconstructed, thereby using biplane X-ray images of the IVUS catheter. Combining the IVUS cross sections with the 3-D trajectory provided us with a 3-D reconstruction of the coronary arteries ('ANGUS'). This 3-D reconstruction technique was successfully introduced into the catheterization laboratory and after clinical validation applied to study (human) coronary arteries *in vivo (Chapter 3)*.

Firstly, this 3-D reconstruction technique was applied to an atherosclerotic human coronary artery. Applying computational fluid dynamics to the 3-D reconstruction of this artery provided us with the local shear stress distribution at

the vessel wall. This study confirmed earlier observations, mainly derived from post mortem studies, that the amount of atherosclerotic plaque is inversely related to shear stress, implying that at low shear stress regions, often observed in the inner curve of a coronary artery, atherosclerotic plaque is most prominent *(Chapter 4).*

Subsequently, the influence of a Wallstent on the local shear stress distribution was investigated. For that purpose Wallstents were implanted in curved parts of the coronary arteries of pigs. This study showed that due to stent implantation the local curvature of the artery was increased near the stent edges thereby generating local low and high shear stress regions deviating from the normal shear stress distribution before stenting *(Chapter 5).*

A next step was to study the influence of shear stress on neointimal growth after Wallstent implantation in *human* coronary arteries. Therefore, 3-D reconstructions of stented coronary arteries were successfully obtained in 14 patients investigated in the catheterization laboratory. By applying computational fluid dynamics to these 3-D reconstructed arteries, the shear stress distribution was obtained. Due to the IVUS technique wall thickness observation was present, which was related to the local shear stess. The neointimal thickness was inversely related to the shear stress, implying that at the low shear stress regions the maximal neointimal growth was observed. These observations make the role of shear stress in the neointimal growth after stent implantation likely. Interestingly, for a subgroup of patients entering the study with hypercholesteremia, the relationship between neointimal growth and shear stress was totally abolished *(Chapter 6).*

Subsequently, the influence of shear stress and wall stress control mechanisms on vascular remodeling and vessel wall growth after balloon angioplasty was evaluated. Therefore, the above described straight IVUS 3-D reconstruction technique was applied to the iliac arteries of 6 atherosclerotic Yucatan pigs. Due to balloon angioplasty an increase in lumen area was obtained, thereby reducing the local shear stress and increasing the local wall stress. Indeed, our results showed that both shear stress and wall stress regulated vessel shrinkage ('vascular remodeling'), such that after a period of 6 weeks both the shear stress and wall stress became equal to the reference segment *(Chapter 7).*

Previously, it has been shown that inhibition of matrix metalloproteinases strongly reduces matrix degradation and therefore limits the vascular remodeling. We investigated in the external iliac arteries of 6 atherosclerotic Yucatan pigs the effect of the matrix metalloproteinase inhibitor Batimastat on the wall stress and shear stress control mechanisms. This study showed that both the wall stress and shear stress were not normalized at follow up compared to the reference values indicating a hampering effect of Batimastat on both control mechanisms *(Chapter 8).*

Chapter 9, summary and conclusion

The conclusions drawn from the presented studies may be summarized as follows:

1. A high resolution 3-D arterial reconstruction technique combined with computational fluid dynamics provides a feasible method to study in, among others, coronary arteries of patients wall thickness and/or neointimal growth in relation to the local shear stress.

2. Shear stress plays a role in neointimal formation after stent implantation. Furthermore, both shear stress and wall stress are factors regulating the vascular remodeling after balloon angioplasty. The MMP-inhibitor Batimastat influences both the shear stress and wall stress regulation.

Verdikkingen van de vaatwand, die ontstaan door atherosclerose of optreden na behandeling van een vernauwing (bijvoorbeeld door Dotter behandeling en/of stent plaatsing) worden waargenomen op specifieke plaatsen. Deze observatie suggereert, dat naast de bekende risico-factoren, zoals roken, diabetes, hoge bloeddruk, hypercholesteremie, die in het gehele lichaam aanwezig zijn, andere meer lokale factoren bij (her)vernauwing na behandeling en atherosclerose betrokken zouden moeten zijn. Eerdere studies toonden aan dat biofysische factoren zoals afschuifspanning uitgeoefend door de bloedstroom op de vaatwand en spanning in de vaatwand betrokken zouden kunnen zijn bij het ontstaan van atherosclerose en hervernauwing na behandeling (restenose). Afschuifspanning aan de vaatwand is de voor oppervlak genormaliseerde wrijfkracht, die het stromende bloed op de vaatwand uitoefent en deze kan heel lokaal variëren in het vaatbed. Wandspanning daarentegen is de spanning in de vaatwand, die veroorzaakt wordt door de bloeddruk.

Omdat onder normale fysiologische condities afschuifspanning en wandspanning worden gereguleerd, dat wil zeggen op een ingestelde waarde worden gehouden, werd de hypothese opgesteld dat veranderingen in afschuifspanning en wandspanning zoals die worden opgewekt door bijvoorbeeld een Dotter behandeling, lokale voorspellers zijn van de lokale (her)vernauwingen. Deze vernauwingen kunnen ontstaan doordat het gehele bloedvat krimpt ('negatieve vasculaire remodellering') en/of doordat er lokale weefselgroei optreedt ('neointima groei').

Om de relatie tussen de afschuifspanning en de lokatie en de dikte van atherosclerotische wandverdikking of hervernauwing *in vivo* te bestuderen, moeten deze beide *in vivo* gemeten worden. Echter, de mogelijkheden tot meting van de afschuifspanning van het bloed aan de vaatwand zijn beperkt. Dit geldt zowel voor technieken die van buiten af werken als voor een cathetertechniek, die in het bloedvat aangebracht moet worden. In hoofdstuk 2 wordt de toepassing van een nieuwe, op ultrageluid gebaseerde, catheter beschreven, waarmee het mogelijk is om lokaal stromingsprofielen van bloed te meten. Hoewel dit instrument goed in staat is om het debiet van de bloedstroom te meten en de vaatwand te visualiseren, worden door het inbrengen van de catheter in een bloedvat de stromings profielen verstoord. De verstoring van de stromingsprofielen die door het inbrengen van een catheter optreedt, werd met behulp van numerieke stromingsberekeningen onderzocht. Uit deze stromings berekeningen moest geconcludeerd worden dat het toepassen van dit instrument voor het meten van afschuifspanning tot op heden niet mogelijk is. Omdat deze techniek (hoofdstuk 2) en andere in hoofdstuk 1 beschreven technieken niet toereikend waren, hebben we een combinatie van technieken ontwikkeld, waarbij

Samenvatting

3-D reconstructie van de bloedvaten (arteriën) wordt gecombineerd met numerieke stromings berekeningen.

De 3-D reconstructie van (coronair) arteriën werd gebaseerd op een combinatie van angiografie en intravasculair ultrageluid. Intravasculair ultrageluid is een kijktechniek, die *in vivo* beelden levert van de doorsneden van de wand en het lumen van een bloedvat. Als de geluidscatheter, tijdens een terugtrekprocedure door het bloedvat, zich langs een rechte lijn heeft voort bewogen, is het mogelijk om een 3-D reconstructie van de vaten te maken door de doorsnede beelden recht op elkaar te stapelen. Echter, coronair arteriën zijn gekromd en daarom moet het gekromde traject, dat de catheter aflegt, in 3-D worden gereconstrueerd. Dit kan door gebruik te maken van biplane röntgen-foto's van de ultrageluidscatheter. Door de doorsnedeplaatjes te combineren met het 3-D gekromde traject kan een 3-D reconstructie van een coronair arterie verkregen worden. Deze 3-D reconstructietechniek werd succesvol geïntroduceerd in het catherisatielaboratorium en na klinische evaluatie toegepast om (menselijke) coronair arteriën in vivo te bestuderen *(Hoofdstuk 3)*.

Als eerste werd deze techniek toegepast op een atherosclerotische coronair arterie van een patiënt. Numerieke stromingsberekeningen uitgevoerd in de 3-D reconstructie van deze arterie leverden ons de lokale verdeling van de afschuifspanning aan de vaatwand. Deze studie bevestigde eerdere observaties, die hoofdzakelijk verkregen werden uit post mortem materiaal, dat de hoeveelheid atherosclerotische plaque omgekeerd evenredig is met de lokale afschuifspanning van het bloed aan de vaatwand. Dit betekent dat atherosclerotische plaques voornamelijk in gebieden met lage afschuifspanning worden waargenomen, bijvoorbeeld in de binnenbocht van een coronair arterie *(Hoofdstuk 4)*.

Vervolgens werden de veranderingen in afschuifspanning na Wallstent implantatie onderzocht. Om die reden werden Wallstents geïmplanteerd in die delen van de coronair arteriën van biggen, die gekromd zijn. Deze studie toonde aan dat door het implanteren van stents de lokale kromming bij de uiteinden van de stent was toegenomen. Hierdoor werden lokale pieken en dalen in de afschuifspanning veroorzaakt, die niet aanwezig waren voor stent plaatsing *(Hoofdstuk 5)*.

Een volgende stap was om de invloed van afschuifspanning op de weefsel groei (neointima groei) na Wallstent implantatie in menselijke coronair arteriën te onderzoeken. Daarom werden 3-D reconstructies gemaakt van de gestente coronair arteriën van 14 patiënten, die in het catheterisatielaboratorium onderzocht werden. Door numerieke stromingsberekeningen toe te passen op deze 3-D gereconstrueerde vaten werd de distributie van de afschuifspanning verkregen, welke gerelateerd werd aan de neointima groei. De neointima groei was omgekeerd evenredig met de afschuifspanning, wat betekent dat in gebieden met lage afschuifspanning de meeste neointima groei werd waargenomen. Deze

waarnemingen maken de rol van afschuifspanning bij neointima groei aannemelijk. Interessant genoeg werd voor een subgroep patiënten, die bij aanvang van de studie hypercholesteremisch waren, geen relatie tussen neointima groei en afschuifspanning waargenomen *(Hoofdstuk 6)*.

Vervolgens werd de invloed van het regelmechanisme met betrekking tot afschuifspanning en wandspanning op vaatwandkrimp ('vasculaire remodellering') en vaatwandgroei na een Dotter behandeling bestudeerd. Daartoe werd de hiervoor beschreven 3-D reconstructietechniek voor rechte vaten toegepast op de iliaca arteriën van 6 atherosclerotische Yucatan biggen. Door de Dotter behandeling werd een toename van het lumen oppervlak verkregen, dat zorgde voor een afname in de lokale afschuifspanning en toename in de lokale wandspanning. Onze resultaten toonden aan dat zowel de afschuifspanning als de wandspanning de vaatwandkrimp reguleert, zodanig dat na een periode van 6 weken zowel de afschuifspanning als de wandspanning gelijk werden aan die van het niet behandelde referentie segment *(Hoofdstuk 7)*.

Eerdere studies toonden aan dat remming van de enzymen ('matrix metalloproteinases') die betrokken zijn bij het afbreken van de vaatwand, de vaatwandkrimp na een Dotter behandeling limiteert. Wij onderzochten het effect van zo'n matrix metalloproteinase remmer (Batimastat) op de regelcapaciteit van de afschuifspanning en de wandspanning in de iliaca externa van 6 atherosclerotische Yucatan biggen. Deze studie toonde aan dat zowel de afschuifspanning als de wandspanning niet worden genormaliseerd in vergelijking met de referentie segmenten, wat erop wijst dat beide regelmechanismen worden geremd door Batimastat *(Hoofdstuk 8)*.

De conclusies die uit deze studies getrokken mogen worden, kunnen als volgt worden samengevat:

1. Een 3-D bloedvat reconstructietechniek met een hoog oplossend vermogen, gecombineerd met numerieke stromingsberekeningen, levert een methode op om onder andere in coronaire bloedvaten van patiënten, wanddikte en/of neointima groei in relatie tot de lokale afschuifspanning te bestuderen.

2. Afschuifspanning van het bloed aan de vaatwand speelt een rol bij neointima formatie na stentimplantatie. Verder zijn zowel de afschuifspanning als de wandspanning factoren die de vaatwand remodellering na ballonangioplastiek regelen. De matrix metalloproteinase remmer Batimastat beïnvloedt zowel de regeling van de afschuifspanning als van de wandspanning.

Samenvatting

Harry Achterberg, Mariano Albertal, Ivan Andhyiswara, Rogier van Arkel, Heleen van Beusekom, Klaas Bom, Cees Borst, Rob van Bremen, Tom Bruinink, Stephane Carlier, Ignacio Céspedes, Elza van Deel, Robert van Dijk, Marvin Doyley, Eric Duckers, Dirk Jan Duncker, Corrie Eefting, Dahlia El Kheir, Pim de Feyter, Peter Frinking, Wim van der Giessen, Diana en Johan Groot Nibbelink, Elma van Gussenhoven, David Haitsma, Jan Honkoop, Marcel de Jong, Jan Willem de Jong, Robert de Jonge, Erik de Jonge, Liz Keijzer, Dominique de Kleijn, Jeroen Kloet, Marco Knook, Chris de Korte, Stefan Krabbendam, Rob Krams, Frido Kuijper, Charles Lancée, Glen van Langenhove, Bart Lengkeek, Li Wenguang, Frits Mastik, Jan van Meegen, Gerdiene en Klaas Jan Mulderij, Carla Nederhof, Tessa Onderwater, Jan Oomen, Gerard Pasterkamp, Mark Post, Hans Schuurbiers, Patrick Serruys, Marion Sierevogel, Kees Slager, Bart de Smet, Hans van 't Spijker, Ton van der Steen, Rene Stubenitsky, Andrew Tjon, Serge Trines, Carolina en Remko Ullersma, Piet Verdouw, Petra en Peter Verhoef, Wim Vermeulen, Ruud Vinke, Alex Wardeh, Pa en Ma Wentzel, Deirdre Whelan, Mark Winkelman, Sandra de Zeeuw

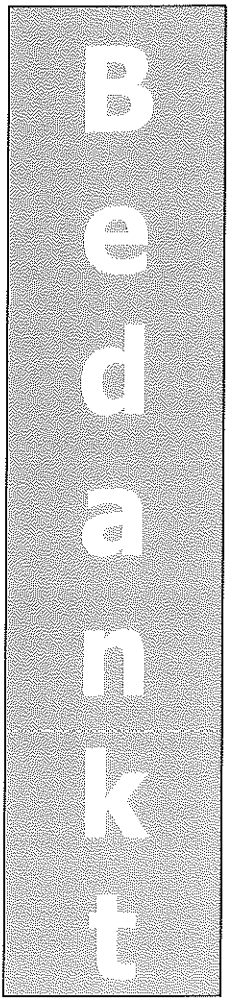

Dankwoord

Aan het tot stand komen van dit proefschrift hebben vele mensen meegewerkt. Zonder de steun en hulp van deze mensen was het onmogelijk geweest dit resultaat te bereiken.

Bedankt Prof. Dr. Ir. N. Bom, dat U mij de infrastructuur bood om het werk dat nodig was voor dit proefschrift op de afdeling Hemodynamiek te verrichten.

Bedankt Dr. R. Krams en Dr. Ir. C. J. Slager voor het vele werk dat jullie verricht hebben en de ontelbare keren dat we mijn onderzoek konden bediscussiëren. Rob je bevlogenheid en enthousiasme voor het onderzoek stimuleerde me elke keer weer om verschillende aspecten van het onderzoek aan te pakken. Daarnaast kon ik veel leren van je wetenschappelijke benadering van een probleem. Kees, je technische kennis en je oog voor detail bood menig aanknopingspunt voor het opzetten van technieken en het opzetten van theorieën.
Bedankt Jan Oomen, Hans Schuurbiers en Serge Trines voor de hulp bij de projecten en de prettige werksfeer en Jan voor de mooie (theater) verhalen tijdens de lunch.

Bedankt Experimentele Cardiologie. Prof. Dr. P. D. Verdouw hartelijk dank voor de mogelijkheid die U mij bood om experimenten uit te voeren op het dieren lab.
Bedankt Dr. H. M. M. van Beusekom, Dr. D. M. Whelan, Dr. W. J. van der Giessen en S. Krabbendam. Heleen, Deirdre, Wim en Stefan jullie gaven me de kans om metingen te verrichten aan gestente coronair vaten van biggen.
Daarnaast, heb ik veel geleerd van de verschillende discussies over het vakgebied, waaraan Dirk Jan Duncker, Eric Duckers, Sandra de Zeeuw, David Haitsma, Dahlia El Kheir, Jan Willem de Jong, Robert de Jonge, Jan van Meegen, Rob van Bremen, Elza van Deel, Rene Stubenitsky Liz Keijzer en Marcel de Jong een grote bijdrage leverden. Daarnaast wil ik Carla Nederhof bedanken voor de secretariële ondersteuning.

Bedankt Experimentele Echografie. Dr. ir. A.F.W. van der Steen, Dr. ir C. Lancée, Dr. W. Li and Dr. E. I. Céspedes wil ik met name bedanken voor de hulp bij het het schrijven van het manuscript over de stromingsverstoringen veroorzaakt door de aanwezigheid van een catheter. Ook Stephane Carlier, Peter Frinking, Chris de Korte, Marvin Doyley, Frits Mastik, Jan Honkoop en Elma van Gussenhoven wil ik bedanken voor de prettige samenwerking en de gezellige 'dinertjes' in het restaurant. Daarnaast wil ik Corrie Eefting bedanken voor de secretariële ondersteuning.

Dankwoord

Bedankt Rogier van Arkel, Andrew Tjon, Ivan Andhyiswara, Harry Achterberg, Jeroen Kloet, Bart Lengkeek, Erik de Jonge, Tom Bruinink, Robert van Dijk, Tessa Onderwater en Wim Vermeulen voor de gezelligheid en de hulp bij de verschillende projecten.

Bedankt cardiologen, cath-lab technici en verpleegkundigen van het Cath-lab. Prof Dr. P.W. Serruys, ik wil U met name hartelijk danken dat U ons in de gelegenheid stelde om metingen te verrichten tijdens de behandeling van vele patienten. Ook Dr. W. J. van der Giessen, Dr. P. J. de Feyter, G. Van Langenhove, M. Albertal, A. J. Wardeh, M. Knook, wil ik daarbij niet onvermeld laten. De cathlab-technici wil ik met name bedanken dat de apparatuur op het juiste moment in het Cath-Lab aanwezig was. Ook de verpleging was tijdens de procedures onmisbaar.

Bedankt 'Utrecht', dat we mee konden meten in de atherosclerotische Yucatan biggen. Bart de Smet, Gerard Pasterkamp, Dominique de Kleijn, Cees Borst, Marion Sierevogel, het was altijd een genoegen om met jullie over onze data te discussiëren.

Bedankt Ruud Vinke, dat je altijd klaar stond voor onze 'Unix' probleempjes.

Bedankt vrienden, dat jullie me ondersteunden en hielpen bij allerlei klusjes. Mark Winkelman bedankt voor je morele steun, waarbij de grote afstand geen rol bleek te spelen. Frido Kuijper bedankt voor het ontwerpen van de voorkant van het proefschrift. Ook Johan en Diana Groot Nibbelink, Hans van 't Spijker en Gerdiene en Klaas Jan Mulderij mogen niet vergeten worden, die hun bijdrage hebben geleverd aan de lay-out van het proefschrift.

Bedankt zussen en zwagers- Carolina & Remko en Petra & Peter- jullie toonden altijd belangstelling voor me, ook als ik soms wat druk was. Carolina bedankt voor de huishoudelijke klusjes, die je voor me gedaan hebt.

Bedankt Pa & Ma. Niet in de laatste plaats wil ik jullie hartelijk bedanken voor alles wat jullie voor me gedaan hebben. Jullie stonden altijd achter me, hielpen me waar dat kon en bij jullie kon ik altijd m'n verhaal kwijt.

Dankwoord

Curriculum Vitae

Jolanda Johanna Wentzel was born on May 2nd 1972 in Delft. She grew up in Dordrecht, were she attended 'Het Christelijk Lyceum' for 6 years. After graduation in 1990, she continued her studies at the Agriculture University Wageningen, where she studied Agriculture System Sciences (Agrosysteemkunde). This study contained classes in the field of, among others, Mathematics, Informatics and Control sciences. In order to focus her studies on the medical field she followed a course on Bioregulation at the Academic Medical Center Amsterdam. Thereafter she started a research project at the Academic Medical Center Amsterdam at the lab of biophysics under the supervision of Prof. Dr. J.A.E Spaan and Dr. J. Dankelman (Technical University Delft) and Prof Dr. Ir. A. J. Udink ten Cate (Agriculture University Wageningen). During a 6 months period she modeled the dynamic behavior of the control system of the coronary circulation. To complete her studies, she went to the Johns Hopkins University Baltimore USA, where she cooperated for 6 months in a research project on the pressure flow relationship in the septum under the supervision of dr. F. Yin. In 1995 she graduated. Subsequently, she started her PhD at the laboratory of Hemodynamics at the Thoraxcenter, Erasmus University Rotterdam, the Netherlands. Her main interest is the role of biophysical factors in the development of atherosclerosis and restenosis. At the moment she remains at the department of Hemodynamics at a post-doc position studying the same topic.

Full papers

- Grasman, J. and Wentzel, J. (1994) Co-existence of a limit cycle and an equilibrium in Kaldor's business cycle model and its consequences. *J. Econ. Behav. Organ.* **24** 369-377.

- Laban, M., Oomen, J. A., Slager, C. J., Wentzel, J. J. , Krams, R., Schuurbiers, J. C. H., den Boer, A., von Birgelen, C., Serruys, P. W. and de Feijter, P.J. (1995) ANGUS: A new Approach to Three-dimensional Reconstruction of Coronary Vessels by Combined Use of Angiography and Intravascular Ultrasound, *Computers in Cardiology, IEEE,* 325

- Wentzel, J. J., Krams, R., vander Steen, T., Wenguang, L., Cespedes, I., Bom, N. and Slager, C.J. (1997) Disturbance of 3-D velocity profiles induced by IVUS-catheter. Evaluation with computational fluid dynamics. *Computers in Cardiology, IEEE* **vol 24**, 597

- Krams, R., Wentzel, J. J., Oomen, J. A. F., Schuurbiers, J. C. H., de Feyter, P. J., Serruys, P. W. and Slager, C. J. (1997), Evaluation of Endothelial Shear Stress and 3-D Geometry as Factors Determining the Development of Atherosclerosis and Remodeling in Human Coronary Arteries in Vivo; Combining 3-D Reconstruction from Angiography and IVUS (ANGUS) with Computational Fluid Dynamics, *Arterioscler Thromb Vasc Biol* **17**, 2061-2065

- Slager, C. J., Wentzel, J. J., Oomen, J. A. F, Schuurbiers, J. C. H., Krams, R., von Birgelen, C, Tjon, A., Serruys, P.W. and de Feyter, P.J. (1997) True reconstruction of vessel geometry from combined X-ray angiographic and intracoronary ultrasound data, *Semin. Intervent. Cardiol* **2**, 43-47

- Wentzel J. J., Krams, R, Slager, C. J., Schuurbiers, J. C. H., Oomen, J. A. F., Vinke, R., Kloet, J., Andhyiswara, I., Achterberg, H., de Feyter, P. J. and Serruys, P.W. (1998) The role of shear stress in atherosclerosis restenosis and vascular remodeling, *the Thoraxcentre Journal*, **volume 10/2**, 12-17

- Krams, R. Wentzel J. J., Cespedes, I., Carlier, S., van der Steen, A. F. W., Lancee, C. T. and Slager, C. J. (1999) Effect of catheter placement on 3-D velocity profiles in curved tubes resembling the human coronary system, *Ultrasound Med Biol* **Jun; 25(5)**, 803-10

List of publications

- Krams R., Wentzel J. J., Oomen J. A. F., Schuurbiers, J. C. H., Andhyiswara, I., Kloet, J., Post, M., de Smet B., Borst, C., Slager, C. J., Serruys, P. W. (1998) Shear stress in atherosclerosis and vascular remodelling, *Semin Interv Cardiol.* **Mar;3(1)**, 39-44.

- Wentzel, J. J., Whelan, D., van Beusekom, H. M. M., van der Giessen, W. J., Andhyiswara, I., Serruys, P. W., Slager, C. J. and Krams, R., Stent implantation in coronary arteries causes alterations in 3-D geometry and distribution of 3-D shear stress at the endothelium, *Journal of Biomechanics, in press*

- Van Langenhove, G., Wentzel, J. J., Krams, R., Slager, C. J., de Jonge, E., Serrano, P., Hamburger, J. N. and Serruys, P. W., Helical velocity patterns in a human coronary artery. A 3-D computational fluid dynamic reconstruction showing the relation with local wall thickness, *Circulation, in press*

- Bom, N., de Korte, C. L., Wentzel, J. J., Krams, R., Carlier, S. G., van der Steen, A. W. F., Slager, C. J., and Roelandt, J. R. T. C., (1999) Quantification of plaque volume, shear stress on the endothelium an mechanical properties of the arteria wall with intravascular imaging, *Zeitschrift für Kardiologie, in press*

- Schuurbiers, J. C. H. , von Birgelen, C., Wentzel, J. J., Bom, N., Serruys, P. W., de Feyter, P. J. and Slager, C. J., On the plaque volume error of three-dimensional IVUS when using a straight reconstruction approach, *submitted*

- Slager, C. J., Wentzel, J. J, Schuurbiers, J. C. H., Oomen, J. A. F., Kloet, J, Krams, R, von Birgelen, C., van der Giessen, W. J., Serruys. P. W. and de Feyter, P. J. True 3-D Reconstruction of Coronary Arteries in Patients by fusion of Angiography and IVUS (ANGUS) and its Quantitative Validation, *submitted*

- Wentzel J. J., Krams, R., Kloet, J., van der Giessen, W. J., Serruys, P. W. and C. J. Slager, The relationship between neointimal thickness and shear stress after Wallstent implantation in human coronary arteries at 6 months follow up, *submitted*

- Krams, R., Wentzel, J. J., Kloet, J., Andhyiswara, I., Oomen, J. A., Schuurbiers, J. C. H., de Kleijn, D., Pasterkamp, G., Borst, C. and Slager, C. J. The role of regional shear stress and regional wall stress in vascular remodeling after balloon angioplasty, *submitted*

- Wentzel, J. J., Kloet, J., Andhyiswara, I., Oomen, J. A., Schuurbiers, J. C. H., de Smet, B. J. G. L., de Kleijn, D., Pasterkamp, G., Borst, C., Slager, C. J. and Krams, R. Reduction in constrictive vascular remodeling after PTA by Batimastat is accompanied by hampered normalization of wall stress and shear stress, *submitted*

Abstracts

- Chan, C., Wentzel, J. J., Judd, R., Spaan, J. A. E. and Yin, F. C. P. (1995) Tissue thickness is a measure of coronary vascular volume in canine interventricular septa. *Faseb* **J9 (4),** A847

- Cornelissen, J. M., Chan, C., Wentzel, J., Yin, F. C. P and Spaan J.A.E. (1995) Pressure dependence of transfer functions between coronary vascular pressure, flow and volume, Faseb, **J9 (4),** A848

- Wentzel, J. J., Krams, R., Oomen, J. A. F., Schuurbiers, J. C. H., Vinke, R., Bom, N. and Slager, C.J. (1996) Applying computational fluid dynamics to a spatially correct 3-D reconstrucion of a coronary arterial segment in the individual patient, *Proc. IEEE Eng. Med. Bio.* Amsterdam nr 482.

- Wentzel, J., Krams, R., Oomen, J., Schuurbiers, J., Vinke, R., Bom, N. and Slager, C.J. (1997) Computational fluid dynamics in an IVUS derived true 3-D reconstrucion of a human coronary artery in vivo, *the Thoraxcentre Journal,* June pg. 23

- Wentzel, J. J., Krams, R., van Beusekom, H. M. M., Whelan, D., van der Giessen, W. J., Krabbendam, S., Andhyiswara, I., Tjon Joek Tjien, A., Schuurbiers, J. C. H., Oomen, J. A. F., Bom, N. and Slager, C. J. (1997) Stent implantation causes alterations in 3-D geometry and 3-D shear stress distribution at the endothelium of coronary arteries, *Circulation* **vol 96: Suppl I**, 2349

- Krams, R., Wentzel J. J., Oomen, J., Schuurbiers, J., Vinke, R. and Slager, C. J. (1997) Evidence for a Pivotal Role of Shear Stress on the Endothelium in Human Atherosclerosis, *Endothelium,* **Vol. 5**, 353-367

List of publications

- Wentzel J. J., Whelan, D., van Beusekom, H. M. M., Krams, R., van der Giessen, W. J., Andhyiswara, I., Schuurbiers, J. C. H., Oomen, J. A. F., Bom, N. and Slager, C. J. (1998) Applying computational fluid dynamics in ivus derived 3-D reconstruction of coronary arteries before and after stent implantation, *Proceedings of 3RD World Congress of Biomechanics , Sapporo, Japan*

- Krams R., Wentzel J. J., Oomen, J. A. F, Schuurbiers, H., van der Giessen, W., Whelan, D., van Beusekom, H., de Smet, B., Post, M., Andhyiswara, I. A., Achterberg, H., and Slager, C. J. (1998) The role of shear stress in vascular remodeling and in stent restenosis, *Proceedings of 3RD World Congress of Biomechanics Sapporo, Japan*

- Slager, C. J., Wentzel, J. J., Schuurbiers, J. C. H, Oomen, J. A., Krams, R., Achterberg, H., Kloet, J., de Feyter, P. J. (1998) True 3-D reconstruction of coronary arteries in patients shows accurate correspondence between X-ray and IVUS derived dimensions, *Circulation* **vol 98, Suppl I**,2673

- Wentzel, J. J., Kloet, J., Krams, R., Serruys, P. W. and Slager, C. J. (1999) The relationship between neo intimal thickness and shear stress after Wallstent implantation in human coronary arteries at 6 months follow up, *Basis Research in Cardiology,* **Vol 94**, No. 5, 114

- Wentzel, J. J., Kloet, J., Krams, R., Serruys, P. W. and Slager, C. J. (1999) The relationship between neointimal thickness and shear stress after Wallstent implantation in human coronary arteries at 6 months follow up, *Circulation,* **vol 100, Suppl I**, 3840